SIMULATION AND EXPERIMENTAL STUDY OF THE MULTICHANNELING RIMFIRE GAS SWITCH

A Thesis
Presented to
The Faculty of the Graduate School
University of Missouri-Columbia

In Partial Fulfillment
Of the Requirements for the Degree
Master of Science

By
MARK A. KEMP

Dr. Randy Curry, Thesis Advisor

May 2005

The undersigned, appointed by the Dean of the Graduate School, have examined the thesis entitled

SIMULATION AND EXPERIMENTAL STUDY OF THE MULTICHANNELING RIMFIRE GAS SWITCH

presented by Mark Kemp,

a candidate for the degree of Master of Science, and hereby certify that in their opinion it is worthy of acceptance.

Dr. Randy Curry, Thesis Advisor
Electrical and Computer Engineering

Dr. John Gahl
Electrical and Computer Engineering

Dr. Mark Prelas
Nuclear Engineering

Dr. Scott Kovaleski
Electrical and Computer Engineering

Dr. Kenneth Struve
Electrical and Computer Engineering

ACKNOWLEDGMENTS

First, I would like to thank my advisor Dr. Curry. His guidance and encouragement made this work possible. He first gave me research opportunities as an undergraduate worker over four years ago. In addition, I thank Dr. Gahl for pursuing collaboration with Sandia for this project. Technical advice was always appreciated. Additionally, I would like to thank my third committee member Dr. Prelas.

Dr. McDonald has always been a calming presence whose logical insight into problems is refreshing. Dr. Kovaleski was a great help with circuit analysis issues as well as discussions regarding plasma phenomenon. During my summer at Sandia, Dr. Elizondo and Dr. Struve were very helpful. Without their support for the University of Missouri, none of this work would be possible.

I would like to thank my fellow MUTTS researchers Keith and Andy. Both of them constantly provided suggestions and encouragement with my work. Many undergraduates also gave invaluable assistance: Shaun, Paul, Mike 1, Mike 2, Tim, Ramasami, Zach, Brandon, and Bill.

My parents always have provided me encouragement with my schoolwork and through their emphasis on learning and education, they set the foundation for my college career. Last, but not least, I thank my wife Tanya for tolerating my long nights and weekends at the lab and always being supportive of my work.

TABLE OF CONTENTS

LIST OF TABLES

LIST OF FIGURES

CHAPTER 1

BACKGROUND

At Sandia National Laboratories (Sandia), many high current, high voltage accelerators have a need for fast, efficient closing switches. Since 1985, the Rimfire switch has fulfilled this need. However, with the increased performance requirements of newer accelerators, many aspects of the switch need to be improved upon. This thesis discusses some of the research conducted at the University of Missouri-Columbia with respect to improvements and further characterization of the Rimfire switch. This chapter is a brief introduction to the function of the switch, past versions of the switch, the University of Missouri Terawatt Test Stand (MUTTS), and the goals of this research project.

1.1 Introduction to the Rimfire Switch

Although the Rimfire switch has had many different versions used in its various implementations in accelerators, the basic concept and operating

characteristics have not significantly changed. A drawing of a version of the Rimfire switch is shown in Figure 1. Label 1 corresponds to the cascade section of the switch. This section contains a number of floating toroidal electrodes separated and held in place by acrylic cylinders. Label 2 is the trigger section. It is two hemispherical electrodes that connect one endplate, label 6, to the cascade section. The floating trigger electrode, label 3, is sometimes referred to as the disk electrode. The disk electrode is also the beginning of the cascade section. Both the trigger and cascade section are contained in an acrylic housing, label 7, filled with a gas (most commonly SF_6). The entire switch is immersed in a dielectric, label 4, which, depending on the application, is either deionized water or transformer oil [1].

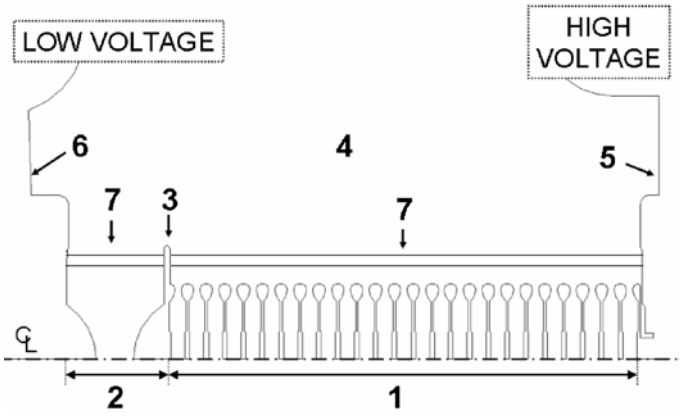

Figure 1: Drawing of the Rimfire switch.

In the most typical application, a pulsed voltage is applied across the switch, which will not conduct until either the self-break voltage is exceeded or it is successfully triggered. After that point, current will flow through the switch and the voltage across the switch will decrease. Figure 2 shows a power flow diagram

of PBFA-Z, which is a typical application of the Rimfire switch. Components C_M and L_M are, respectively, the equivalent capacitance and inductance of the Marx generator. A Marx generator is an arrangement of capacitors that are charged in parallel and then discharged in series, multiplying the charge voltage. The Marx generator is switched into an intermediate store whose voltage increases with a $1-\cos(\omega t)$ waveform. The Rimfire switch (S_2) closes and the intermediate store discharges into a second intermediate store. This intermediate store then discharges into a pulse forming network and the power flow continues into the load [2].

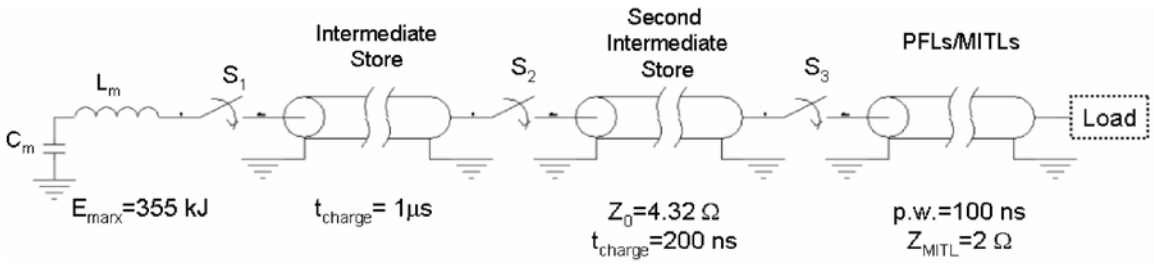

Figure 2: Simple power flow diagram for PBFA-Z [2].

There are several characteristics that describe the Rimfire switch. First is the maximum voltage hold-off. This parameter is determined primarily by the gas pressure and by the number of cascade gaps [3]. The second parameter of the switch is its jitter. Jitter is defined as the shot-to-shot variance in the timing of switch closure. A third parameter is runtime. Runtime has had several definitions in the literature, and direct comparison of values is not always possible. In-depth analysis of this issue is discussed in section 3.2.3. Runtime is in-effect how fast

the switch closes. Two different triggering methods have been used for the switch: laser triggering and electrical triggering using a trigatron.

The Rimfire switch plays an integral role in the power flow in large accelerators. If, for example, the jitter is exceptionally high in the switch, then power flow from that point forward is adversely affected. In addition, if the switch has too large of an inductance, pulse risetime will be unacceptably large. Therefore, improvement of these switch parameters is necessary for improved accelerator performance.

1.2 Past Versions of the Switch

Before the Rimfire switch, there were several types of cascade electrode gas switches used in industry [4,5]. The first version of the Rimfire switch evolved from a self-break switch developed in the Sandia Speed test stand. The cascade electrodes were not toroidal in shape, but flat plates [6]. Laser triggering was initially attempted by directly focusing a KrF or Nd:YAG laser on the first cascade gap [7]. Later, a hemispherical trigger section was implemented in series with the cascade gaps [8]. An electrically triggered version of this switch eventually replaced a hemispherical trigatron switch on the PBFA I accelerator [9]. The PBFA I accelerator was refurbished and became the Saturn accelerator and the electrically triggered switch was upgraded with the refurbishment [10].

The first application of the Rimfire switch was in the PBFA II accelerator. Much like the PBFA I version of the switch, this switch utilized toroidal cascade electrodes in series with a laser-triggered hemispherical gap [1]. Later,

improvements to this version of the switch were made and implemented in PBFA II [11]. The PBFA II accelerator was eventually upgraded to PBFA II-Z, however there was no upgrade to the existing switch [12]. After modifications were made to the PBFA II version, the Rimfire switch was installed into the Hermes III accelerator [13,14]. This switch was a lower voltage version of the switch utilized in PBFA II.

The High Current Electronics Institute (HCEI) developed a version of the Rimfire switch for use with water filled transmission lines [15]. Research on that switch coupled with tests on the Advanced Pulsed Power Research Module (APPRM) at SNL led to the development of the version of the Rimfire switch which will be installed on the upgrade to PBFA II-Z, the ZR Accelerator [16-19].

Table 1 shows a brief summary of the Rimfire switches installed in accelerators at Sandia. In all cases, the jitter is one standard deviation from the mean (1-σ) and the voltage range is the maximum pulsed voltage across the switch. There are additional switch parameters quoted in the literature, however in many cases there is a discrepancy with the exact method of measurement or derivation. The most dramatic example of this is in the case of runtime, which is discussed in detail in section 3.2.3. Another example is the calculation of switch inductance. Some sources give detailed derivations and cite specifically from where an inductance value comes [20,21]. However, specifically in reference to the PBFA II switch, discrepancies arise with the method of measurement. For example, Humphreys quotes that the inductance of the Rimfire switch in PBFA II must be about 400 nH [1]. However, when giving an overview of the PBFA II program, Martin states that the inductance must be lower than 150 nH [22]. This

illustrates the difficulty of referencing values from multiple sources. Both sources refer to the same switch; however, they may have been analyzed in a different manner.

Table 1: Maximum voltage and jitter parameters for Rimfire switches used at Sandia.

	Voltage Range (MV) *Tested* *Operation*	**Jitter (ns)**
PBFA II–version 1	2.5 - 5.7 5	4-10
PBFA II-version 2/ PBFA II-Z	2.4 – 5 5	2-3
Hermes III	1.2 - 2.8 2.2 - 2.4	2
Saturn	1.5 - 3.3 3.2	1.5
ZR Baseline	2-5.5 4.9	1.3

1.3 University of Missouri Terawatt Test Stand

To facilitate the need of Sandia for additional research on the Rimfire switch, the University of Missouri Terawatt Test Stand (MUTTS) started construction in early 2003 [23]. The first shot occurred in April 2004 and the test stand was commissioned in the summer of 2004. The objective of the test stand is to supply Sandia with quality information regarding improvements to the existing Rimfire design.

The MUTTS accelerator is a refurbishment of a Marx generator and intermediate store from the Proto II accelerator [24]. The components are contained in a 10,000 gallon tank filled with a synthetic oil, Luminol, for electrical insulation [25]. The Marx bank has thirty-two Aerovox 100 kV, 700 nF

capacitors which are switched by sixteen, 200 kV Physics International T508 spark gaps [26]. The Marx bank discharges into two parallel, 7 nF intermediate storage capacitors (intermediate stores) which the Rimfire switch then discharges into a 4.1 Ω resistive dummy load. Output parameters are shown in Table 2 and experimentally derived circuit parameters from Lechien are shown in Figure 3 [20]. The circuit elements C_m, L_m and R_m are the equivalent Marx capacitance, inductance and resistance. The resistance R_s is the shunt resistance to ground. Circuit elements L_b and R_b are the inductance and resistance of the bus connecting the Marx and the intermediate stores. The elements L_{is1} and C_{is1} are the inductance and capacitance of intermediate store 1 and L_{is2} and C_{is2} are the inductance and capacitance of intermediate store 2. The circuit parameters for the output switch and load vary from experiment to experiment. As will be shown later, geometry changes to the switch can significantly alter the electrical characteristics of the switch [20,23]. An alternate MUTTS circuit diagram is given in section 4.1 of this paper.

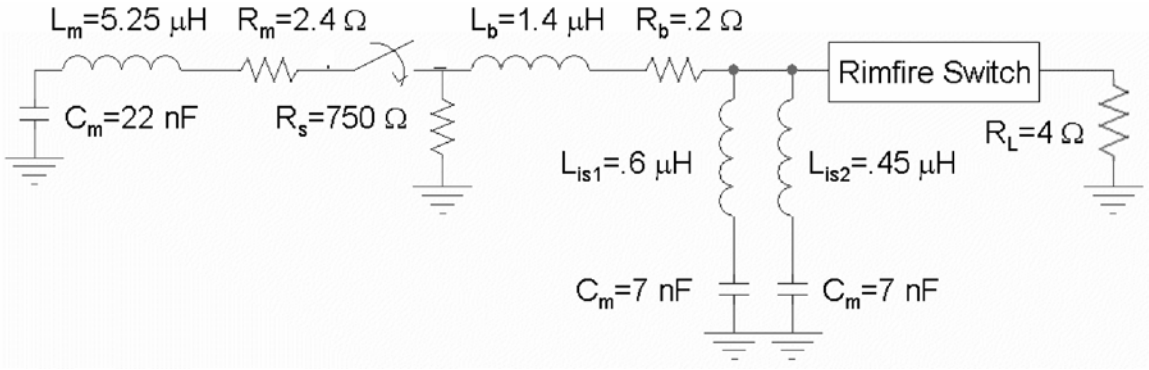

Figure 3: Simplified circuit diagram of MUTTS pulsed power system [20].

Photographs of the completed facility are shown in Figure 4. The left photograph of Figure 4 shows the resistive load, Rimfire switch, and the intermediate stores. The bus connecting the intermediate stores and the Marx generator is shown in the middle right of the picture. The right photograph in Figure 4 shows a side view of the copper sulfate resistive load and the Rimfire switch.

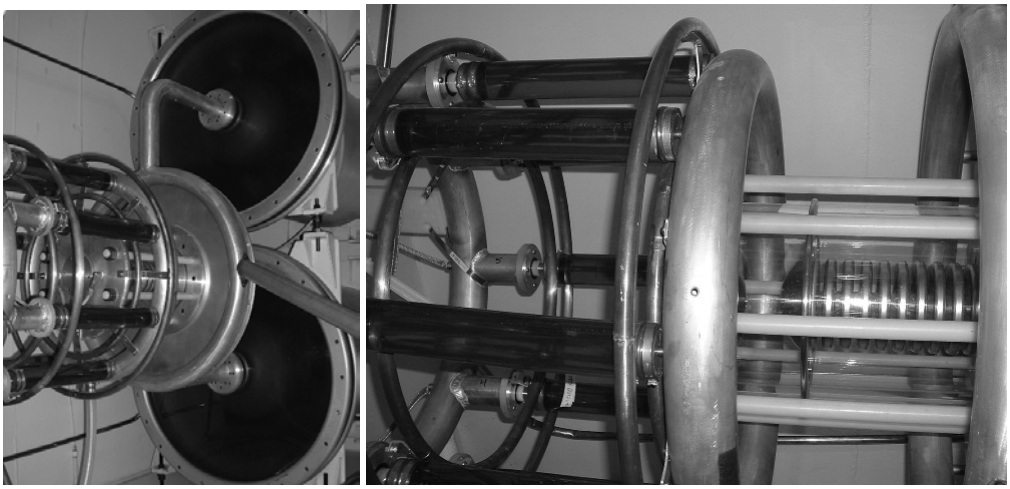

Figure 4: Photographs of some MUTTS components. Left: Intermediate stores connected to switch and load. Right: Close-up of switch and load.

The result of simulating the circuit of Figure 3 is shown in Figure 5. This result was for a Marx charge of 84.5 kV per capacitor and a load of a 450 nH inductor in series with a 4 Ω resistor. The Rimfire switch was triggered when the intermediate store reached 90% of its maximum voltage. Experimentally measured waveforms from MUTTS are presented in section 4.2.

A summary of the maximum output characteristics is shown in Table 2. These were derived from the simulation used for Figure 5. The limiting factor of

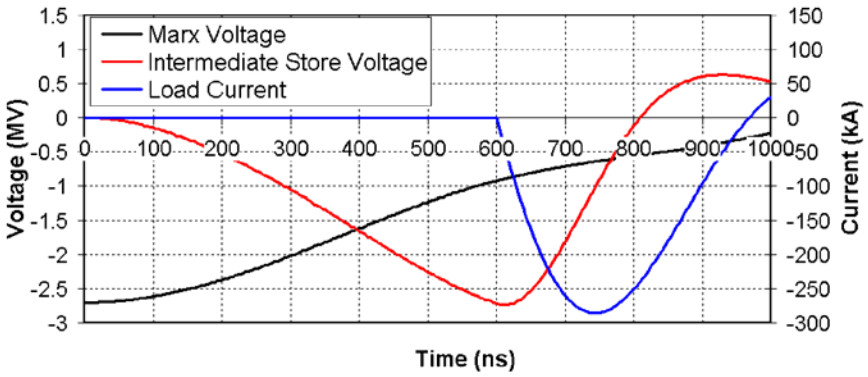

Figure 5: MUTTS simulated output waveforms- 84.5 kV Marx charge, switch triggered at 90% intermediate store max.

the output voltage at MUTTS is the intermediate stores. In past configurations, breakdown in the water occurred at approximately 2.7 MV. It was not determined if this was due to the initial negative voltage pulse, or the positive voltage reversal [27]. MUTTS has not yet been fired at full charge. Such tests are planned for the future.

Table 2: MUTTS output parameters for an 84.5 kV Marx charge and switch triggered at 90% intermediate store maximum voltage.

Peak Intermediate Store Voltage (untriggered)	3 MV
Peak Load Current	285 kA
Load Current Risetime (10%-90%)	95 ns
Load Current FWHM	228 ns
Intermediate Store Voltage Risetime (10%-90%)	400 ns
Intermediate Store Reversal	630 kV / 23 %

1.4 Research Goals and Objectives

There are several needs for the improvement of the Rimfire switch. This paper will focus on three. In the preliminary switch for the ZR accelerator, a jitter of 1.3 ns (1-σ) has been achieved [17]. Further reduction of this jitter may become

necessary in future accelerator designs. Large switch jitter can have significant negative effects on the overall performance of a large accelerator. A second need is consistent multichanneling in the cascade section of the switch. Parameters that affect the multichanneling properties need to be better understood. When Rimfire switches are designed to be very low inductance, the design will depend on reliable multichanneling. The third need is for further characterization of the Rimfire switch. Although several models of the switch exist, further modeling will increase the simulation capabilities, and allow scaling of the switch for future accelerator applications.

To address these requirements, two different approaches were selected. First, an advanced circuit model of the switch was developed. From this model, insights can be gained into runtime and the switch jitter. Second, experimental tests were performed to study the multichanneling parameters of the self-break Rimfire switch. Shots on MUTTS were compared to existing models, and this allowed us to:

- Develop and verify an advanced circuit model of the Rimfire switch.
- Compare the UMC model to past results from Rosenthal, Volkov, and experimental data [18] [15].
- Evaluate the electrical effects of specific changes to the Rimfire geometry.
- Evaluate the effects of advanced triggering methods.
- Develop a curve fitting technique to evaluate the inductance of the switch.
- Experimentally verify inductance equations for the cascade section.

- Evaluate the effect of cascade electrode azimuthal currents on the overall switch inductance.
- Experimentally evaluate various topologies for enhancement of multichanneling in the series switches that comprise the Rimfire switch.
- Develop conceptual Rimfire switch topologies for improved performance.

CHAPTER 1 REFERENCES

[1] D.R.Humphreys, K.J.Penn, J.S.Cap, R.G.Adams, J.F.Seamen, and B.N.Turman, "Rimfire: A Six Megavolt Laser-Triggered Gas-Filled Switch for PBFA II," *in Proceedings of the 5th IEEE Pulsed Power Conference*, Arlington, VA, 1985.

[2] R.B.Spielman, W.A.Stygar, J.F.Seamen, F.Long, H.Ives, and R.Lample, "Pulsed Power Performance of PBFA Z," *in Proceedings of the 11th IEEE Pulsed Power Conference*, Baltimore, MA, 1997.

[3] B.N.Turman and D.R.Humphreys, "Scaling Relations for the Rimfire Multi-Stage Gas Switch," *in Proceedings of the 6th IEEE Pulsed Power Conference, Arlington*, VA, 1987.

[4] L.Demeter, "High-Voltage Tests of the PI Trigger Gas Switch," Physics International Report, Num. PI FR-1429, 1981.

[5] J.W.Douglas, W.F.J.Crewson, and C.H.Jones Jr., "The DQ Switch - Operation at 4 Million Volts and 800 Kiloamperes," Defense Nuclear Agency Report, Num. DNA 5160F, 1979.

[6] J.F.Seamen, J.P.VanDevender, D.L.Johnson, T.H.Martin, G.Zawadzkas, E.L.Neau, W.Beezhold, M.Mikkelson, S.Downie, and D.Green, "Speed, A 2.5 TW, Low Impedance Pulsed Power Research Facility*," in Proceedings of the 4th IEEE Pulsed Power Conference*, Albuquerque, NM, 1983.

[7] R.G.Adams, W.B.Moore, J.R.Woodworth, M.M.Dillon, F.Morgan, and K.J.Penn, "Ultraviolet Laser Triggereing of a 5 Megavolt Multistage Gas Switch," *in Proceedings of the 4th IEEE Pulsed Power Conference,* Albuquerque, NM, 1983.

[8] B.N.Turman, W.B.S.Moore, J.F.Seamen, F.Morgan, J.Penn, and D.R.Humphreys, "Development Tests of a 6 MV, Multistage Gas Switch for PBFA II," *in Proceedings of the 4th IEEE Pulsed Power Conference*, Albuquerque, NM, 1983.

[9] D.D.Bloomquist, G.R.Montry, S.E.Downie, and G.R.Peterson, "Cascade Switch Implementation on PBFA I," *in Proceedings of the 5th IEEE Pulsed Power Conference*, Arlington, VA, 1985.

[10] D.D.Bloomquist, R.W.Stinnett, D.H.McDaniel, J.R.Lee, A.W.Sharpe, and and J.A.Halbleib, "Saturn, A large Area X-Ray Simulation Accelerator*," in Proceedings of the 6th IEEE Pulsed Power Conference*, Arlington, VA, 1987.

[11] J.M.Wilson and G.L.Donovan, "Laser-Triggered Gas Switch Improvements on PBFA-II," *in Proceedings of the 6th IEEE Pulsed Power Conference,* Arlington, VA, 1987.

[12] R.B.Spielman, F.Long, T.H.Martin, J.W.Poukey, D.B.Seidel, W.Shoup, W.A.Stygar, D.H.McDaniel, M.A.Mostrom, K.W.Struve, P.Corcoran, I.Smith, and P.Spence, "PBFA II-Z: A 20-MA Drivre for X-Pinch Experiments," *in Proceedings of the 10th IEEE Pulsed Power Conference*, Albuquerque, NM, 1995.

[13] B.N.Turman and D.R.Humphreys, "Scaling Relations for the Rimfore Multi-Stage Gas Switch," *in Proceedings of the 6th IEEE Pulsed Power Conference*, Arlington, VA, 1987.

[14] G.J.Denison, J.P.Corley, D.L.Johnson, G.J.Weber, R.A.Hamil, G.W.Crowder, J.A.Alexander, D.A.Petmecky, L.P.Schanwald, and J.J.Ramirez, "A High-Voltage Multistage Laser-Triggered Gas Switch," *in Proceedings of the 6th IEEE Pulsed Power Conference*, Arlington, VA, 1987.

[15] S.N.Volkov, A.A.Kim, B.M.Kovalchuk, V.V.Kremnev, and V.A.Sinebryukhov, "MV Multi Channel Closing Switch for Water Storages," *in Proceedings of the 12th IEEE International Pulsed Power Conference*, Monterey, CA, 1999.

[16] J.P.Corley, M.A.Dixon, A.A.Kim, B.M.Kovalchuk, V.A.Sinebryukhov, S.N.Volkov, K.C.Hodge, S.A.Drennan, J.M.Navarro, D.L.Johnson, G.Avrillaud, and F.Lassalle, "Tests of 6-MV Triggered Switches on APPRM at SNL," *in Proceedings of the 13th IEEE International Pulsed Power Conference*, Las Vegas, NV, 2001.

[17] J.P.Corley, K.C.Hodge, S.A.Drennan, D.W.Guthrie, J.M.Navarro, D.L.Johnson, J.M.Lehr, S.E.Rosenthal, and J.M.Elizondo, "Development/Tests of 6-MV Triggered Gas Switches at SNL," *in Proceedings of the 14th IEEE International Pulsed Power Conference*, Dallas, TX, 2003.

[18] S.E.Rosenthal, J.M.Elizondo, J.E.Maenchen, K.W.Struve, D.H.McDaniel, J.P.Corley, D.L.Johnson, and B.V.Oliver, "Modeling 6-MV Gas Switches For the ZR Accelerator," *in Proceedings of the 14th IEEE Pulsed Power Conference*, Dallas, TX, 2003.

[19] K.W.Struve, J.P.Corley, D.H.McDaniel, D.L.Smith, R.B.Spielman, W.A.Stygar, D.L.Johnson, and R.W.Shoup, "Design Options for a Pulsed-Power Upgrade of the Accelerator," *in Proceedings of the 13th IEEE Pulsed Power Conference*, Las Vegas, NV, 2001.

[20] K.R.LeChien, J.M.Gahl, M.A.Kemp, A.L.Benwell, J.M.Elizondo, and K.W.Struve, "Initial Results from the University of Missouri Terawatt Test Stand," *in Proceedings of the 26th IEEE Power Modulator Symposium,* San Francisco, CA, 2004.

[21] J.M.Elizondo, K.W.Struve, J.P.Corley, and D.L.Johnson, "Inductance Calculation for the Rim-Fire Multi-Channel Switch," ZR Technical Note, Num. 5, 2002.

[22] T.H.Martin, B.N.Turman, S.A.Goldstein, J.M.Wilson, D.L.Cook, D.H.McDaniel, E.L.Burgess, G.E.Rochau, E.L.Neau, and D.R.Humphreys, "PBFA II, The Pulsed Power Characterization Phase," *in Proceedings of the 6th IEEE Pulsed Power Conference*, Arlington, VA, 1987.

[23] K.R.LeChien, J.M.Gahl, M.A.Kemp, R.D.Curry, J.M.Elizondo, and K.W.Struve, "Development of a Terawatt Test Stand at the University of Missouri for Fast, Multichannel Switching Analysis," *in Proceedings of the 14th IEEE Pulsed Power Conference*, Dallas, TX, 2003.

[24] D.L.Johnson, "Initial Proto II Pulsed Power Tests," *in Proceedings of the 1st IEEE International Pulsed Power Conference*, Lubbock, TX, 1976.

[25] Petro-Canada, Calgary, Alberta.

[26] Aerovox Div. PPC, New Bedford, MA.

[27] Robin Sharpe, personal communication.

CHAPTER 2

RIMFIRE GAS SWITCH THEORY

Gas switches have been used effectively for closing switches in pulsed power applications for decades. Many aspects of them have been studied extensively and are well understood [1,2]. Rather than provide a synopsis of all gas switch research to date, this chapter provides a brief introduction to some gas switch theory as it applies directly to this research. This will focus on pulse-charged gas switch breakdown, multiple conductor switching, and multichanneling in the Rimfire switch.

2.1 Breakdown

Many extensive studies have been conducted characterizing gas breakdown phenomenon. Because the work in this thesis is not concerned with characterizing gas breakdown data for the Rimfire switch, a previously developed model for breakdown in large gas pulsed charged switches was utilized. Tom

Martin developed several models for gas switch breakdown while at Sandia [28,29]. Using Charlie Martin's negative streamer transit formula, equation (1), as a basis, T. Martin calculates an empirical equation for gas switch breakdown delay, equation (2) [2]. For (1), F is the gap voltage, in kV, at breakdown divided by the gap spacing, in cm. The variable t_{eff} is the time the voltage exceeds .89 of the breakdown voltage, p is the absolute pressure in atmospheres, K is a constant dependent on polarity, and n is a gas constant. The value of n for SF_6 is 0.4. For (2), ρ is the gas density in gm/cc, τ is the breakdown delay in seconds, and E is the average electric field in kV/cm. The breakdown delay consists of three intervals: a fast discharge, a thermal or transition phase, and the final resistive phase of the arc. By incorporating these times into one equation, a wide variety of switching applications are able to utilize equation (2) as a guide for breakdown delay [29].

$$F = \frac{K \cdot p^{n}}{t_{eff}^{1/6} \cdot d^{1/6}} \quad \text{[kV/cm]} \tag{1}$$

$$\tau = \frac{97800 \cdot (E/\rho)^{-3.44}}{\rho} \quad \text{[s]} \tag{2}$$

For pulse charged breakdown of gasses, the SF_6 DC breakdown data given by Nitta were utilized by T. Martin as described in his earlier paper [3,5]. Nitta published probabilities of DC charged SF_6 breakdown data for large area gaps. T. Martin combined these data with J.C. Martin's analysis of streamer propagation

[2]. T. Martin used this relationship to match breakdown data from the gas switch in PBFA–I. The PBFA-I switch operated at nearly the same voltage hold off requirements as the Rimfire switch [4].

In both the UMC circuit model described in chapter 3 and the MUTTS experiments described in chapter 4, equation (2) was used in conjunction with DC breakdown data to calculate the breakdown voltages of the switch. In the circuit model, separate parameters were used for the hemispherical electrode trigger section and the toroidal electrode cascade section. Voltage breakdown values vary from switch to switch based on the system charging parameters and switch geometry.

2.2 Multiple Conductor Switching

This section discusses the breakdown sequence in the Rimfire switch. There are three possible breakdown modes for the switch. In the first case, the trigger section is closed by the arrival of a laser pulse in the trigger gap that induces breakdown earlier than the untriggered self-break voltage. This provides precise control over the closing time of the switch. The second mode of breakdown is when the switch is untriggered and the trigger gap self-breaks. This breakdown of the trigger section will induce the cascade section to break down as well. The third mode of operation is when the cascade section self-breaks before the trigger section. This may or may not be an optimal situation. However, in practice, the latter two modes are almost never utilized because the switch is always triggered.

In mode one or two, the trigger section closes before the cascade section. Figure 6 illustrates this switch breakdown sequence. At $t=t_1$, the trigger section breaks down and the voltage across it (shown in red) decreases. The voltage across the entire switch (shown in black) remains constant, so the voltage across the cascade section (shown in blue) increases. The voltage across the cascade section increases because the voltage across the trigger section plus the voltage across the cascade section must equal the voltage across the entire switch. At $t=t_2$, the cascade section increases past its self-break voltage and breaks down. At this point, the entire switch has broken down, current starts to flow, and then the voltage across the switch begins to decrease. Figure 21 and Figure 22 in section 3.2.2 further illustrate this process using the UMC circuit model.

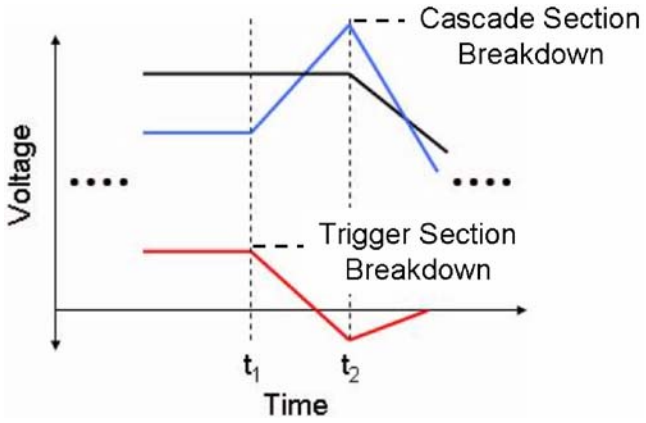

Figure 6: Breakdown sequence in Rimfire switch. Black: voltage across the entire switch. Blue: voltage across the cascade section. Red: voltage across the trigger section. All voltages are with respect to ground.

2.3 Multichannel Operation

Multichanneling is the result of parallel channels in a single gap. Conclusions as to the exact cause of and parameters for multichanneling have not been completed. However, there have been several studies in the area of multichanneling in toroidal gaps [2,6,7]. One parameter of interest is the resistive phase of the arc. This is given by equation (3) where p is the pressure in atmospheres, E is the electric field in MV/m, and Z is the characteristic impedance of the circuit in Ohms. After one arc is initiated, if another arc forms before the resistive phase is finished (the arc resistance is below a certain value), then both arcs will possibly carry significant current [2].

$$\tau_r = \frac{88 \cdot p^{1/2}}{Z^{1/3} E^{4/3}} \text{ [ns]} \tag{3}$$

CHAPTER 2 REFERENCES

[1] G.Schaefer, *Gas Discharge Closing Switches*, Plenum, 1991.

[2] J.C.Martin, "Switching," in *J.C. Martin on Pulsed Power,* Plenum Press, 19910, pp. 261-366.

[3] T.H.Martin, "Pulse Charged Gas Breakdown," in *Proceedings of the 5th IEEE Pulsed Power Conference*, Arlington, VA, 1985.

[4] T.H.Martin, "An Empirical Formula for Gas Switch Breakdown Delay," in *Proceedings of the 7th IEEE Pulsed Power Conference*, Monterey, CA, 1989.

[5] T.Nitta, N.Yamada, and Y.Fujiwara, "Area Effect of Electrical Breakdown in Compressed SF6," *IEEE Transactions on Power Apparatus and Systems*, vol. 93, no. 2, pp. 623-629, Apr.1974.

[6] K.R.LeChien, "A Study of a Multi Channeling Spark Gap Switch." Master of Science Thesis, University of Missouri-Columbia, 2002.

[7] S.Futuya, Y.Watanabe, T.Yoshikawa, S.Takano, and J.Irisawa, "Characteristics of Multichannel Arc Gap," *Japanese Journal of Applied Physics*, vol. 40, no. 2B, pp. 987-991, 2001.

CHAPTER 3

SWITCH MODEL

This chapter details the development, verification, and results from an advanced circuit model of the Rimfire switch. With this model, past models were verified and extended. It was shown that in some situations, this model provides advantages over past models and gives new insight into the operation of the switch. The main strength is its flexibility to simulate many different versions of the Rimfire switch in many different switching situations.

3.1 Circuit Model Development

Sandia already utilizes circuit models to describe the behavior of the Rimfire switch. Simple switch circuit models have effectively modeled the performance of the switch when incorporated into an overall system circuit. Figure 7 shows the topology of a typical simple circuit model. While adequate and effective for determining macroscopic switch characteristics, internal switch

characteristics such as runtime are undetectable. In addition, electrical effects of geometry changes to the switch may not be easily realizable because this model does not include stray capacitances. For this reason, an advanced circuit model (the UMC circuit model) was developed.

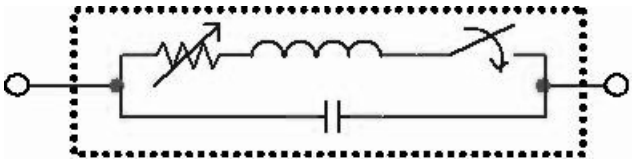

Figure 7: Simple circuit model of the Rimfire switch.

3.1.1 Cascade Gap Model

A more advanced circuit model, the UMC circuit model, was made by including every gap and conductor of the switch in the circuit rather than lumping them all into a few elements. Each individual spark gap has a model similar to Figure 7, which is placed in series. The capacitance values from every conductor in the switch to every other conductor were generated from electrostatic simulations. Figure 8 shows the general layout.

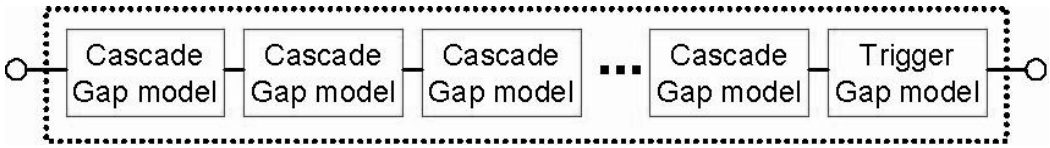

Figure 8: Layout of cascade circuit model.

The entire UMC circuit model can be inserted as a two terminal switch in a system model where the circuit of Figure 7 would normally be placed. The

strength of the UMC model is that while the whole model macroscopically performs like a switch, every gap has an independent closing time and individual time-varying parameters. This allows analysis of the time-varying voltage and current at each part of the switch.

3.1.2 Conduction Characteristics

The first task completed in developing the UMC model was to determine the Rimfire switch on-state conduction characteristics to be utilized in the model. General switch characteristics are known for several versions of the Rimfire switch. These switch characteristics were fit to experimental results and values such as inductance and resistance were extrapolated. In addition, theoretical calculations exist to support the experimentally generated values [1].

For calculating the switch inductance, the methodology is the same as previously published work [1]. Simplified equations from Grover were utilized to calculate inductance for various geometries in the Rimfire switch [2]. Equation (4) is the general inductance equation for a coaxial geometry. Equation (5) is for a coaxial geometry as well, but with an inner conductor of numerous discrete conductors (similar to the arcs in the cascade section of the Rimfire switch). The inductance, *L,* is given in nanohenrys and all lengths are in centimeters. For equations (4) and (5), the outer radius of the outer conductor is ρ_1, the outer radius of the inner conductor is ρ_3, and the length of the conductors is *l*. For equation (5), *a* is the distance from each inner conductor to the center of the coaxial conductor, ρ is the radius of each inner conductor, and *n* is the number of

inner conductors. It is interesting to note that, given the same conductor radius values, the inductance given by equation (5) approaches the inductance given by equation (4) as *n* approaches infinity [1].

$$L = 2 \cdot l \cdot \ln \frac{\rho_1}{\rho_3} \quad \text{[nH]} \tag{4}$$

$$L = 2 \cdot l \cdot \left(\ln \frac{\rho_1}{a} + \frac{1}{4n} + \frac{1}{n} \cdot \ln \frac{a}{n\rho} \right) \quad \text{[nH]} \tag{5}$$

For the time varying resistance of an arc, several equations are commonly utilized. Equation (6) is a resistance model used in the Screamer circuit code [3]. Resistance and impedance (*R* and *Z*) are in Ohms and the decay constant τ is in seconds. Equations (7) and (8) come from reference [4] which utilizes Braginskii's spark channel formation theory [5]. For equation (8), C_{BRAG} is a constant which varies by switch dielectric, a(t) is the radius of the arc in meters, and *I* is the current through the arc in Amperes. Equations (9) and (1) come from a sigmoid function defined by Rosenthal [6]. The symbols *a*, σ_{max}, and Δ are constants dependent on the characteristics of the switch dielectric and $\sigma(t)$ is the arc conductivity in Siemens/meter. Approximate values for some of the constants are shown in Table 3. Each of these models for the resistance of an arc can be used in the UMC model.

For the UMC circuit model, the resistance and inductance values derived using equations (4) – (10) were distributed over every gap. For example, for a

$$R(t) = R_{close} + \frac{Z_{switch} \cdot e^{-t/\tau}}{1 - e^{-t/\tau} + Z_{switch} \cdot 10^{-6}} \tag{6}$$

$$R(t) = \frac{l}{\sigma \pi a(t)^2} \tag{7}$$

$$a(t)^2 = (C_{BRAG})^{1/3} \int_0^t I^{2/3} dt \tag{8}$$

$$R(t) = \frac{l}{\sigma(t) \pi a^2} \tag{9}$$

$$\sigma(t) = \frac{\sigma_{\max}}{e^{-(t - t_{BD} - \Delta)/\tau} + 1} \tag{10}$$

Table 3: Approximate values of constants used in equations (6)-(10).

C_{BRAG} [4]	.091
a [7]	.7 mm
τ [6]	.2 ns
σ, σ_{max} [6]	160 $(\Omega\text{-cm})^{-1}$
Δ [6]	1.3 ns

given version of the switch, using equation (5), the inductance of the cascade section is found to be 400 nH. There are 25 gaps in the cascade section, so the inductance per gap model would be 400 nH divided by 25 gaps, or 16 nH per gap. The hemispherical trigger section inductance was calculated using equation (4) and it is not reduced further from the calculated value.

3.1.2 Electrostatic Field Simulation and Verification

The next step in the development of the UMC model involved finding the values of stray capacitance. Using Maxwell 2-D, the capacitance from every conductor in the switch to every other conductor was calculated [8]. This was achieved by using the electrostatic simulation results and the generated capacitance values. For the switch, each metal part was considered to be a single conductor and therefore a single node in the circuit model. Figure 9 illustrates a small four-electrode system example of how these capacitance values are defined. Figure 10 shows a plot of equipotential lines and electric field vectors produced by Maxwell 2-D. 6 MV is used because this is the operating voltage of the *PBFA-II-Z* switch used in the simulations. The generated capacitance values were inserted into the PSpice circuit as discrete capacitors. For simplicity, some small capacitance values (<~0.005 pF) were omitted from the model. For a typical Rimfire switch, this method of capacitance calculation resulted in ~400 capacitors in the circuit model. Appendix A gives a list of these capacitance values for the ZR baseline switch.

The validity of this method of exporting capacitance values was checked by simulating the circuit model before breakdown occurred. Capacitance values generated (with nodes separated by open circuits) were placed into the CLC circuit of Figure 11. If the method of exporting and capacitance implementation methods is valid, the result of electrostatic simulation from Maxwell should match the PSpice results. This allows a 3D problem to be simulated by a 1D-

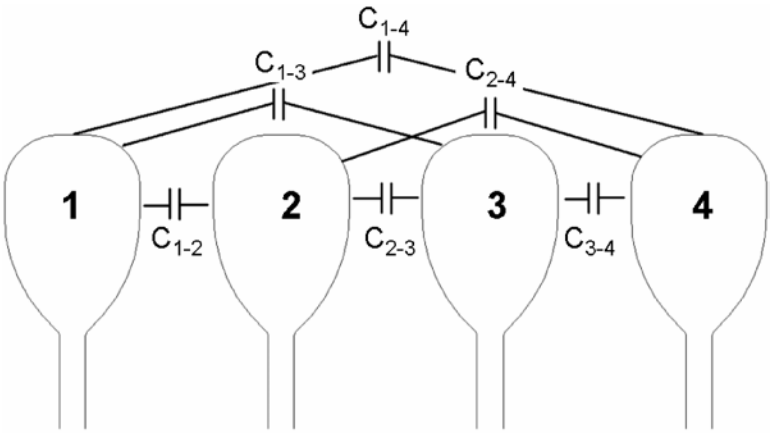

Figure 9: Electrode-to-electrode capacitance values for a simple four electrode system.

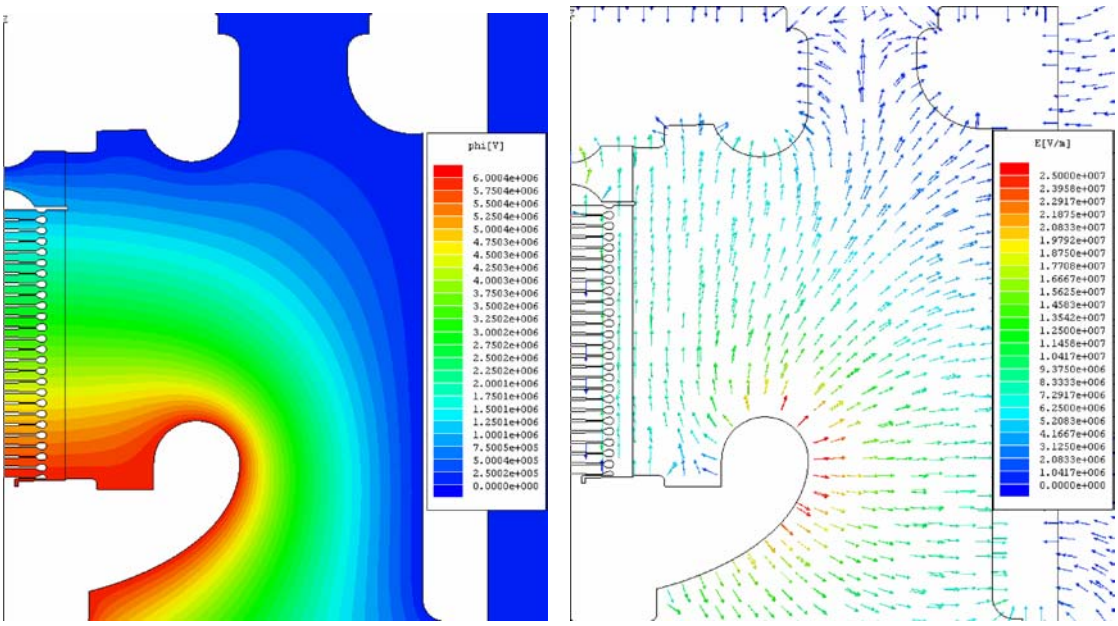

Figure 10: Maxwell 2-D electrostatic simulation with 6 MV across switch. Left: Equipotential lines. Right: Electric field vectors.

circuit code. The PSpice capacitance model was pulse charged until the voltage across it was the same as the simulated voltage across the switch in the Maxwell 2-D model.

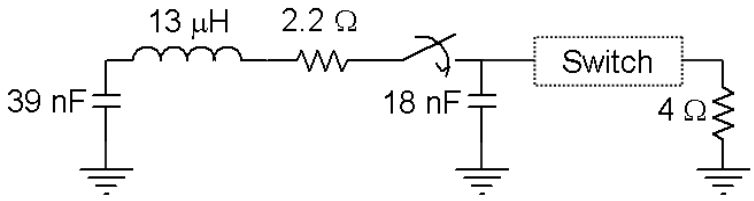

Figure 11: CLC circuit used to evaluate validity of the method of capacitance export.

The voltage with respect to ground of every conductor in the switch was simulated using both Maxwell and PSpice. In both simulations, 6 MV was placed across the switch. This chosen voltage is arbitrary and similar results occured with any pulse charge voltage. Using these values, the voltage across every cascade gap was calculated using the UMC model. The numbering convention used is shown in Figure 12 and the results from both simulations are shown in Figure 13. In the figures, gap 1 is the gap closest to the trigger disk electrode and gap 25 is closest to the end of the switch. As shown, the results are very similar and only differ by +/- 1.3%. Because the results of electrostatic simulation from Maxwell match the PSpice results, the export method and capacitance implementation method is valid.

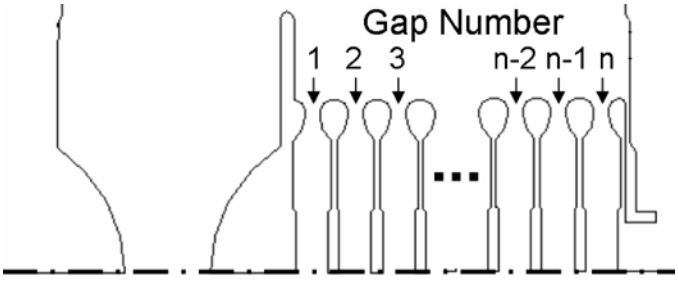

Figure 12: Rimfire gap numbering convention.

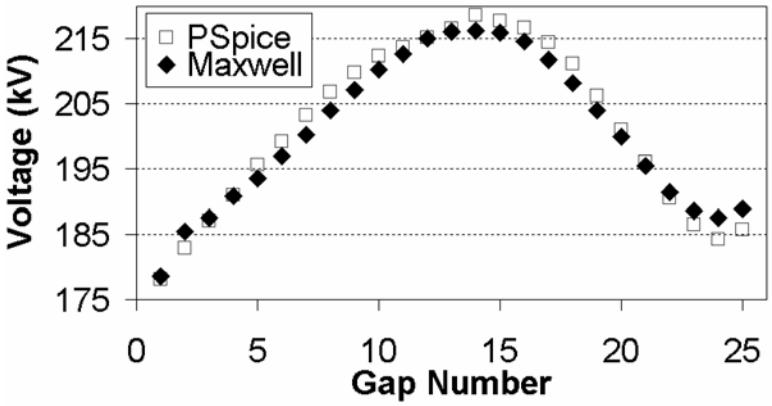

Figure 13: Voltage across cascade gaps for two different simulation methods. Plot shows pre-breakdown voltage grading on the cascade section.

3.1.3 PSpice Implementation

PSpice was used to simulate the UMC circuit model of the Rimfire switch. The circuit layout for a single gap module is shown in Figure 14. There are four objects in the model: an inductor, a voltage controlled current source (VCCS), a module called TIMER, and a biasing resistor. The inductor represents the inductance of a single arc. It is connected in series with the VCCS. The VCCS represents the time-varying resistance of the arc. It is controlled by two inputs: the voltage across the VCCS and a signal from the TIMER module. The output current, given by equation (10), is the voltage across the VCCS divided by a time varying function representing the resistance. The biasing resistor has no function other than to facilitate PSpice convergence.

The TIMER module, shown in Figure 15, triggers gap breakdown and outputs a waveform for the resistance function in the VCCS. Using the voltages across the VCCS, the TIMER module signals breakdown when a threshold voltage is exceeded. Breakdown is assumed to continue until the pulse voltage is

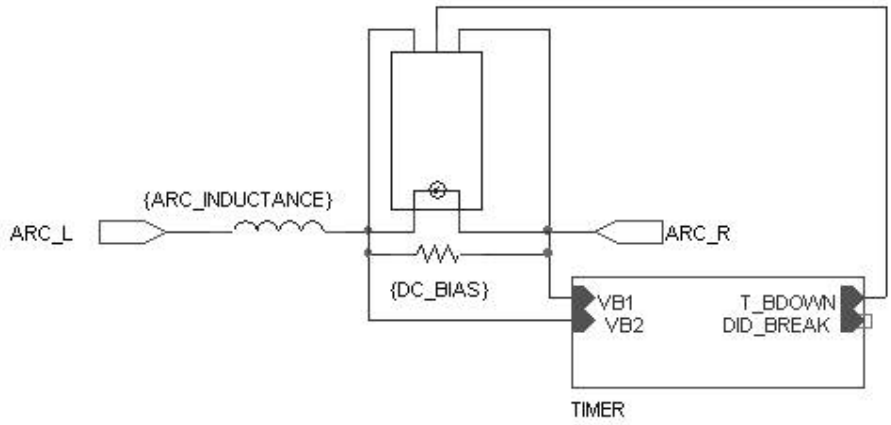

Figure 14: Circuit layout for gap model.

$$I_{VCCS} = \frac{V_{VCCS}}{R_{arc}(TIMER)} \tag{10}$$

removed. The output waveform of the TIMER module is shown in Figure 16. From the point of breakdown, shown in the figure at time=1, the voltage increases linearly with respect to time. For example, if breakdown occurred at t=0.5 μs, the voltage output from TIMER at t=1.5 μs would be 1 μV. The TIMER waveform is directly input as the t variable to a resistance equation such as (6) – (9). The VCCS then acts as a time-varying resistor with a time variable given by the TIMER function. This implementation of a time-varying resistance allows for simple utilization of formulas for arc resistance.

Incorporation of the gap model into PSpice was the final step for the development of the switch model. When a geometry change to the switch is to be evaluated, the switch is first simulated in Maxwell 2-D and generated capacitance values are exported into PSpice. Appropriate values of inductance and resistance

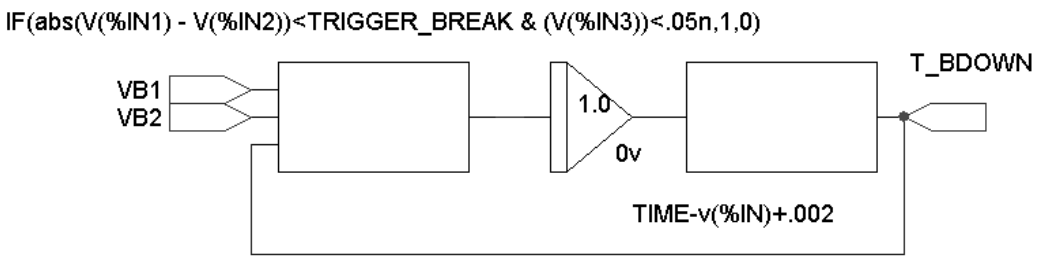

Figure 15: Circuit diagram of the TIMER module.

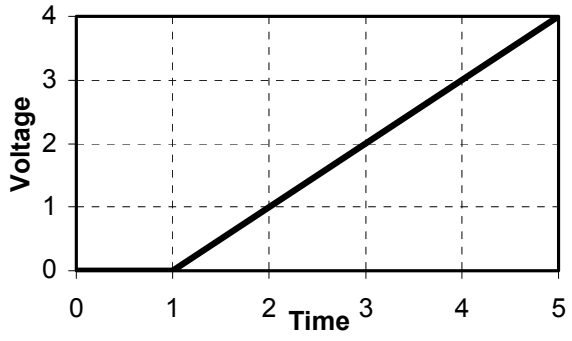

Figure 16: Example TIMER module output waveform. Units of both axes are arbitrary.

are calculated according to equations (4)-(9). The self-break point of the cascade gaps is calculated according to equation (2). Lastly, the desired percentage of self-break for switch triggering is input into the switch model. An example of the switch model is shown in Figure 17. This represents a completed UMC circuit model.

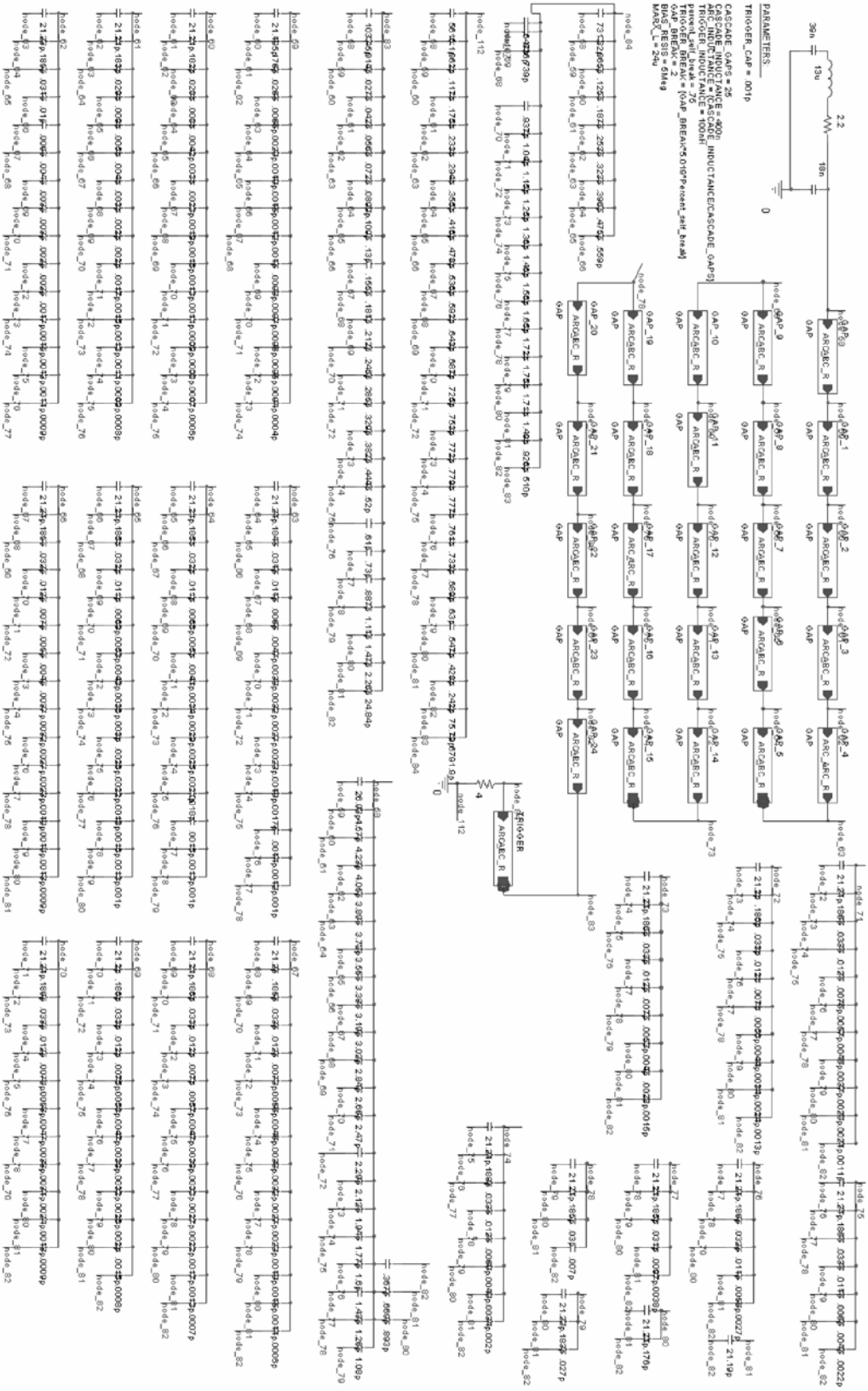

Figure 17: Full circuit model of Rimfire switch. Capacitance values are listed in Appendix A.

3.2 Comparison to Past Results

As mentioned earlier, several methods of modeling as well as experimental results for the Rimfire switch already exist. Comparisons to the UMC model are not always possible; however, in some cases the results can be compared. Consistency was desired, so several parameters were kept constant throughout the simulations. The PSpice parameters are shown in Table 4 and switch parameters (unless specifically noted otherwise) are shown in Table 5. Reltol is the relative accuracy of the simulations. Vntol, Abstol, and Chgtol are the absolute accuracy for voltage, current, and charge respectively. ITL4 is the transient time point iteration limit.

Table 4: PSpice simulation parameters used in all simulations.

Reltol	.0003
Vntol	10 μV
Abstol	10 μA
Chgtol	10 pC
ITL4	150

Table 5: Default switch parameters used in the simulations.

Cascade Gaps	25
Cascade Inductance	400 nH
Trigger Inductance	100 nH
Cascade Gap Breakdown	242 kV
Trigger Gap Breakdown	960 kV
Load	4 Ω

3.2.1 Rosenthal Simulations

One previous model of the Rimfire switch was developed by Rosenthal. A fully electromagnetic model was created using the Sandia EM PIC code

TWOQUICK. The switch was simulated in 2-D and contained all elements of the switch. In the model, the breakdown of the gap was initiated when a threshold electric field was exceeded. After that point, the channel formed and had conductivity given by equation (9) [6].

One of the focuses of Rosenthal was the effect of changing the dielectric in which the switch is submerged from water to oil. Rosenthal found that there were lower electric fields at the gas-water interface on the insulator in oil when compared to water. In addition, effects of outside dielectric variation on runtime were explored [6].

Results from the UMC circuit model were compared to the results from Rosenthal [6]. First, capacitance matrices were generated with water (ε_r=81), then transformer oil (ε_r=2.2) as the outside dielectric. These capacitance values were imported into PSpice and each circuit was simulated while triggered at varying percentages of self-break. The closing times of the cascade gaps with respect to the trigger closing are shown in Figure 18 and Figure 19 for oil and water respectively.

Figure 18 and Figure 19 confirm that water as the outside dielectric induces a longer runtime than oil and that a low percentage self-break trigger causes a longer runtime than when triggered closer to self-break. Rosenthal showed that the trigger runtime for water is 2.5 times that of oil and that the cascade runtime (the time for all cascade gaps to break down) for water was two times that of oil [6]. The UMC model confirmed these results. Runtime numbers are shown in Table 6.

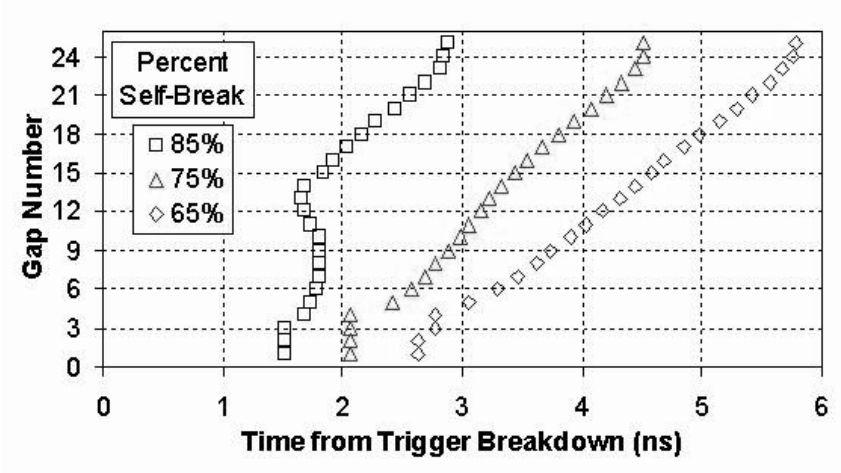

Figure 18: UMC circuit model simulation of cascade gap breakdown times for the Rimfire switch submerged in oil.

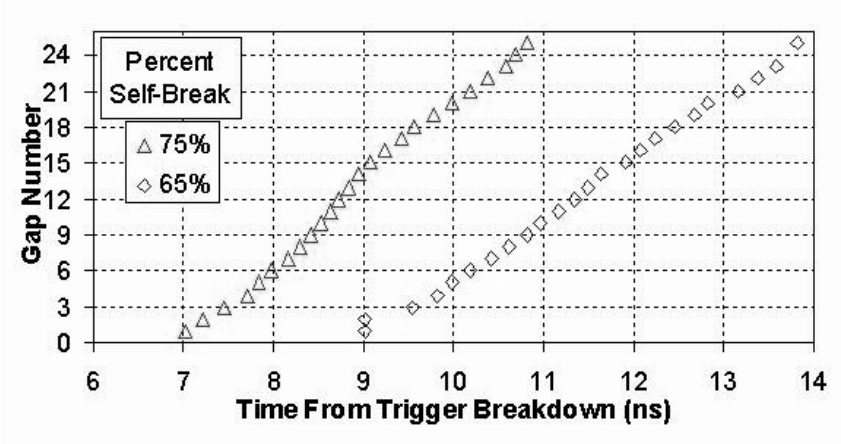

Figure 19: UMC circuit model simulation of cascade gap breakdown times for the Rimfire switch submerged in water.

Table 6: Comparison of runtimes of the UMC model and the Rosenthal model.

	UMC Model	**Rosenthal Model**
Trigger runtime (oil)	2.0 ns	2 ns
Trigger runtime (water)	7.0 ns	5 ns
Cascade runtime (oil)	2.5 ns	7 ns
Cascade runtime (water)	4.0 ns	14 ns

While similar conclusions on trigger runtime and the effect of oil and water on runtime may be gathered from both models, the values of cascade

runtime are drastically different. The cascade runtimes of Rosenthal are more than twice the UMC model. One explanation is that the cascade section inductance used in the Rosenthal model may be significantly different from that used in the UMC model. Section 3.2.3 investigates the issue of runtime further and a number of explanations are presented. A limit of the Rosenthal model was that it could not incorporate outside circuit effects into the simulation of the switch. For simulations, a static voltage was placed across the switch.

3.2.2 Past Circuit Simulations

Circuit models of varying complexity of the Rimfire switch have been used previously. One such circuit was a simple cascade model completed by Humphreys [9]. Methods of resistance and inductance calculation were not provided, few capacitance values were utilized in the model, and the gap breakdown was triggered artificially. Specific results were not quoted. However, it was mentioned that LC oscillations of voltage across the cascade electrodes were observed. This may be a beneficial effect because it maintains discharges in the gaps until the entire switch conducts current [9]. A circuit model and results were also provided by Elizondo [10]. This model was used to investigate the hybrid switch. The capacitance values utilized in the model were limited and were not generated from field simulations.

To evaluate the validity of the method of dividing resistance and inductance across the entire cascade section, both the simple switch model of Figure 7 and the UMC switch model were simulated in the circuit of Figure 11.

The same overall resistance and inductance values were utilized for both models. The only expected difference between the two results would be the runtime delay generated by the full circuit model. Results for one set of simulations are shown in Figure 20. It was found that regardless of inductance and resistance model used for both simulations, the UMC model did not vary greatly from the simple model. The two-element circuit model and the many-element UMC model had a very good match. Therefore, there is minimal late-time difference between using a single inductor and resistor for a switch model and using these values divided over many gaps.

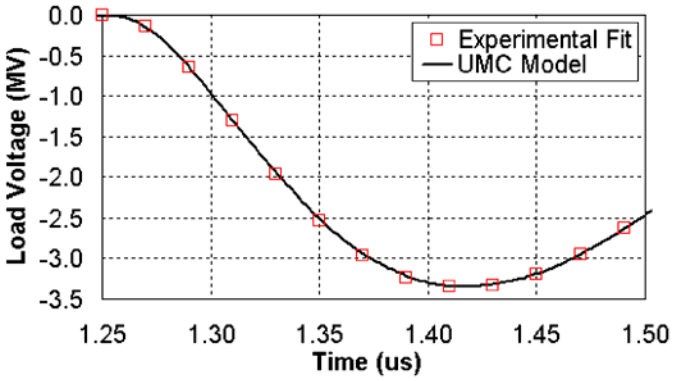

Figure 20: Simulated load voltage for the experimentally fit and UMC circuit models.

Another circuit model was developed by Volkov [15]. Although Volkov did not explicitly state the circuit model that he used to obtain the results of figure 2 of his study (as shown by solid lines in Figure 21), an educated guess can be made as to the parameters used in the model. Using curve-fitting techniques, a fit (as shown by dashed lines in Figure 21) was made to their data. The plot shows electrode voltages with respect to ground for a pulsed charged switch that breaks

down at ~1.015 μs. Trace 1 is a trigger cascade electrode, trace 2 is the trigger disk electrode, and traces 3 and 4 are cascade electrodes [11]. Although the usefulness of this data fit is limited, it was concluded that similar techniques to those presented in this paper were used to generate his circuit model results. Exact switch parameters, model topology, and switch geometries are not provided, so direct comparison is not possible.

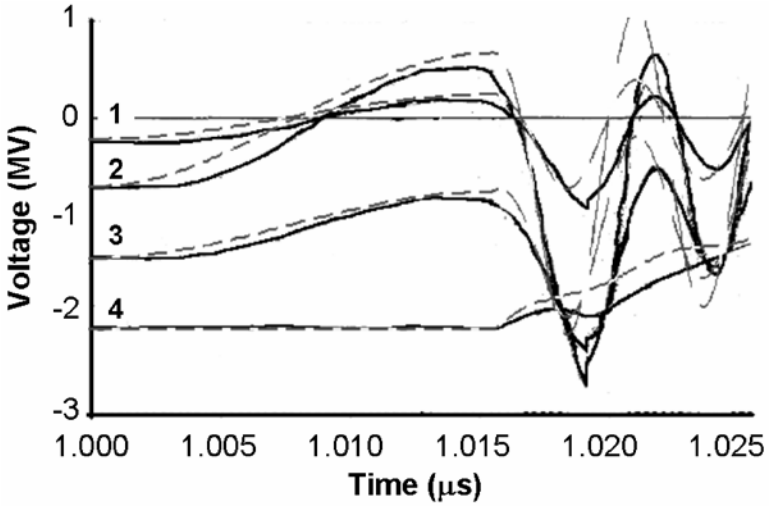

Figure 21: Comparison of circuit model from Volkov (solid line) and UMC circuit model (dashed line) [15].

Using the UMC circuit model, a plot, Figure 22, similar to the one presented by Volkov, is generated [11]. Trace 1 is the load-side endplate of the switch, trace 2 is for the trigger disk electrode, and traces 2 through 7 are every fifth cascade electrode. Trace 7 is the end cascade electrode. At ~1125 ns, the trigger section breaks down and a few nanoseconds later, the first cascade gap breaks down. The load voltage peaks at around 1260 ns.

After switch breakdown, the voltage of the cascade electrodes oscillated at a high frequency. Past studies have experimentally verified these oscillations to exist. The arc inductance and cascade electrode capacitance form a high-Q resonant circuit. These oscillations may have both positive and negative effects. Short continuation of this ringing may maintain discharges in the cascade gaps until current flows through the switch as a whole. However, long-term oscillations may cause stress on the insulators in the switch [9].

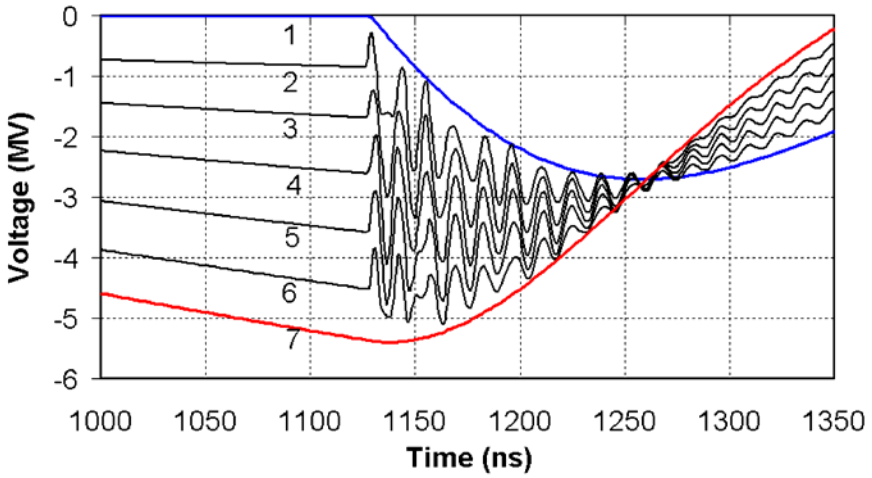

Figure 22: Electrode voltage with respect to ground for the Rimfire switch.

3.2.3 Runtime Experiments

Runtime in the Rimfire switch has been explored in several studies. The significance of this parameter is that it has been shown that there is a strong correlation between runtime and jitter. As shown in Figure 23, reduction in runtime drastically reduces jitter [12]. Several factors have been shown to effect runtime including switch length, number of cascade electrodes, percent of self-break that the switch is triggered, the dielectric in which the switch is submerged,

and the pre-breakdown grading of the fields along the switch. This section looks at a few of these parameters as they relate to the UMC model.

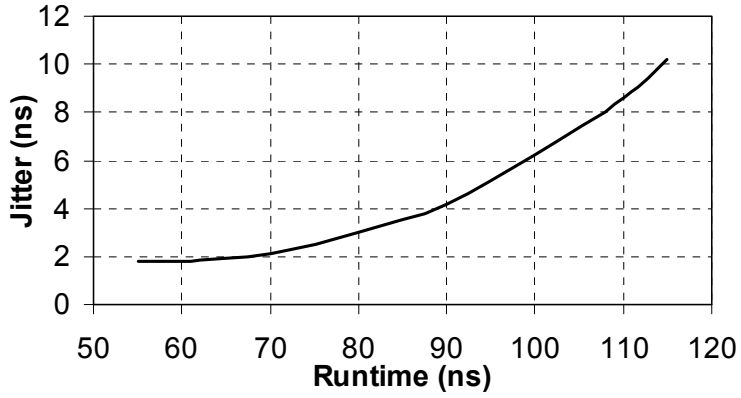

Figure 23: Relation of jitter to runtime for one version of the Rimfire switch (from Wilson [11]).

When evaluating runtime, the first issue to resolve is to determine exactly how the parameter is to be measured. Most publications define it as the time from laser pulse arrival until the voltage on the intermediate store begins to drop. This implies that the UMC circuit model underestimates runtime values because it does not include the formation time of the arc after laser arrival. In addition, even though all arcs may be formed in the switch, there is a time delay from when the voltage begins to drop on the intermediate store. Wilson uses a different definition of runtime: "the time between arrival of the laser at the trigger gap and the zero-crossing of a V-dot monitor located in the middle of the intermediate storage capacitor" [12]. Turman utilized all optical data to measure the closure times in the switch. However, runtime in his experiments was greater in both trigger and switch runtime when the values would be thought to be an underestimation compared to the other experiments [13]. Table 7 shows a

comparison of runtime values from many different sources. For the UMC model, runtime was measured from the closure of the trigger gap until voltage reduction on the intermediate store. Except for the optical evaluation of runtime by Turman, all studies give approximately the same values of runtime.

Table 7: Comparison of overall and trigger runtimes by various studies. All are for the Rimfire switch submerged in water.

	Switch Runtime (ns)	**Trigger Runtime (ns)**
UMC Model: Self-break	14.0	6.2
Rosenthal Model [6]	19.0	5.0
Humphreys [9]	19.5	4.8
Turman [14]	32.0	7
Denison- 1987 [15]	24.0	*n/a*
Denison- 1989 [16]	14.0	6.0
Corley [17]	24.0	*n/a*

Because of the many factors that effect runtime, it is not possible to compare the runtime values. However, it is possible to determine the relative effects of some factors on runtime. In section 3.2.1, the UMC model was compared to the model of Rosenthal. The relative effect of the outside dielectric on runtime was confirmed. Experimentally, the same phenomenon was noted by Denison, "It is interesting to note that the switch 'ran' ~30 ns faster in the STF oil tank than it did when tested in a water tank. This difference appears to be the result of the time it takes for the fields to redistribute themselves, in the oil or water, after the gas gaps have closed." [15]

A second runtime parameter, the effect of triggering at a percentage of self-break, was also studied by Denison. His results are compared to the UMC model in Table 8. Denison showed that for a given version of the Rimfire switch,

switches triggered at 65% of self-break compared to switches triggered at 85% of self-break had twice the runtime. Compared to the Denison experiments, the UMC model underestimates the effect of percent self-break on runtime [15]. One possibility for this underestimation is the lack of incorporation of parameters such as streamer velocity and transit time into the UMC model. One way to address this issue is to incorporate transmission line models between electrodes.

Table 8: Switch runtime for percentage of self-break. All results for the Rimfire switch submerged in water.

Percent Self-Break	UMC Model	Denison Experiments [15]
65%	21.5 ns	47.0 ns
75 %	15.5 ns	35.0 ns
85%	14.7 ns	24.0 ns
95%	14.0 ns	20.0 ns

Several studies have been conducted which investigate the effects of the trigger laser on switch runtime. Because the UMC model does not incorporate laser parameters, comparison to these studies is not possible. However, it is noted that the trigger laser parameters such as peak power, wavelength, and pulse width have significant effects on runtime [13].

3.3 Electrical Results of Switch Geometry Alterations

This section presents four studies on switch geometry alterations. Variation of the surrounding dielectric, implementation of MID electrodes, addition of a hybrid trigger section, and development of an all-cascade switch are explored. Effects on electrical parameters are calculated.

3.3.1 Outside Dielectric

As mentioned earlier, the dielectric constant of the liquid in which the switch is submerged has large effects on the electrical operation of the switch. One effect is shown in Figure 24. The switch was simulated submerged in oil and then water. The switch broke down at significantly different times and produced different load currents. For Figure 24, the breakdown times are manually aligned to ~1250 ns. The switch submerged in water had much higher stray capacitances than the switch in oil. For example, the capacitance from end plate to end plate was 731 pF in water but only 17 pF in oil. The energy stored in this capacitance prior to breakdown discharged through the load and produced a higher current. However, the risetime of the current was also much larger.

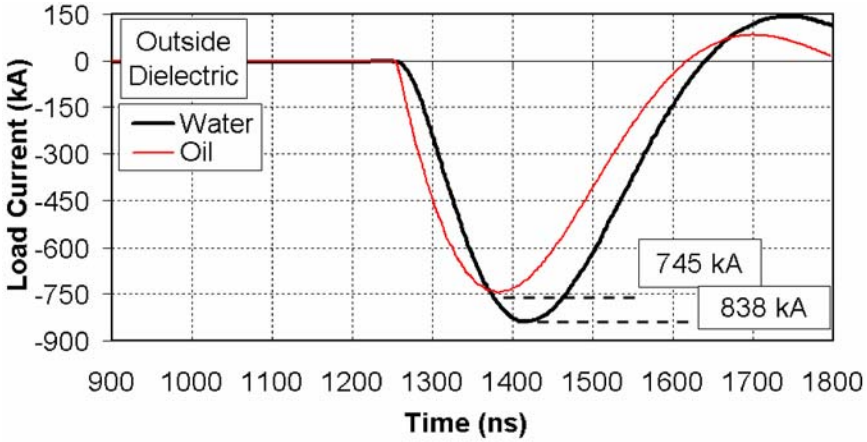

Figure 24: Load current with switch submerged in oil and water. Breakdown times are aligned for comparison.

3.3.2 Metal Insert Dielectric Electrodes

Several electrode geometries have been proposed other than the toroidal electrodes presently utilized in the Rimfire switch. One possibility is the electrode

shown in Figure 25 that was presented by Volkov. This electrode is a dielectric disk with metal inserts around the perimeter. An advantage of this is that multichanneling is forced around the perimeter. Additionally, azimuthal electrode currents are eliminated because current cannot flow through the dielectric [11]. This is beneficial because azimuthal currents possibly contribute to increased switch inductance [18]. In addition, using toroidal electrodes anywhere from one to twelve arcs can occur in a given gap. If there are a consistently larger average number of arcs per gap, a lower switch inductance may result. These electrodes may provide these conditions.

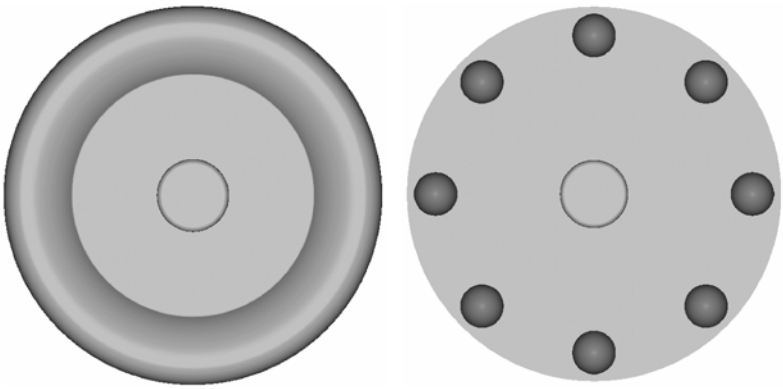

Figure 25: Left: Original toroidal electrode. Right: Dielectric electrode with metal inserts.

One attribute of these electrodes is the electrode-to-electrode capacitance is greatly reduced. The Rimfire switch was simulated with these electrodes. Capacitance for the dielectric electrode was overestimated because of the 2D limitation of Maxwell. One result using the UMC model is shown in Figure 26. The plot shows the voltage of the floating trigger electrode. The switch broke down at ~1029 ns. There appears to be little difference between the electrodes except that the dielectric electrode had slightly smaller variations in voltage

amplitude. Figure 26 underestimates this effect because the simulations may have had had a larger capacitance than the actual dielectric electrodes.

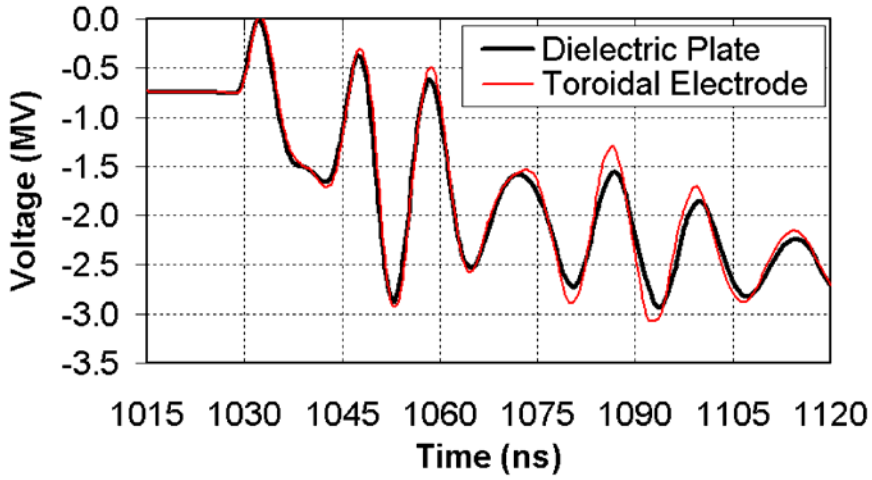

Figure 26: Comparison of floating trigger electrode voltage with respect to ground for two different electrodes.

3.3.3 Hybrid Switch

Another version of the Rimfire switch is the hybrid Rimfire switch, as shown in Figure 27. The difference between this version and previous versions is that the cascade gaps, label 1, are added in parallel to the existing hemispherical electrode trigger section, label 2. In addition, a large inductor (~3 μH), label 3, is placed in series with the hemispherical electrodes. The switch is triggered in the same manner as the previous Rimfire switches, but after the main cascade section breaks down, the parallel cascade electrodes self break and carries the bulk of the trigger section current instead of the hemispherical electrodes. The purpose of the inductor is to force a slower dv/dt on the trigger disk electrode to allow the trigger cascade electrodes to break down. As will be shown later, removal of this

inductor inhibits the parallel cascade electrodes from breaking down. A secondary purpose is to further limit the current through the hemispherical electrodes, thereby reducing hemispherical electrode erosion [11,17].

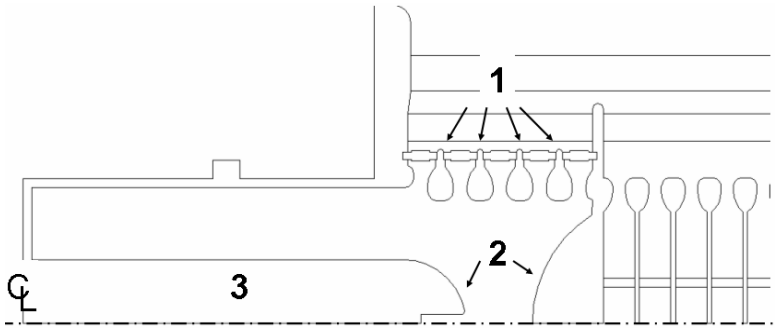

Figure 27: Drawing of the hybrid Rimfire switch trigger section.

This version of the Rimfire switch has two main advantages. The first advantage is that with the added electrodes, the entire switch conducts with multichannel arcs. Previously, in the trigger section, the current was limited to only one channel. This single channel has higher inductance than the multichannel cascade trigger electrodes. The second advantage of the current not flowing in one large channel is that the negative effects of erosion are minimized. Random, multiple arcs on the toroidal electrodes erode the electrodes less than a location forced, single arc [11].

One result of simulating the hybrid switch is shown in Figure 28. Increasing the series inductance to over 2 μH did not significantly reduce hemispherical electrode current. Therefore, if a reduced hemispherical current is desired, increasing the series inductance is not a practical method. However, it was found that if the series inductance was decreased less than ~1.6 μH, the

trigger cascade electrodes did not break down and the switch had an inductance approximately equal to the series inductor. This is because the value of the added trigger inductance (~2.5 μH) is much larger than the inductance of the switch (~.5 μH). If the cascade trigger electrodes do not break down, the total trigger section inductance is no longer the parallel combination of the added inductance and the trigger cascade electrodes, but only the added inductance.

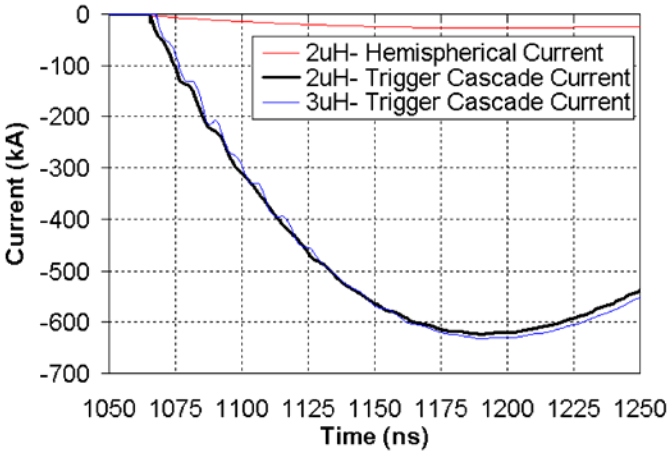

Figure 28: Currents with added trigger inductance

In a paper presenting experimental results on a Rimfire switch with a non-hybrid trigger section, Corley found switch runtime to be 24 ns [17]. When evaluating one version of the hybrid trigger switch immersed in oil, he stated that switch runtime was ~40 ns, but insufficient data existed to determine jitter. The tests of a hybrid switch in a water dielectric resulted in jitter with a ~20 ns spread. The non-hybrid switch shots had low jitter and runtime, but the hybrid switch shots had high jitter and runtime. However, Corley attributes the poor hybrid performance to a large field anomaly in the trigger section and states, "...trigger gap closure is not dependent on voltage reversal with the LC time

constant of the isolation inductor and trigger capacitance as had been explored" [19]. As shown in Table 9, the UMC circuit model simulations showed that increases in the series inductance increased trigger runtime. This shows that with the current hybrid switch configuration, it may not be possible to attain low runtimes as in the non-hybrid switch.

Table 9: Simulated hybrid switch trigger section runtimes.

Trigger Inductor (μH)	Trigger Runtime (ns)
None (original switch)	1.5
2	6.7
3	7.8
4	9.3

3.3.4 Advanced Triggering Methods

As will be shown in the next chapter, the existing trigger section becomes a limiting factor when designing a low inductance gas switch. The hybrid switch presented in the previous section is one possible solution. A possible drawback of that design is that with the added trigger inductor, there is added runtime, and therefore jitter, to the switch. One separate possibility is the all-cascade switch shown in Figure 29.

If the entire Rimfire switch were comprised of toroidal electrodes, the entire switch would multichannel. However, triggering of this version of the switch is non-trivial. Triggering of the Rimfire switch achieves two goals: breakdown of the switch is temporally controlled and it increases the dv/dt across the cascade electrodes dramatically. Multichanneling may be more prevalent with shorter applied voltage pulses (large dv/dt).

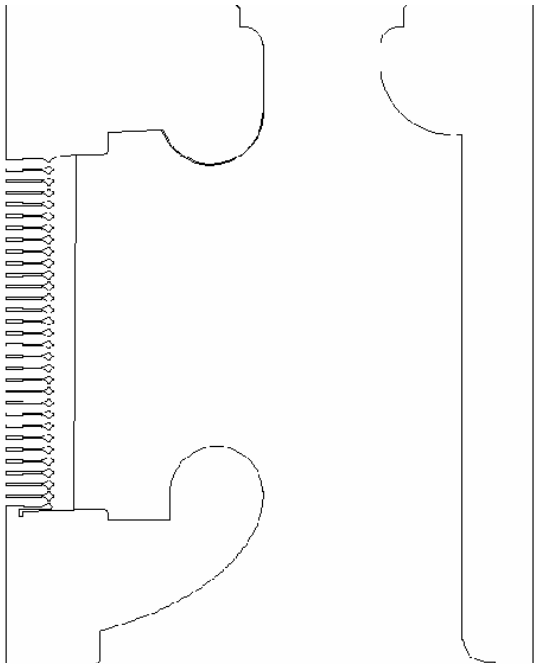

Figure 29: All-cascade Rimfire switch drawing.

Laser energy would need to be split into several trigger beams to ensure multichanneling in the “trigger section” gaps. In addition, because smaller trigger sections have been shown to cause larger switch runtimes, the laser would need to penetrate several gaps to effectively trigger the switch [20]. The UMC circuit model was used to evaluate the number of cascade gaps required to be triggered by the laser to ensure low switch runtimes. One, two, or three gaps were manually closed at various switch self-break voltages. Runtime was both measured as the time from first to last gap closure (runtime 1) and as time from first gap closure to voltage reduction on the intermediate store (runtime 2). Results are shown in Table 10.

Table 10: Runtime for various numbers of gaps triggered in the all-cascade switch.

		1 Gap	2 Gap	3 Gap
90% Self-Break	Runtime 1	1.75 ns	1.7 ns	1.75 ns
	Runtime 2	12.7 ns	13.7 ns	13.7 ns
80% Self-Break	Runtime 1	8.7 ns	1.7 ns	1.75 ns
	Runtime 2	21.1 ns	16.3 ns	16.08 ns
70% Self-Break	Runtime 1	191.8 ns	7.6 ns	4.38 ns
	Runtime 2	199.7 ns	23.2 ns	20.4 ns

For the case where only the first gap is triggered at 70% self-break, the switch could not be triggered. In addition, the 80% self-break simulation had a large runtime. However, the addition of more gaps directly triggered by the laser trigger ensured lower runtimes.

CHAPTER 3 REFERENCES

[1] J.M.Elizondo, K.W.Struve, J.P.Corley, and D.L.Johnson, "Inductance Calculation for the Rim-Fire Multi-Channel Switch," ZR Technical Note, Num. 5, 2002.

[2] F.W.Grover, *Inductance Calculations*, Dover, 1962.

[3] M.L.Kiefer, K.L.Fugelso, and M.N.Widner, "SCREAMER: A Pulsed Power Design Tool," Sandia National Laboratories Internal Report, Num. 6-26-1991.

[4] T.H.Martin, J.F.Seamen, and D.O.Jobe, "Energy Losses in Switches," *in Proceedings of the 9th IEEE Pulsed Power Conference*, Albuquerque, NM, 1993.

[5] S.I.Braginskii, "Theory of the Development of a Spark Channel," J.Exptl.Theoret.Phys.(U.S.S.R.), vol. 34, no. 1, pp. 1548-1557, June1958.

[6] S.E.Rosenthal, J.M.Elizondo, J.E.Maenchen, K.W.Struve, D.H.McDaniel, J.P.Corley, D.L.Johnson, and B.V.Oliver, "Modeling 6-MV Gas Switches For the ZR Accelerator," *in Proceedings of the 14th IEEE Pulsed Power Conference*, Dallas, TX, 2003.

[7] J.C.Martin, "Switching," in J.C. Martin on Pulsed Power, Plenum Press, 19910, pp. 261-366.

[8] Ansoft Corp., Pittsburgh, PA.

[9] D.R.Humphreys, K.J.Penn, J.S.Cap, R.G.Adams, J.F.Seamen, and B.N.Turman, "Rimfire: A Six Megavolt Laser-Triggered Gas-Filled Switch for PBFA II," *in Proceedings of the 5th IEEE Pulsed Power Conference*, Arlington, VA, 1985.

[10] J.M.Elizondo, J.P.Corley, L.Bennett, K.W.Struve, K.Prestwich, D.L.Johnson, and J.Maenchen, "Laser Triggered Hybrid Switch," ZR Technical Note, Num. 15, 2002.

[11] S.N.Volkov, A.A.Kim, B.M.Kovalchuk, V.V.Kremnev, and V.A.Sinebryukhov, "MV Multi Channel Closing Switch for Water Storages," *in Proceedings of the 12th IEEE International Pulsed Power Conference*, Monterey, CA, 1999.

[12] J.M.Wilson and G.L.Donovan, "Laser-Triggered Gas Switch Improvements on PBFA-II," *in Proceedings of the 6th IEEE Pulsed Power Conference*, Arlington, VA, 1987.

[13] B.N.Turman, A.E.Rodriguez, and K.J.Touryan, "Experimental and Analytical Study of Laser-Triggering in the Rimfire Switch," *in Proceedings of the 8th IEEE Pulsed Power Conference,* San Diego, CA, 1991.

[14] B.N.Turman, D.R.Humphreys, and C.N.Richards, "Interstage Closure Times for the Rimfire Multistage Gas Switch," *in Proceedings of the 7th IEEE Pulsed Power Conference,* Monterey, CA, 1989.

[15] G.J.Denison, J.P.Corley, D.L.Johnson, G.J.Weber, R.A.Hamil, G.W.Crowder, J.A.Alexander, D.A.Petmecky, L.P.Schanwald, and J.J.Ramirez, "A High-Voltage Multistage Laser-Triggered Gas Switch," *in Proceedings of the 6th IEEE Pulsed Power Conference*, Arlington, VA, 1987.

[16] G.J.Denison, J.A.Alexander, J.P.Corley, D.L.Johnson, K.C.Hodge, M.M.Manzanares, G.Weber, R.A.Hamil, L.P.Schanwald, and J.J.Ramirez, "Performance of the Hermes-III Laser-Triggered Gas Switches," *in Proceedings of the 7th IEEE Pulsed Power Conference,* San Diego, California, 1989.

[17] J.P.Corley, M.A.Dixon, A.A.Kim, B.M.Kovalchuk, V.A.Sinebryukhov, S.N.Volkov, K.C.Hodge, S.A.Drennan, J.M.Navarro, D.L.Johnson, G.Avrillaud, and F.Lassalle, "Tests of 6-MV Triggered Switches on APPRM at SNL," *in Proceedings of the 13th IEEE International Pulsed Power Conference*, Las Vegas, NV, 2001.

[18] K.R.LeChien and J.M.Gahl, "Investigation of a Multichanneling, Multigap Marx Bank Switch," Review of Scientific Instruments, vol. 75, no. 1, pp. 174-178, Jan.2004.

[19] J.P.Corley, K.C.Hodge, S.A.Drennan, D.W.Guthrie, J.M.Navarro, D.L.Johnson, J.M.Lehr, S.E.Rosenthal, and J.M.Elizondo, "Development/Tests of 6-MV Triggered Gas Switches at SNL," *in Proceedings of the 14th IEEE International Pulsed Power Conference*, Dallas, TX, 2003.

[20] B.N.Turman and D.R.Humphreys, "Scaling Relations for the Rimfire Multi-Stage Gas Switch," *in Proceedings of the 6th IEEE Pulsed Power Conference*, Arlington, VA, 1987.

CHAPTER 4

EXPERIMENTAL EVALUATION

Some improvements to the Rimfire switch cannot be made solely through simulation; experimental analysis is necessary. This chapter presents an experimental study of the multichanneling section of the Rimfire switch. The effects of multichanneling and a method to force multichanneling are presented. In addition, an objective curve fitting method is utilized to deduce switch inductance from the measured data.

4.1 Revised MUTTS Circuit Diagram

A previously published circuit diagram of MUTTS is presented in section 1.3. This circuit is adequate to match some data, but it requires changes to the system parameters to gain a good fit for some shots. For this reason, a new circuit model was derived to match data. All parameters except the Marx bank itself and the switch were derived from theory. As stated earlier, the Marx bank used in

MUTTS is from a module of the Proto II machine. Characteristics of this Marx are presented in reference [1]. The reported values were the basis for the MUTTS system model, shown in Figure 30. The main difference between this system model and the model in Figure 3 is that none of the circuit (except for the Marx bank parameters) elements were found from curve fits; all are derived from transmission line equations.

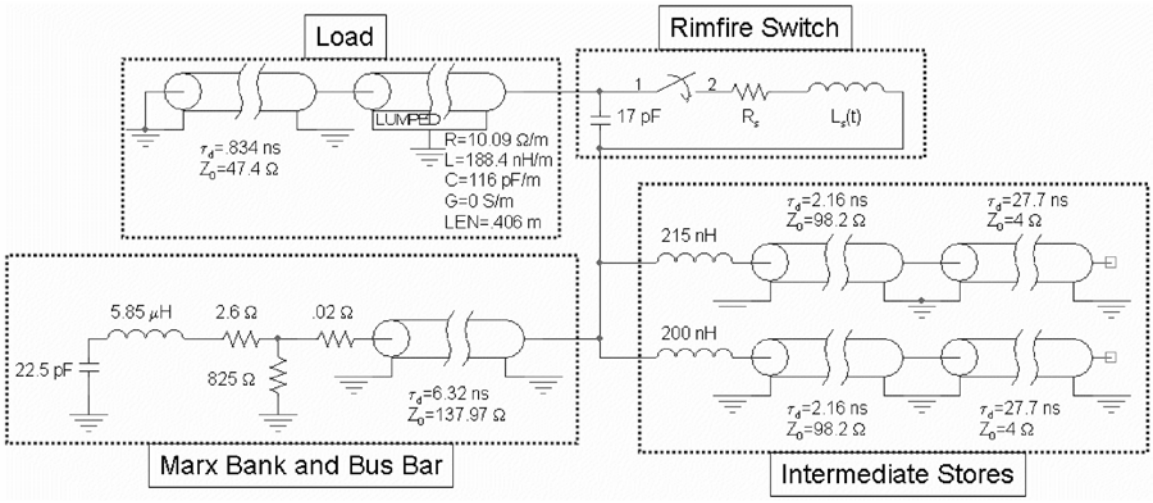

Figure 30: Revised system circuit model of MUTTS.

4.2 Diagnostics

In the MUTTS experiments, the load current measurement was made using T&M Research F-250-1 current viewing resistors (CVRs) placed in series with each of eight load resistors. All CVRs were monitored separately. The CVRs have a risetime of .45 ns, a Bandpass of 800 MHz, and a series resistance of .02 Ω. The voltage was monitored using two 44000:1 resistive voltage monitors. One monitor was placed on the Rimfire field shaper closest to the load, and the other

was placed on the field shaper closest to the intermediate store. A Cannon Powershot A75 was used as the open-shutter camera for viewing optical data. A Kodak ND 4.0 filter was used to attenuate the light into the aperture [2].

4.3 Metal Insert Dielectric Electrode Design

The original toroidal electrodes used in the Rimfire switch have two characteristics that need to be studied further. First, while multichanneling is prevalent in shots using toroidal electrodes, it is not consistent. For example, one cascade gap may have eight arcs, but the adjacent gap will only have one. Second, the inconsistency of arcing from gap-to-gap promotes azimuthal currents in the electrodes. This possibly contributes to an overall increased switch inductance [3].

To study the effects mentioned above, the Metal Insert Dielectric (MID) electrodes were utilized. Volkov studied similar electrodes that were modeled in section 3.3.2 [4]. The MID electrodes consist of a circular dielectric of high-density polyethylene and spherical 440C stainless steel balls. The steel balls were inserted symmetrically around the perimeter of a circle with the same diameter as the diameter of the toroidal electrodes. The dielectric plates were constructed such that the balls were easily removed and that the numbers of balls per plate were easily varied from one to twelve balls. It was desired for less than 5% variation in the 9.53 mm (3/8”) spark gap distances, so manufacturing tolerances were less than .5 mm (.02”). Gap spacing was controlled by machining a groove in the walls of the dielectric where the balls were to be inserted. The MID

electrodes fit easily into slots once occupied by toroidal electrodes in the Rimfire switch. A photograph of one dielectric plate for a MID electrode is shown in Figure 31. For all tests, only the inner diameter is utilized. In this thesis, the steel balls are referred to as ball electrodes and the dielectric disk containing ball electrodes is the MID electrode.

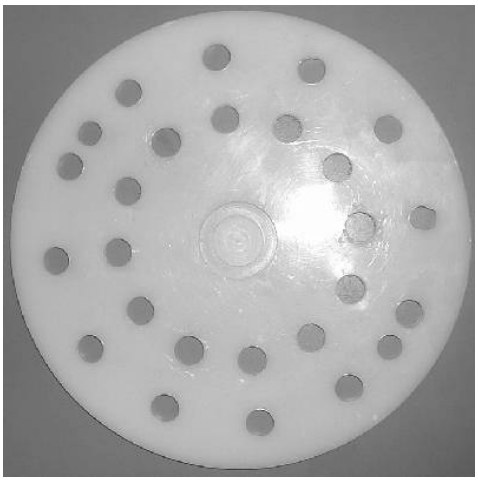

Figure 31: Dielectric plate for the MID electrode.

It was desired to have the breakdown characteristics in the cascade section remain relatively constant when comparing the toroidal electrodes to the MID electrodes. For this reason, the dimensions were chosen such that the field enhancement would be constant. The cascade electrodes were simulated in Maxwell and their FEF was found to be ~1.1. Ball diameter and gap spacing were then found to match this FEF.

4.4 Experiments

For all the tests, air was used as the gas in the switch. In addition, adjustment of gas pressure was the only method of controlling switch breakdown voltage. Tests were conducted for both a +/-30 kV charge and +/-40 kV Marx charge. This corresponds to a maximum intermediate store voltage of 960 kV and 1.28 MV respectively. Voltage on each side of the switch and load current was measured.

4.4.1 Original Electrodes

Initial shots were taken on MUTTS to characterize the machine. Several shots were taken using the original toroidal electrodes at the same voltages of this study [2]. For comparison purposes, these results are shown here. Shots 28-33 were for a 30 kV Marx charge and shots 34-37 were for a 40 kV Marx charge. Figure 32 shows the optical data for the shots and Table 11 and Table 12 show a summary of the electrical data. At the top of each photograph, the trigger section arc is visible. Below that are the arcs between the cascade toroidal electrodes. As shown, multichanneling occurred in the cascade section, but was inconsistent.

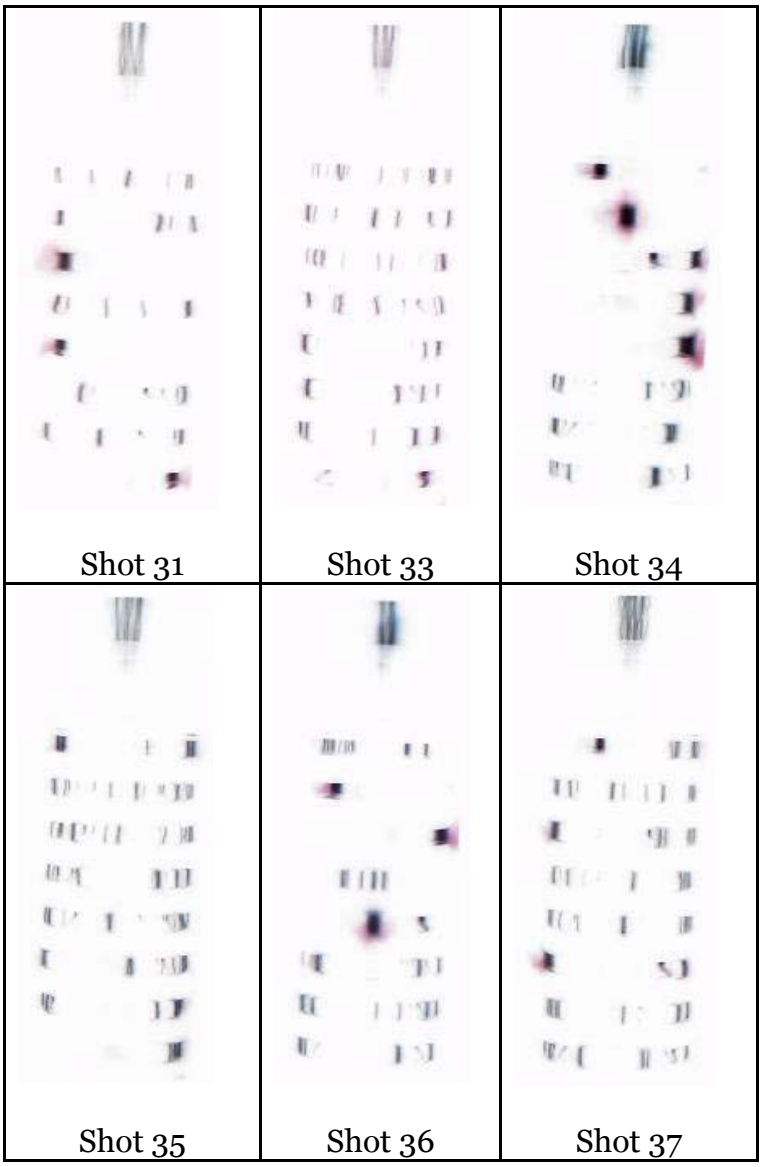

Figure 32: Open-shutter optical data for original toroidal electrode tests.

Table 11: Electrical data summary for original toroidal electrode tests and a 30 kV Marx charge. Risetimes and falltimes are 10-90%.

Shot	Load Current Risetime (ns)	Peak Load Current (kA)	Intermediate Store Falltime (ns)	Intermediate Store Max (kV)
28	101	87.6	228	840
30	103	92.4	264	860
31	112	96	247	871
32	101	96.5	243	909
33	103	96.7	245	876
Avg.	*104*	*93.8*	*245.4*	*871.2*

Table 12: Electrical data summary for original toroidal electrode tests and a 40 kV Marx charge. Risetimes and falltimes are 10-90%.

Shot	Load Current Risetime (ns)	Peak Load Current (kA)	Intermediate Store Falltime (ns)	Intermediate Store Max (kV)
34	102	129.4	232	1194
35	99	131.3	249	1189
36	107	130.6	235	1200
37	102	131	229	1196
Avg.	*102.5*	*130.6*	*236.3*	*1194.8*

4.4.2 MID Electrode Tests

For the first set of tests using the MID electrodes, three ball electrodes were inserted into the each of the nine MID electrodes. A top view of a single MID electrode is shown in Figure 33 and a side view of one MID electrode is shown in Figure 34. A photograph of the MID electrodes in the switch is shown in Figure 35.

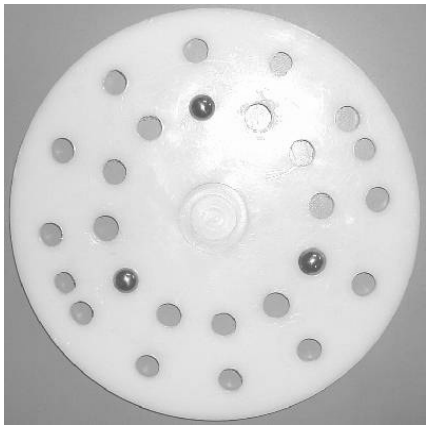

Figure 33: Top view of a 3 ball electrode MID electrode.

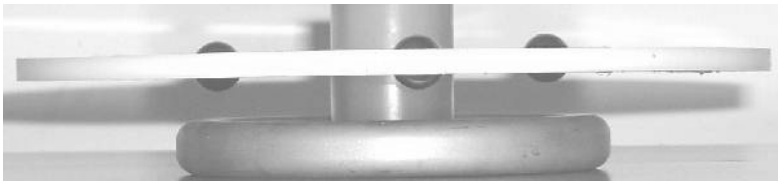

Figure 34: Side view of 3 ball electrode MID electrode with a toroidal electrode.

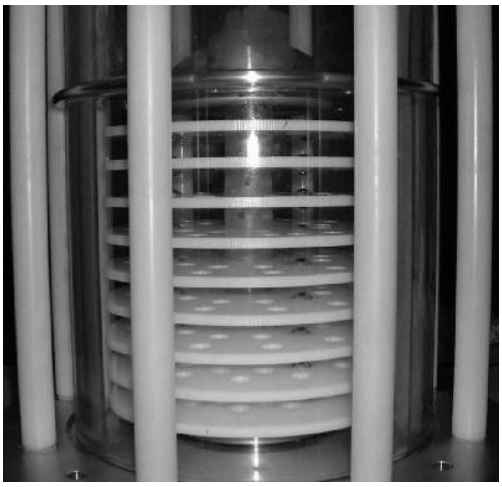

Figure 35: Side view of the MUTTS Rimfire switch with MID electrodes installed.

For these tests, it was expected that the switch would multichannel in three cascade section-length arcs. Five total shots were taken. Shots 57-59 were

for a 30 kV Marx charge and shots 60-62 were for a 40 kV Marx charge. Optical data is shown in Figure 36 and a summary of electrical data is shown in Table 13 and Table 14. As shown in Figure 36, in all but one case, a single, cascade section-length arc occurred. For shot 60, two arcs occurred. These results were unexpected and did not agree with the results from Volkov that stated achievement of multichanneling on every shot. However, the Volkov experiments had a shorted load and were laser triggered which may account for the discrepancy [4].

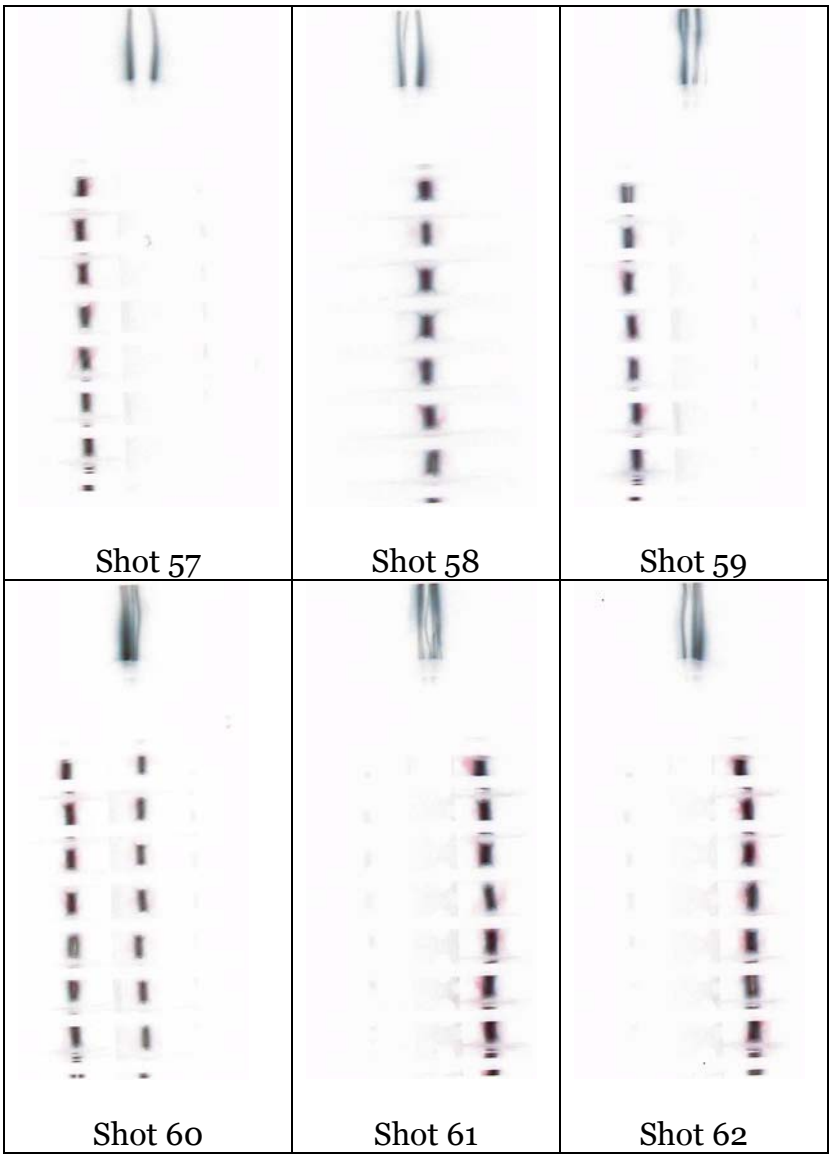

Figure 36: Open-shutter optical data for MID electrode ball-only tests.

Table 13: Electrical data summary for MID electrode ball only tests for a 30 kV Marx charge. Risetimes and falltimes are 10-90%.

Shot	Load Current Risetime (ns)	Peak Load Current (kA)	Intermediate Store Falltime (ns)	Intermediate Store Max (kV)
57	NO DATA			
58	117	86.6	255	892
59	123	85.2	284	806
Avg.	*120*	*85.9*	*269.5*	*849*

Table 14: Electrical data summary for MID electrode ball only tests for a 40 kV Marx charge. Risetimes and falltimes are 10-90%.

Shot	Load Current Risetime (ns)	Peak Load Current (kA)	Intermediate Store Falltime (ns)	Intermediate Store Max (kV)
60	112	125.8	255	1226
61	118	122.2	258	1199
62	116	120.7	258	1188
Avg.	*115.3*	*122.9*	*257.0*	*1204.3*

4.4.3 Alternating Electrodes

Due to unexpected results with the all-MID electrode cascade section, it was decided to try alternating toroidal electrodes with MID electrodes in order to increase the capacitance between sections. Between each MID electrode, a toroidal electrode was installed as in Figure 37. As described in chapter 3, the cascade section arcs form a high-Q resonant LC circuit which results in a high frequency oscillation that inhibits the arcs from extinguishing. The all-MID electrode cascade section has dramatically reduced electrode capacitance, but adding toroidal electrodes increases this capacitance. This arrangement of electrodes is shown in Figure 37.

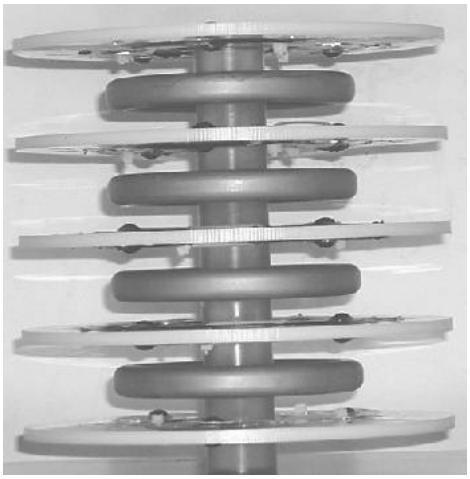

Figure 37: MID electrodes alternating with toroidal electrodes.

First, a three ball electrode arrangement was utilized for the MID electrodes. Shots 70-72, 77-80, and 86-88 were for a 30 kV Marx charge. Shots 73-75, 81-85, and 89-91 were for a 40 kV Marx charge. Optical data for a 30 kV Marx charge is shown in Figure 38 and for a 40 kV Marx charge in Figure 39. A summary of electrical data is shown in Table 15 and Table 16.

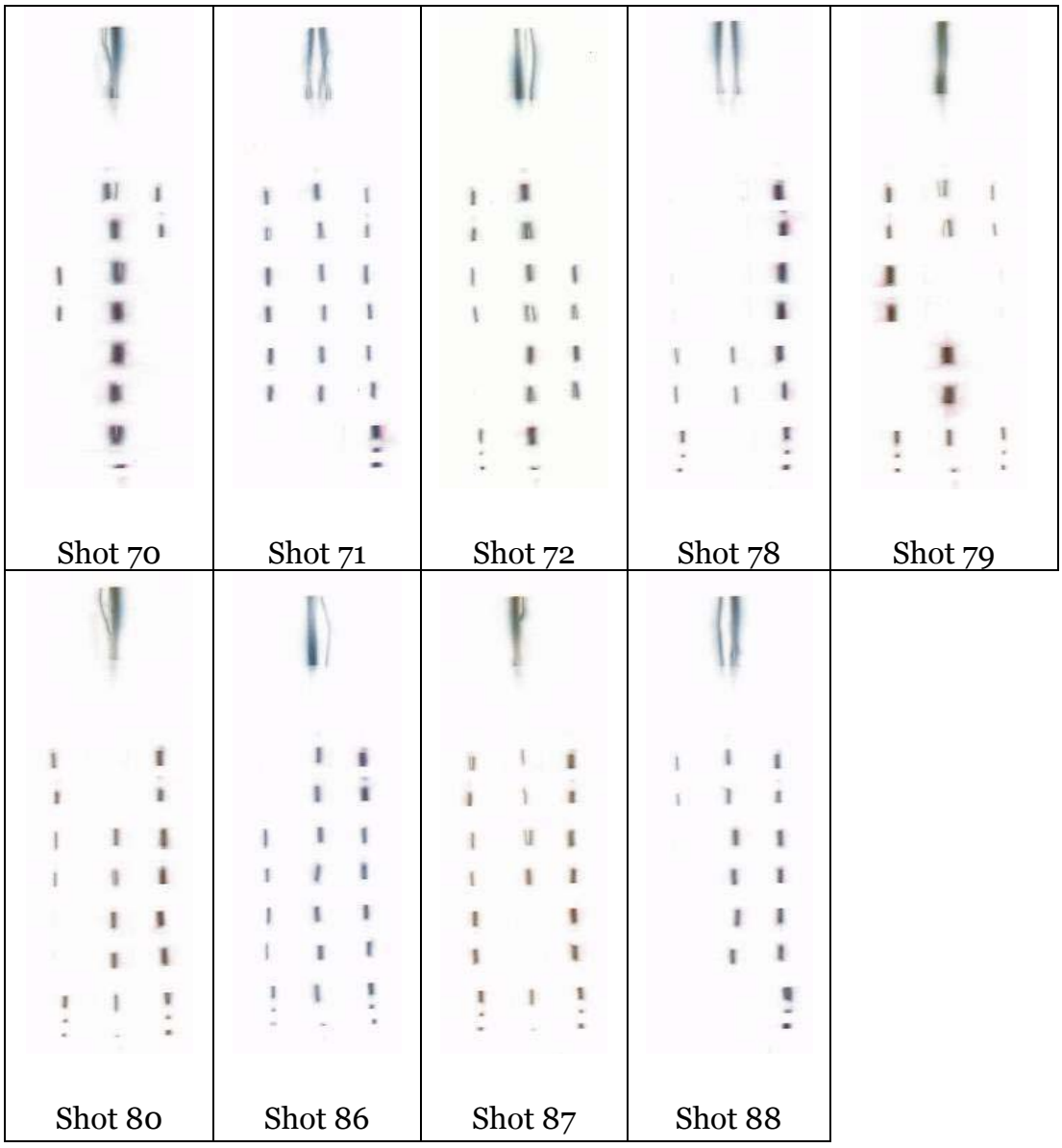

Figure 38: Open-shutter optical data for three ball MID electrodes alternating with toroidal electrodes with a 30 kV Marx charge.

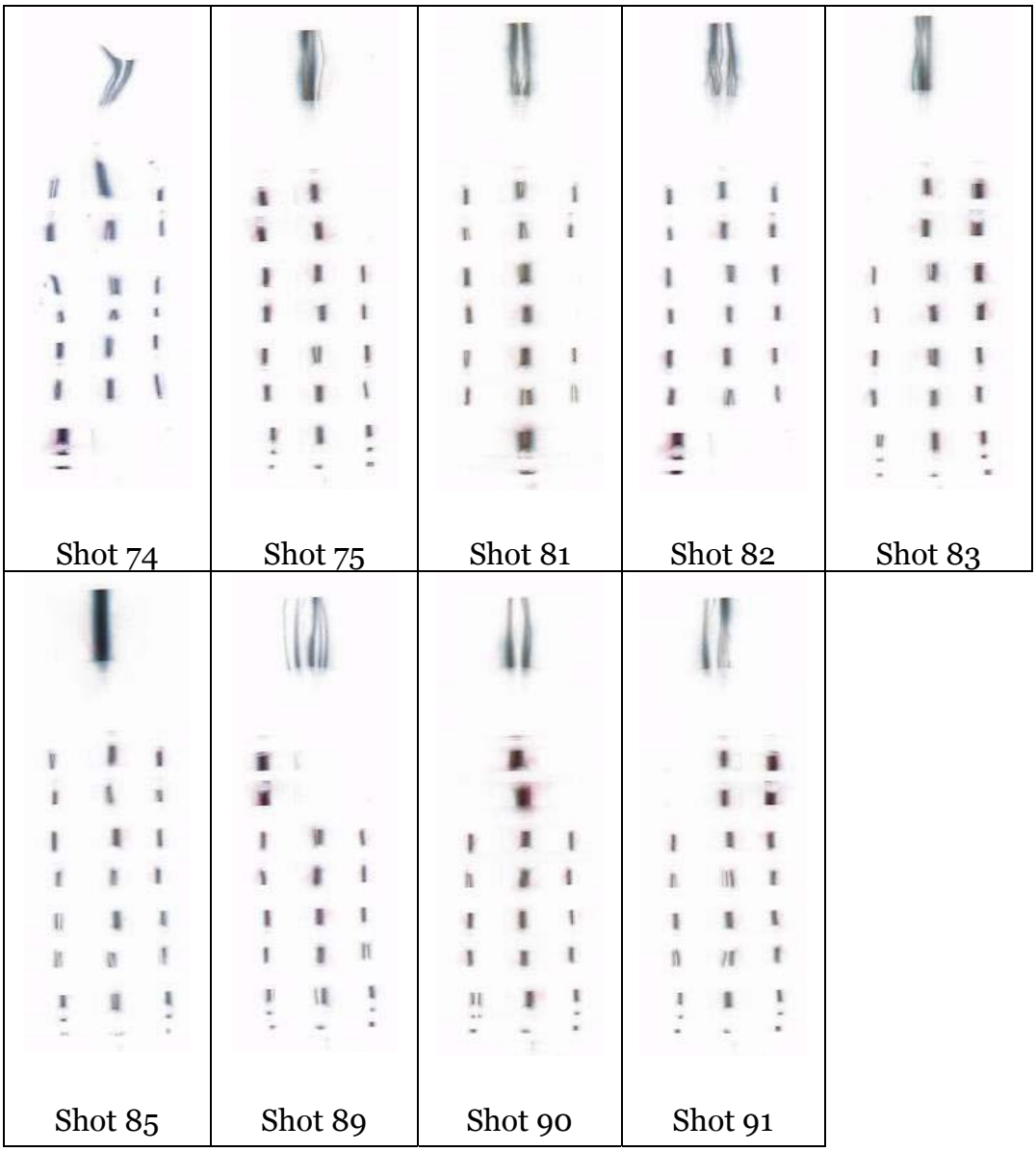

Figure 39: Open-shutter optical data for three ball MID electrodes alternating with toroidal electrodes with a 40 kV Marx charge.

Table 15: Electrical data summary for three ball MID electrodes alternating with toroidal electrode for a 30 kV Marx charge. Risetimes and falltimes are 10-90%.

Shot	Load Current Risetime (ns)	Peak Load Current (kA)	Intermediate Store Falltime (ns)	Intermediate Store Max (kV)
70	104	95.5	230	1043
71	113	93.8	258	905
72	109	95.5	255	926
77	112	93.6	n/a	n/a
78	110	92.2	252	942
79	112	94.8	252	941
80	110	96.2	251	975
86	98.4	96.9	225	1037
87	98.8	96	224	1054
88	93.6	78.2	201	1057
Avg.	*107.5*	*93.3*	*238.7*	*986.7*

Table 16: Electrical data summary for three ball MID electrodes alternating with toroidal electrode for a 40 kV Marx charge. Risetimes and falltimes are 10-90%.

Shot	Load Current Risetime (ns)	Peak Load Current (kA)	Intermediate Store Falltime (ns)	Intermediate Store Max (kV)
73	112	125.8	260	1193
74	107	128.2	256	1249
75	108.8	127.9	256	1247
81	96.8	118.3	221	1416
82	112	127.9	259	1186
83	104	130.6	252	1304
85	99.8	130.1	225	1364
89	94	120	202	1418
90	102	129.6	250	1290
91	99.6	131.3	228	1325
Avg.	*103.6*	*127.0*	*240.9*	*1244.8*

By inspection, this version of the cascade section had much better multichanneling properties compared to the MID electrode only cascade section. While still not ideal in every shot, a much higher percentage of visible gaps broke down. It was decided to continue to vary the number of ball electrodes in the MID electrodes. First, shots with two balls per MID electrode were conducted. Shots

94-100 were for a 30 kV Marx charge. Shots 101-108 were for a 40 kV Marx charge. Optical data for a 30 kV Marx charge is shown in Figure 40 and for a 40 kV Marx charge in Figure 41. A summary of electrical data is shown in Table 17 and Table 18.

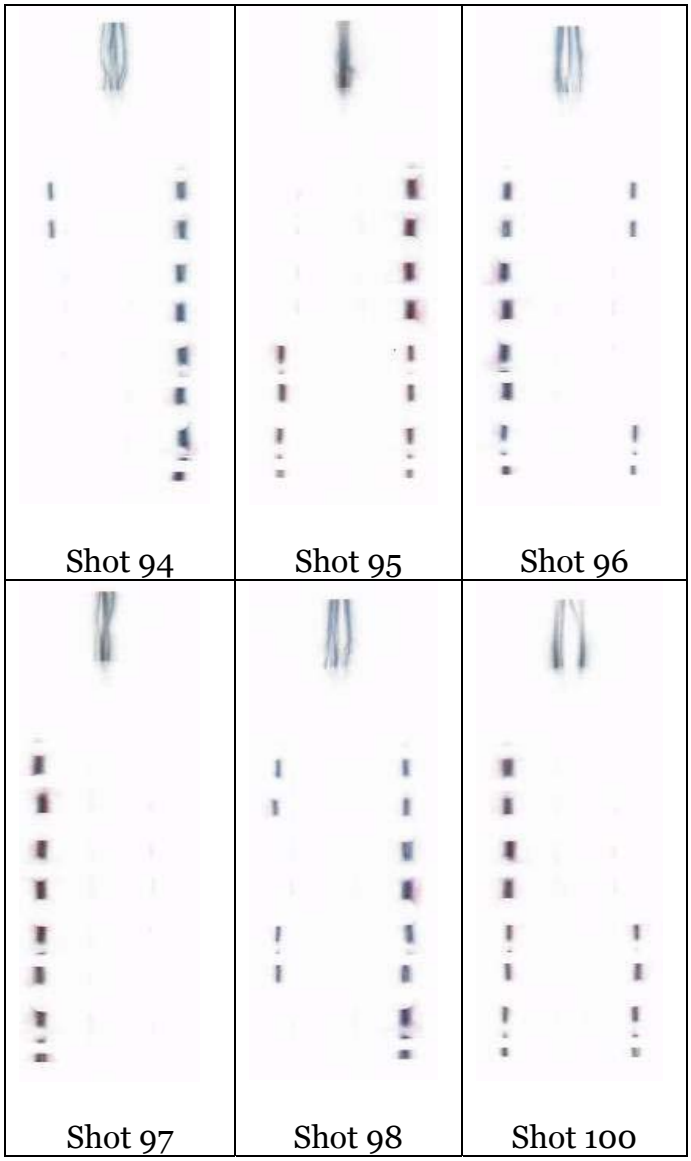

Figure 40: Open-shutter optical data for two ball MID electrodes alternating with toroidal electrodes with a 30 kV Marx charge.

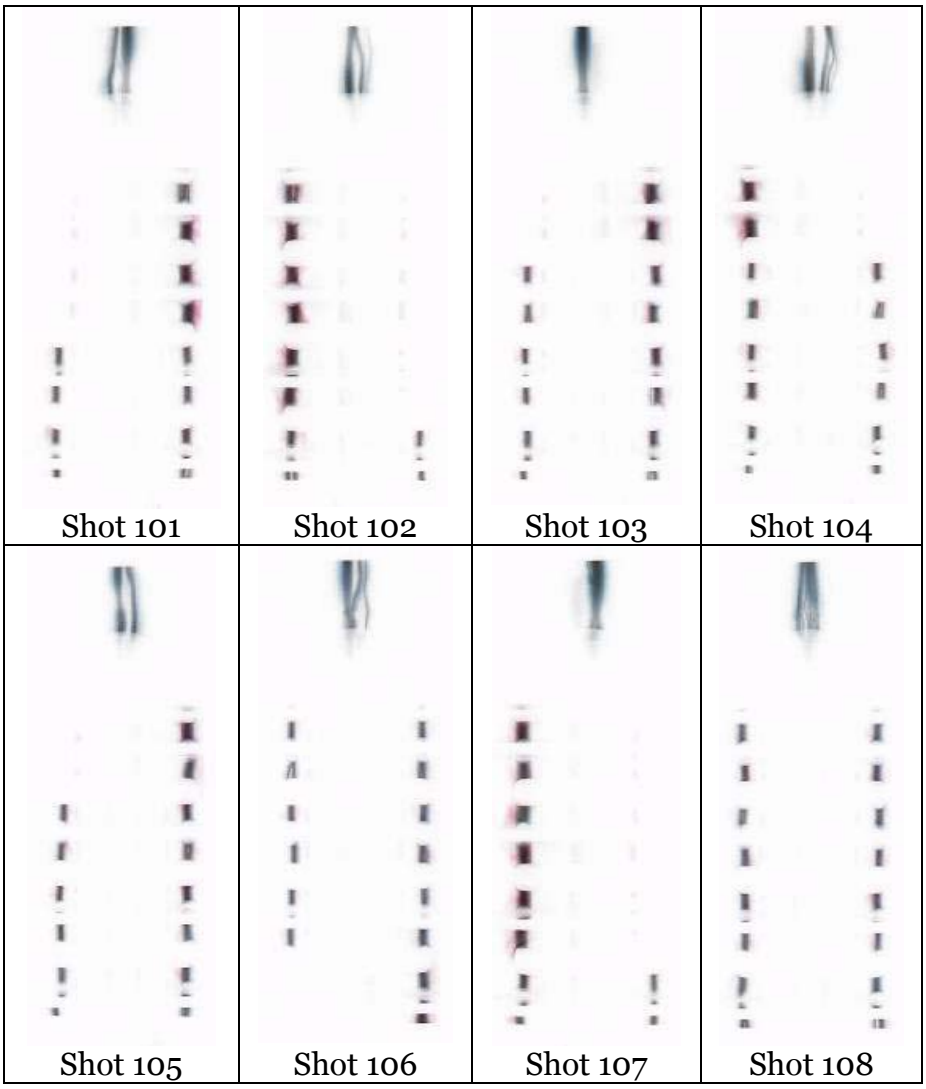

Figure 41: Open-shutter optical data for two ball MID electrodes alternating with toroidal electrodes with a 40 kV Marx charge.

Table 17: Electrical data summary for two ball MID electrodes alternating with toroidal electrode for a 30 kV Marx charge. Risetimes and falltimes are 10-90%.

Shot	Load Current Risetime (ns)	Peak Load Current (kA)	Intermediate Store Falltime (ns)	Intermediate Store Max (kV)
95	106.4	94.8	253	926.7
96	117.2	92.4	275	864.1
97	116.4	93.6	253	935.4
98	108.4	94.3	253	925
100	106.8	95.5	248	952
Avg.	*111*	*94.1*	*256.4*	*920.6*

Table 18: Electrical data summary for two ball MID electrodes alternating with toroidal electrode for a 40 kV Marx charge. Risetimes and falltimes are 10-90%.

Shot	Load Current Risetime (ns)	Peak Load Current (kA)	Intermediate Store Falltime (ns)	Intermediate Store Max (kV)
101	100.8	127.7	245	1321
102	117	123.3	274	1129
103	98.8	125	221	1421
104	102	129	250	1289
105	106.8	126	255	1200
106	93.6	108.5	199	1376
107	104	127	250	1297
108	113	126	257	1175
Avg.	*104.5*	*124.1*	*243.9*	*1276.0*

Next, shots with six balls per MID electrode were conducted. Shots 126-133 were for a 30 kV Marx charge. Shots 134-144 were for a 40 kV Marx charge. Optical data for a 30 kV Marx charge is shown in Figure 42 and for a 40 kV Marx charge in Figure 43. One row of arcs is not visible due to a dielectric rod obstructing the view. A summary of electrical data is shown in Table 19 and Table 20.

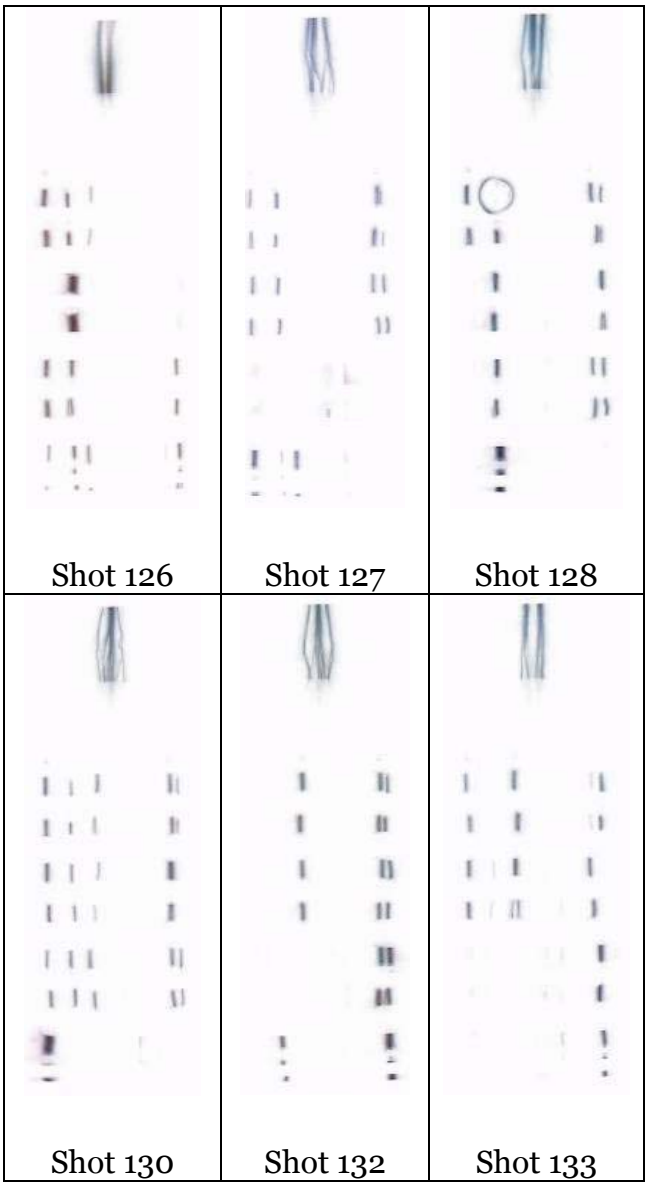

Figure 42: Open-shutter optical data for six ball MID electrodes alternating with toroidal electrodes with a 30 kV Marx charge.

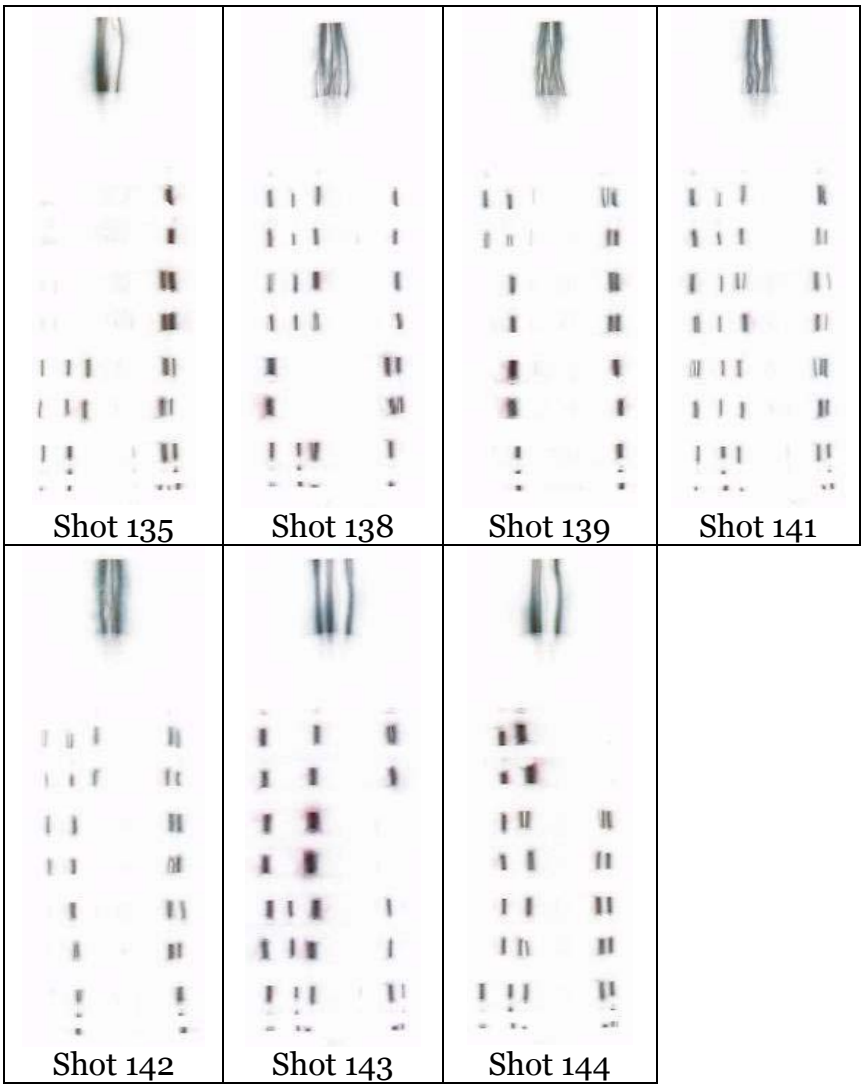

Figure 43: Open-shutter optical data for six ball MID electrodes alternating with toroidal electrodes with a 40 kV Marx charge.

Table 19: Electrical data summary for six ball MID electrodes alternating with toroidal electrode for a 30 kV Marx charge. Risetimes and falltimes are 10-90%.

Shot	Load Current Risetime (ns)	Peak Load Current (kA)	Intermediate Store Falltime (ns)	Intermediate Store Max (kV)
126	112	95.3	257	898
127	108	94.6	252	931
128	112.4	91.9	259	873
129	112	96.8	255	847
130	107	94.6	250	943
131	107.2	91.4	253	905
132	106.8	90.9	253	881
133	106.8	93.6	253	899
Avg.	*109.0*	*92.4*	*254.0*	*904.3*

Table 20: Electrical data summary for six ball MID electrodes alternating with toroidal electrode for a 40 kV Marx charge. Risetimes and falltimes are 10-90%.

Shot	Load Current Risetime (ns)	Peak Load Current (kA)	Intermediate Store Falltime (ns)	Intermediate Store Max (kV)
134	102.8	127.4	252	1276
135	100.8	129.1	252	1253
136	106.8	125.04	255	1166
137	114.8	123.6	280	1096
138	100	130.08	249	1287
139	103.2	126.5	254	1214
141	106	128	255	1185
142	100	132.2	251	1285
143	106.4	133.2	256	1241
144	104	130.6	255	1244
Avg.	*104.5*	*128.6*	*255.9*	*1225*

4.4.4 Electrically Connected Ball Electrodes

To further investigate the parameters that affect the multichanneling of the Rimfire switch, new MID electrodes were constructed. These MID electrodes had ball electrodes that were electrically connected by aluminum .00754 inch flashing. The electrodes would be high capacitance, but also have an electrical

connection between the electrodes. The first test utilizing these electrodes was conducted under the assumption that for prevalent multichanneling, there is a requirement for an electrical connection between ball electrodes. One electrically connected MID electrode (ECMID) is shown in Figure 44.

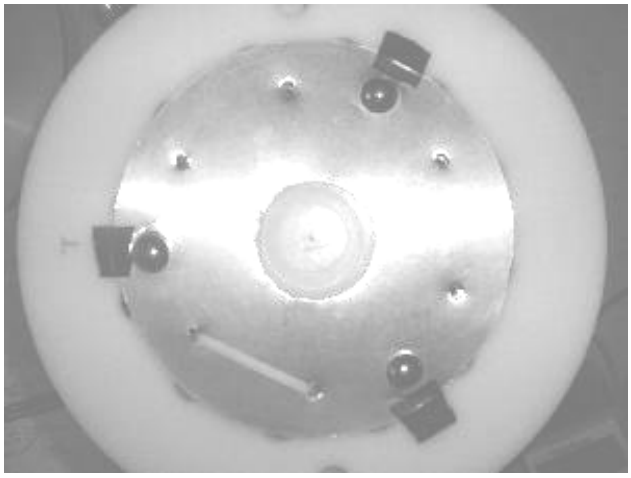

Figure 44: Photograph of one ECMID electrode.

The tests were conducted with the same parameters as previously mentioned. Shots 145-152 were for a 30 kV Marx charge. Shots 153-158 were for a 40 kV Marx charge. Optical data for a 30 kV Marx charge is shown in Figure 45 and for a 40 kV Marx charge in Figure 46. A summary of electrical data is shown in Table 21 and Table 22.

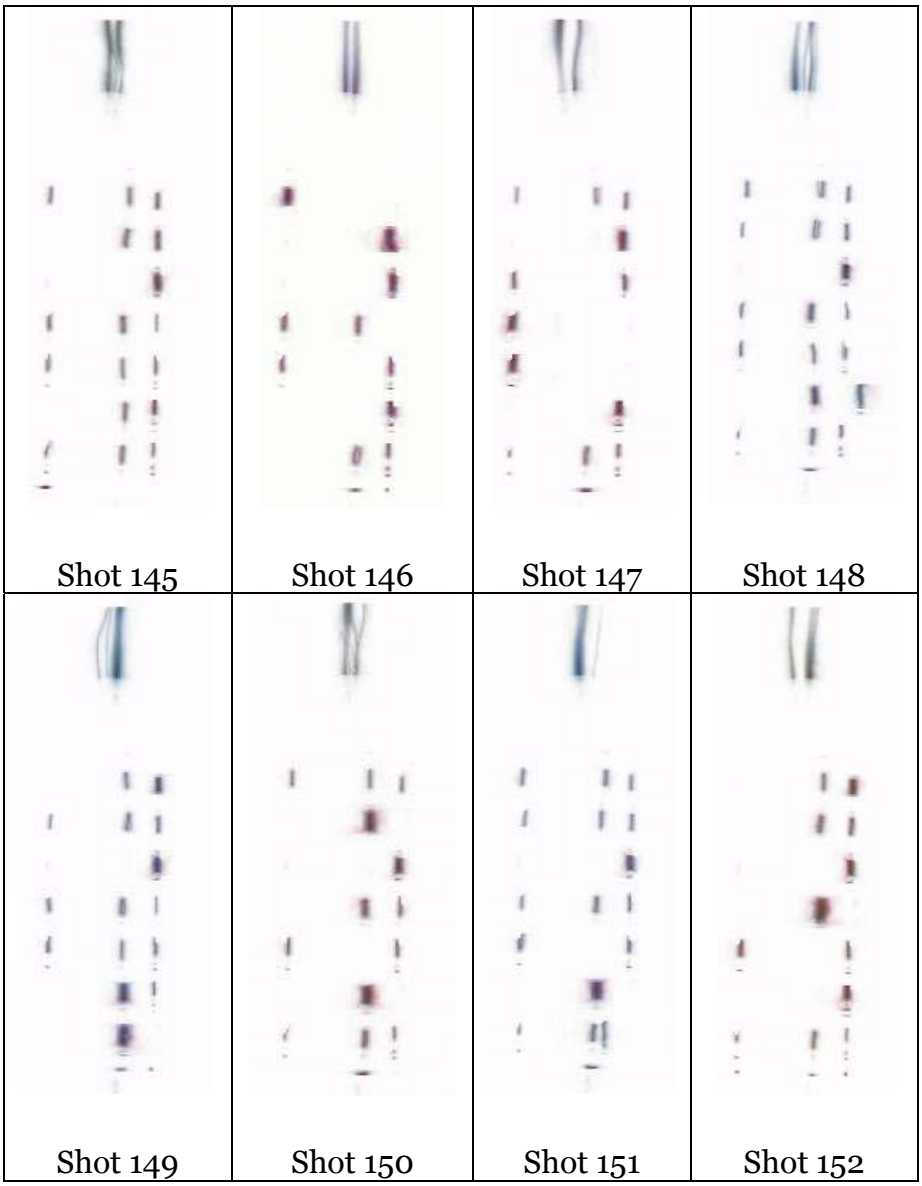

Figure 45: Open-shutter optical data for ECMID electrodes with a 30 kV Marx charge.

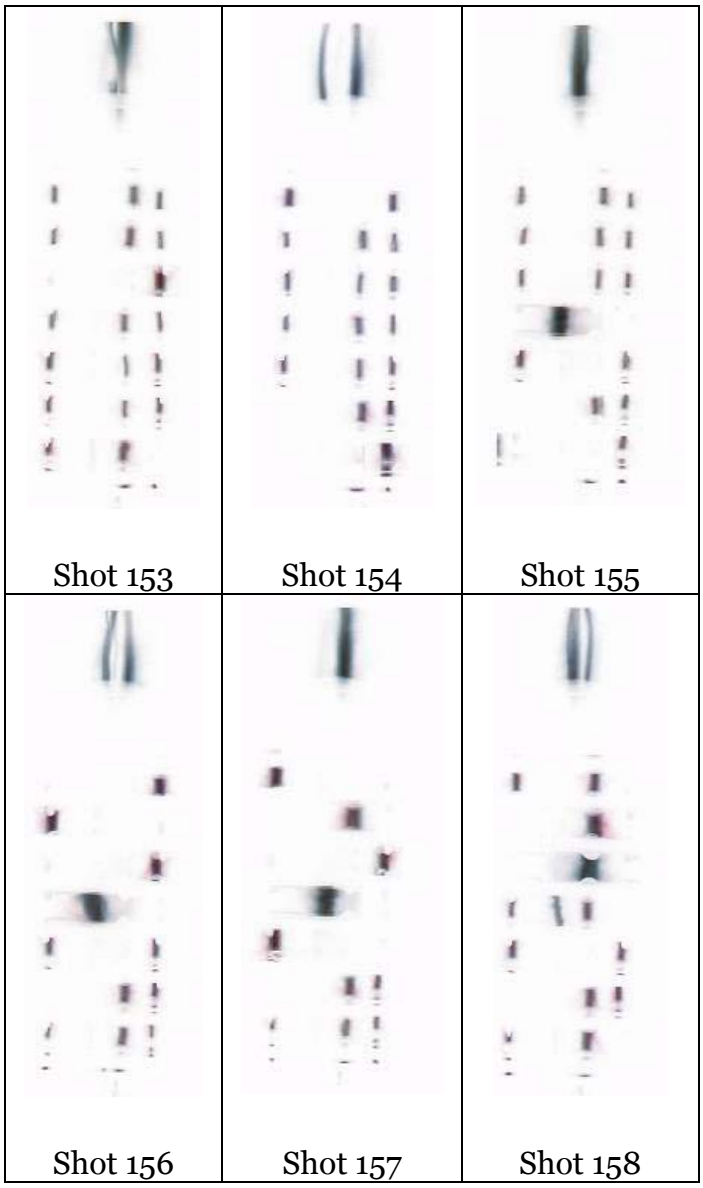

Figure 46: Open-shutter optical data for ECMID electrodes with a 40 kV Marx charge.

Table 21: Electrical data summary for ECMID electrodes for a 30 kV Marx charge. Risetimes and falltimes are 10-90%.

Shot	Load Current Risetime (ns)	Peak Load Current (kA)	Intermediate Store Falltime (ns)	Intermediate Store Max (kV)
145	118	89.3	283	830
146	119	89	281	802
147	119	91.2	251	836
148	119	90	242	782
149	116	90.9	278	827
150	114	92.2	271	859
151	112	91.9	249	859
152	112	95.7	256	897
Avg.	*116.1*	*91.3*	*263.9*	*836.6*

Table 22: Electrical data summary for ECMID electrodes for a 40 kV Marx charge. Risetimes and falltimes are 10-90%.

Shot	Load Current Risetime (ns)	Peak Load Current (kA)	Intermediate Store Falltime (ns)	Intermediate Store Max (kV)
153	116	119	280	1046
154	115	123	278	1107
155	116	123	278	1123
156	118	117	280	1027
157	125.2	113.3	258	939
158	116	120	278	1046
Avg.	*117.7*	*119.2*	*275.3*	*1048.0*

As shown in shots 155-158 in Figure 46, in the forth electrode down from the trigger section, there was an anomalous breakdown between the plates themselves. The breakdown is attributed to rough edges on the plates that caused an increase in the FEF. This appears to have had a negative effect on multichanneling in the cascade section. In addition, after shot 155, this area broke down every time. For this reason, tests with these electrodes were terminated.

4.4.5 Electrically Isolated, High Capacitance Ball Electrodes

The second multichanneling second test utilized isolated ball electrodes with plates attached to each individual ball. The same electrodes were used from the previous test, but with the plates segmented between each ball electrode on the MID electrode. This electrically isolated, high capacitance MID electrode (EIHCMID) is shown in Figure 47.

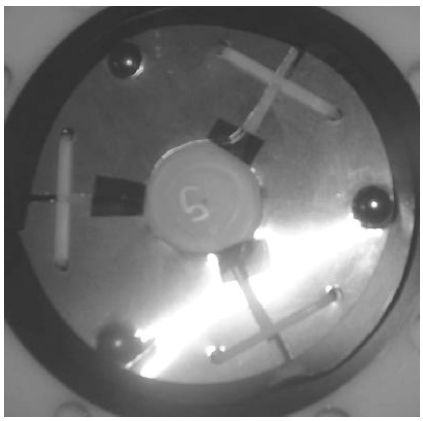

Figure 47: Photograph of one EIHCMID electrode.

After using these electrodes, it was apparent that they were not breaking down as intended. If the ball electrodes were electrically isolated, it would be impossible for there not to be one (or more) continuous arcs down the entire cascade section. As shown by shot 161 in Figure 48, the arcs were not continuous for the length of the cascade section. This implies that there was still a conducting path between the ball electrodes on an MID electrode.

After the electrodes were removed and inspected, it was confirmed that there was arcing between the ball electrodes on the MID electrodes. Figure 49 shows one such breakdown. The dark deposit on the dielectric shows where one

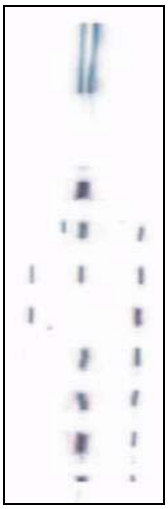

Figure 48: Open-shutter optical data for shot 161 of the EIHCMID electrodes.

arc discharged between plates. For this reason, the gap between plates on the electrode was widened to discourage breakdown. However, the capacitance from electrode to electrode would decrease. The redesigned electrode is shown in Figure 50.

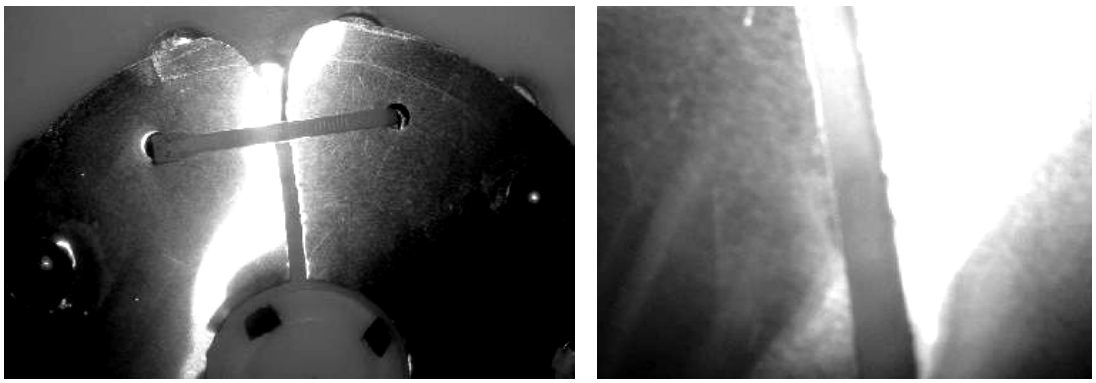

Figure 49: Breakdown between EIHCMID electrodes. Left: overview. Right: close-up.

The redesigned electrodes were installed in the switch and tested. Experimental time constraints only allowed one Marx voltage to be tested, so

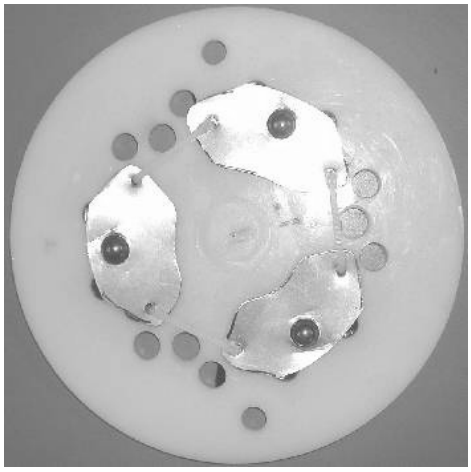

Figure 50: Redesigned EIHCMID electrode.

40 kV was chosen. Shots 162-167 were with a 40 kV Marx charge. Optical data for a 40 kV Marx charge is in Figure 51. A summary of electrical data is shown in Table 23.

All shots appeared to break down as expected except for shot 163. The right set of ball electrodes broke down in the top three gaps. However, there is one continuous arc on the left side of the cascade section. All gaps had exactly one continuous arc except shot 167, which had two. The results from these tests do not appear to vary significantly from the all-MID electrode tests in section 4.4.2.

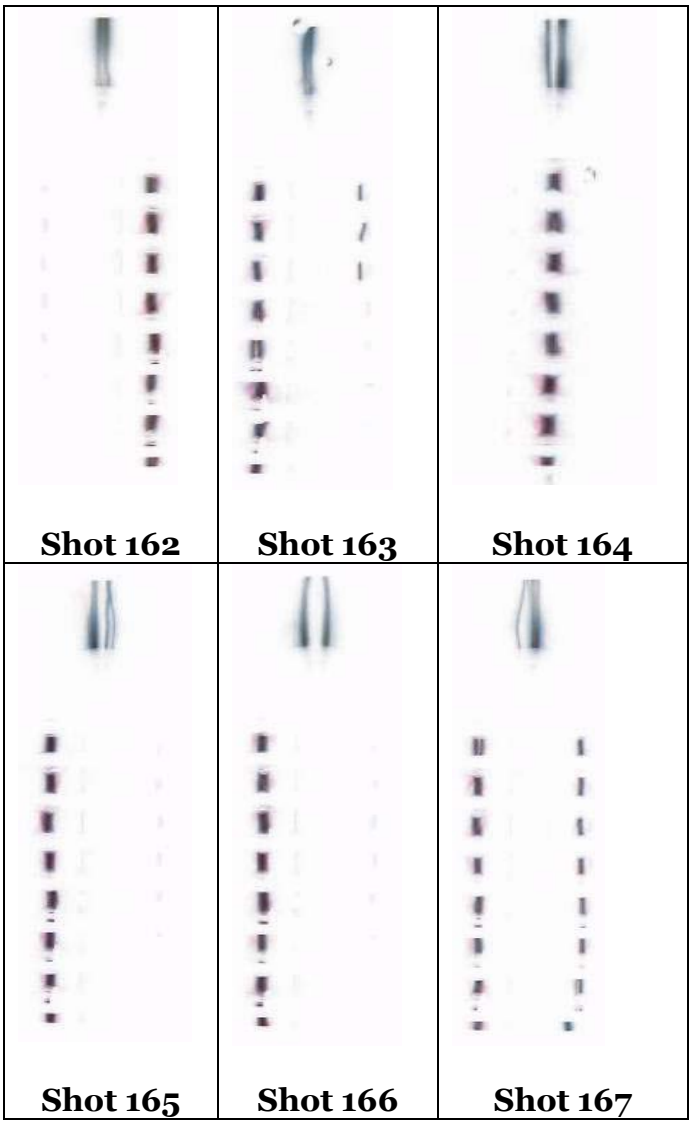

Figure 51: Open-shutter optical data for EIHCMID electrodes. 40 kV Marx charge.

Table 23: Electrical data summary for redesigned EIHCMID electrodes. All shots were for 40 kV Marx charge. Risetimes and falltimes are 10-90%.

Shot	Load Current Risetime (ns)	Peak Load Current (kA)	Intermediate Store Falltime (ns)	Intermediate Store Max (kV)
162	116	119	275	1128
163	125	111	261	945
164	125	114	302	979
165	129	111	255	913
166	131	110	261	887
167	114	125	263	1128
Avg.	*123.3*	*115*	*269.5*	*996.7*

4.5 Results

This section presents the results for the experiments described in the previous section. In all, there were five different cascade section topologies in the tests. One setup was the all-MID electrode cascade section that predominantly had only one long arc. In addition, two, three, and six ball electrode versions of the alternating arrangement were tested. The one arc, EIHCMID electrode results were included with the all-MID tests. Lastly, the original toroidal electrodes were tested. In this section, these tests are referred to as the one arc, two ball, three ball, six ball, and original electrode shot setups. Electrical and optical data from the ECMID electrode tests are not included in the analysis.

4.5.1 Multichanneling Properties

The first multichanneling parameter of interest is the effect of changing the number of ball electrodes per MID electrode on the number of arcs in the cascade section. As stated earlier, the bottom two gaps in the cascade section

were completely concealed in the photographs. However, it is possible to count the number of total visible arcs in the cascade section for a given shot setup. Figure 52 shows averages for seven shots at each data point. As expected, as the number of ball electrodes increased, the total number of cascade arcs increased.

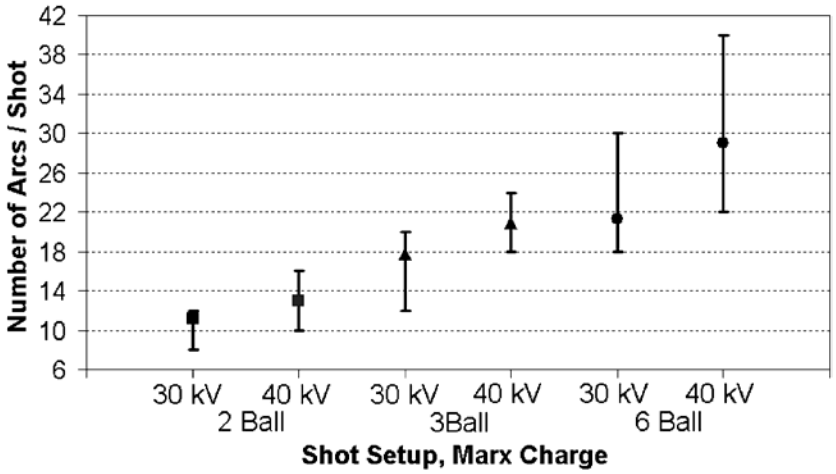

Figure 52: Total number of visible arcs in the cascade section for a given number of ball electrodes in the MID electrodes. Data points are the mean of seven shots and error bars are the range of data.

Another observation of Figure 52 is that the 40 kV Marx charge shots had a higher number of arcs than the 30 kV Marx charge shots. Therefore, it was of interest to study the effect of switch breakdown voltage on the multichanneling of the cascade section. To do this, the number of possible arc locations was determined by multiplying the number of ball electrodes per MID electrode by the number of gaps between electrodes. Then, the number of visible arcs was counted. The number of observed arcs was then divided by the number of possible arc locations in the cascade section. In Figure 53, this value, the arc efficiency, is shown versus the magnitude of the voltage of the intermediate store

at the time of switch breakdown. Two, three, and six ball electrode data is shown for both 30 and 40 kV Marx charges.

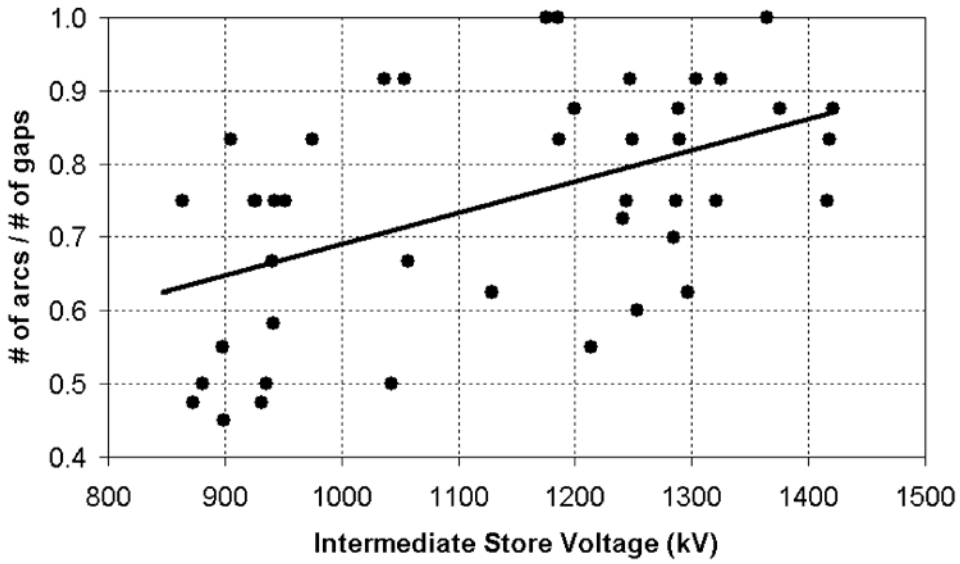

Figure 53: Cascade section arc efficiency with respect to switch voltage at time of breakdown. R^2=.25.

Two statistical methods were utilized to analyze the data. First, the coefficient of determination, R^2, was calculated. An R^2 value close to 1 means that most of the data variation can be explained by a linear relationship between the independent and dependent variables. A value close to 0 means none of the variation can be described. Secondly, a p-value test determines if there is a statistically significant (α=.01) dependence of the dependent variable on the independent variable [5]. With these techniques, it was found that the arc efficiency had a statistically significant dependence on the breakdown voltage, however only 25% of the variation was described by the breakdown voltage.

4.5.2 Electrical Properties

All of the shots taken in these experiments were untriggered. This condition has two effects on data. First, switch breakdown voltage for a given Marx charge was not consistent. The consequence of this condition is that comparisons of electrical values must take into account dependence on the voltage at which the switch breaks down. The second effect of using an untriggered switch is that the cascade section may self-break before the trigger section breaks down. Multichanneling in the cascade section may be affected by this.

There was a +/-20% spread in the switch breakdown voltage for a given Marx charge in the MUTTS experiments. To easily compare all data, for each shot the switch breakdown voltage was divided by the maximum intermediate store voltage if the switch were not to break down. Figure 54 shows load current risetime (10-90%) versus the breakdown percentage of intermediate store maximum voltage. All of the risetime data sets have over 65% of the variance described by the breakdown voltage of the switch. In typical pulsed power applications, load current risetime can be analyzed to determine inductance. In these experiments, load current risetime may be dependent on switch inductance, but there is also a strong dependence on breakdown voltage. Therefore, a method of switch inductance measurement independent of switch breakdown voltage must be found.

It is noted that in Figure 54 the linear fit for the 3 ball electrode data is above the 2 ball electrode data. This implies that the 3 ball electrode data has a

lower load current risetime. However, the fits are so close, that the difference is not statistically distinguishable.

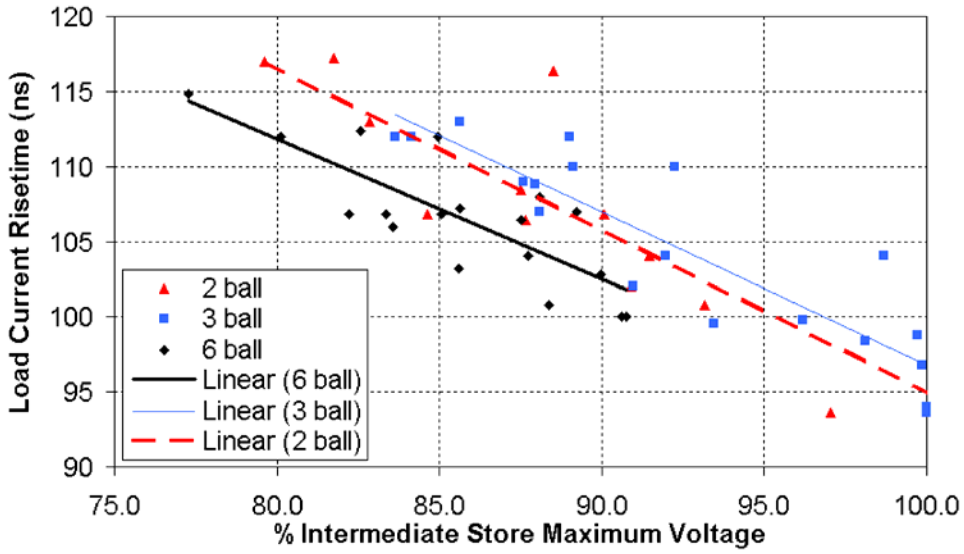

Figure 54: Dependence of load current risetime on percentage intermediate store maximum voltage at switch breakdown.

One method to find the switch inductance is to use a curve fitting technique utilizing the system circuit model of Figure 30. If the system circuit is kept the same for every shot, the only changes in the output waveforms must be based on the varying switch parameters (inductance, resistance, and breakdown voltage). Since the Marx charge is known for each shot, switch breakdown voltage for a given shot can be found from the peak voltage on the intermediate store.

Two switch parameters need to be resolved: resistance and inductance. However, each of these quantities may also have a dependence on time. Additionally, Martin suggests that the switch resistance has a dependence on the arc current [6]. Difficulty arises with matching experimental waveforms when

waveform parameters (falltime, overshoot, frequency, etc.) are not exclusively dependent on either inductance or resistance. For example, switch inductance A and resistance B may provide a good fit to experimental data, but inductance C and resistance D may provide an equally good fit. In other words, where there are two variables in the curve fit, there may be more than one solution. An exhaustive study using many shots of the same switch may be able to resolve this issue, but when comparing many different switch versions, one variable must be held constant.

When the Rimfire switch is used in large accelerators at Sandia, it connects two transmission lines. After the switch closes, the first transmission line charges the second transmission line. Then, the second transmission line is discharged through a second switch into a load. Because the second transmission line is charged during the rising edge of the pulse, the main switch attribute of interest is risetime. Traces from a typical shot on MUTTS are shown in Figure 55. The risetime (10-90%) of the load current is approximately 100 ns. The peak load current occurs at ~200 ns after the intermediate store voltage begins to fall. Therefore, the focus of the study is from switch closing until around 200 ns after breakdown.

There are two components that affect the impedance of the switch: inductance and resistance. The entire load section (the Rimfire switch plus the resistive load) is modeled as shown in Figure 56. The component values for the dummy load are known. Approximate values are known for the circuit parameters of the MUTTS Rimfire switch. Adjustment of these parameters in

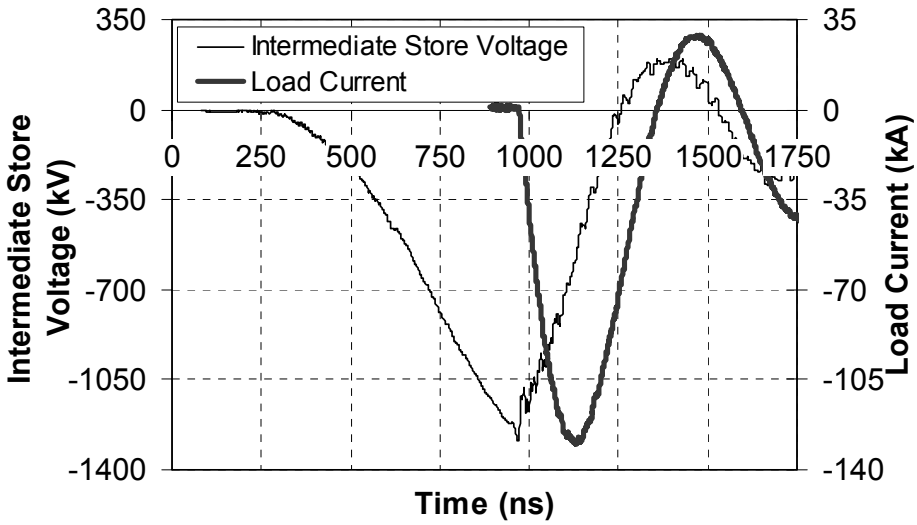

Figure 55: Intermediate store voltage and load current for typical MUTTS shot. Switch closes at ~970 ns.

circuit simulations shows that the dominate components of the load impedance are the inductance of the switch and the resistance of the dummy load.

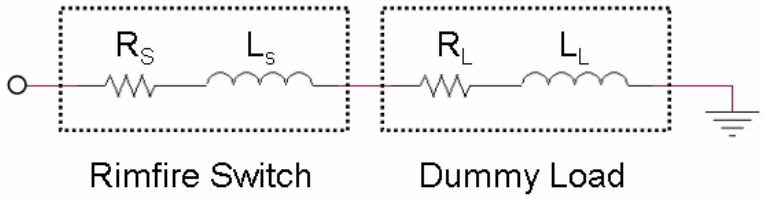

Figure 56: Components of MUTTS load (Rimfire switch plus dummy load).

It is assumed that changing the cascade section geometry (by various multichanneling distributions) has an effect on switch resistance and inductance and that these values scale linearly. Using this assumption, when curve-fitting techniques were used for analysis, the resistance of the switch was held constant. Although the resistance value was probably changing, it did not affect the overall load impedance as significantly as the inductance. Analysis of the intermediate

store voltage was used to determine switch inductance. A time-varying inductance model was incorporated into the switch model. The inductance was kept constant until 250 ns after switch breakdown, which, as described above, is the time of interest because it is during the rising edge of load voltage. An example fit is shown in Figure 57. This initial inductance was considered to be the inductance of the switch

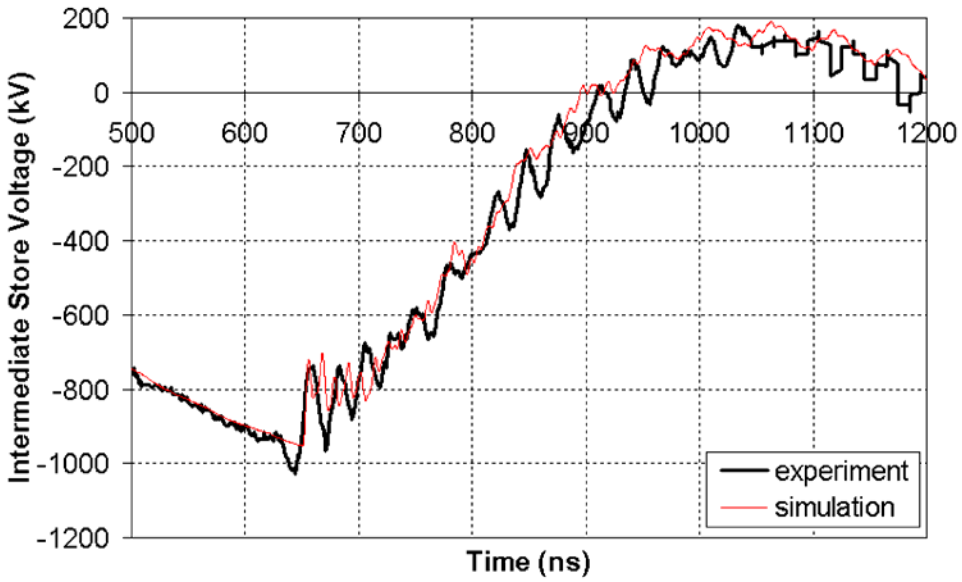

Figure 57: Fit of simulation to experiment for intermediate store voltage for MUTTS shot 130.

For a given test shot, to evaluate the quality of fit of simulation to data, the two curves were analyzed using a computer program. The curves were compared from switch breakdown until the second zero crossing of the intermediate store voltage (around 600 ns after breakdown). As will be discussed later, a shorter period of comparison would have been optimal. At discrete 1 ns time steps (the sampling rate of the oscilloscope), the difference of the voltages was squared. The squaring removes the sign on the difference. To accumulate the total differences

on the waveform, the square root of the sum of all the differences was taken and divided by the number time steps. Equation (11) summarizes this method. Using this equation, a non-subjective method of analysis was utilized. The lower the number generated by the computer program, the better the fit. For a single experimental shot, many simulations were run with several inductances. The switch inductance in the simulation with the best fit was then considered the inductance of the switch. Appendix D has the Matlab program used for these calculations.

$$\frac{\sqrt{\sum_{n=1}^{\#timesteps}[V_{simulation}(t_n) - V_{experiment}(t_n)]^2}}{\#timesteps} = q.o.f. \qquad (11)$$

Using several preliminary simulations for a number of shots, a general range was found for the initial switch inductance. In addition, a best-fit switch resistance, .8 Ω, was found. For all shots, the initial switch inductance was varied from 310 nH to 510 nH in 40 nH intervals. Using the results of the circuit simulations, the quality of fit for each shot for each value of inductance was found. Second order polynomial trend lines were fit to the data points. Shown by Figure 58, as the switch inductance was varied, the quality of fit values formed minima. The value of inductance at these minima was considered to be the switch inductance.

The best-fit inductance was found for each of seven shots of the one arc, two ball, three ball, and six ball 40 kV setups. In Figure 59, the switch inductance for the two, three, and six ball shots is shown versus intermediate store voltage at

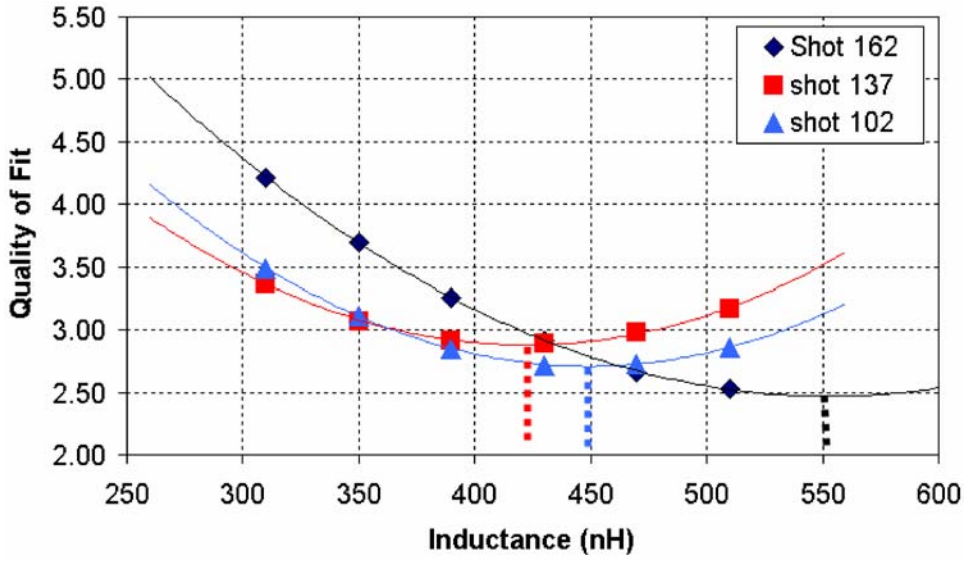

Figure 58: Quality of fit for three sample shots. Trend lines illustrate the parabolic nature of the fits. Shot 162 is a one arc shot, shot 102 is a 2 ball shot, and shot 137 is a 6 ball shot.

the time of switch breakdown. Switch inductance was not found to have statistically significant dependence (p-value >> α) on breakdown voltage. Compared to the method of analyzing load current risetime as illustrated in Figure 54, this method of finding the switch inductance does not depend on breakdown voltage. Therefore, the widely varying breakdown voltage associated with a non-triggered switch is no longer a barrier to determining switch inductance.

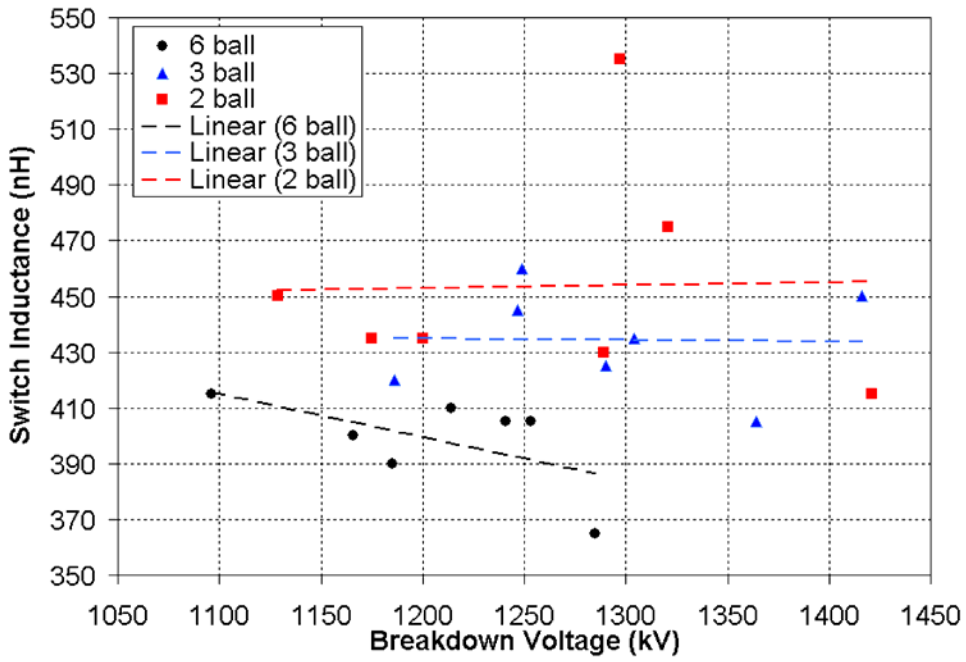

Figure 59: Switch inductance versus switch breakdown voltage. None of the data sets had a statistically significant dependence on breakdown voltage.

4.5.3 Effect of Multichanneling on Electrical Properties

Ignoring placement and continuity of arcs in the cascade section, the number of arcs was counted. Figure 60 shows the switch inductance with respect to total number of arcs in the cascade section. The switch inductance had a statistically significant dependence on the number of arcs.

A second observation regarding switch inductance with respect to multichanneling was made with regard to the number of cascade gaps that had only one arc. If there was a single arc between two MID electrodes at some place in the cascade section, all of the current flowed through that one arc. The number of single arc gaps was counted for a given shot, and is shown with respect to switch inductance in Figure 61. Inductance was found to have a statistically

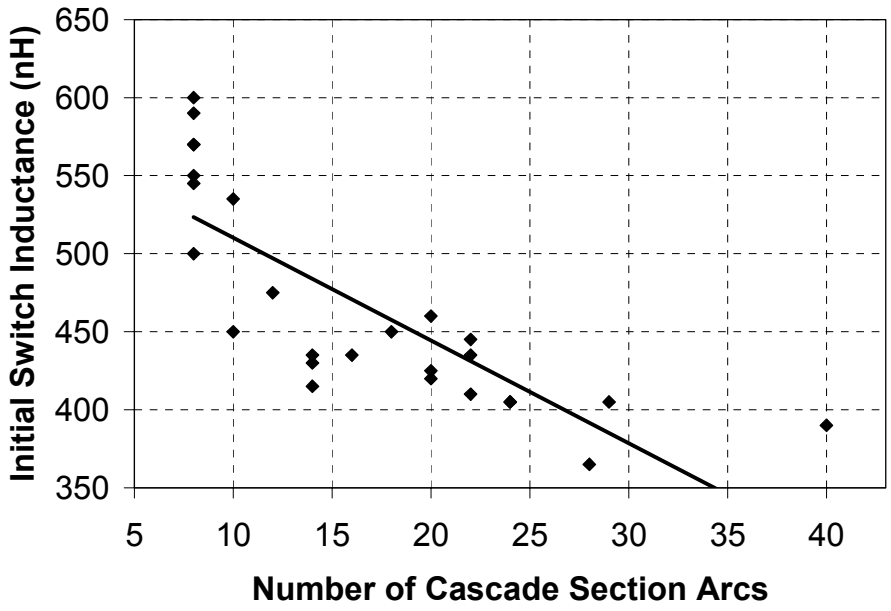

Figure 60: Switch inductance versus total number of cascade section arcs. R^2=.64.

significant dependence on this parameter, and there was a very low, R^2=.82, variance in the data. Compared to Figure 60, this data had a greater influence on switch inductance (82%) than the total number of arcs (64%). However, these variables were not independent, and possibly demonstrate the same phenomenon.

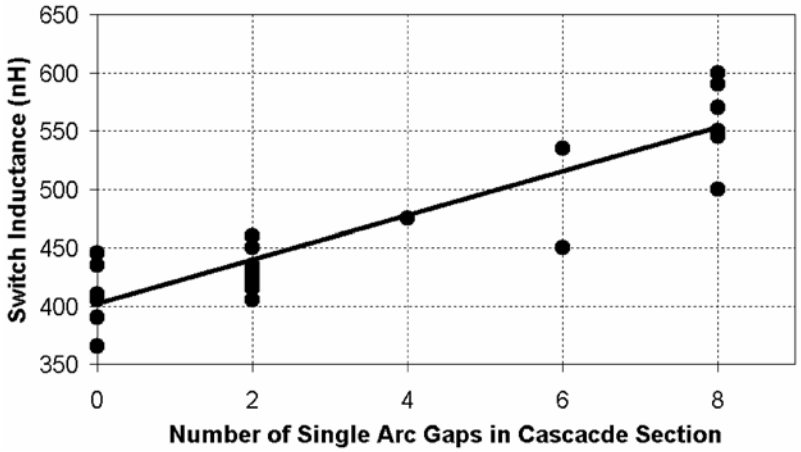

Figure 61: Switch inductance versus number of single arc gaps in the cascade section. R^2=.82.

4.6 Analysis

The results from the previous section present a summary for the tests conducted at MUTTS. However, experimental results also provided insight into the performance of the Rimfire switch in general and showed some guidelines for switch design in the future. This section presents these topics.

4.6.1 Forcing of Multichanneling

There are three possible reasons that adding toroidal electrodes encourages multichannels in the alternating electrode experiments and that the ECMID electrodes multichannel. The first explanation is that multiple arcs did in fact form, but one arc carried the majority of current. If this were true, there should be some optical evidence of a secondary arc. In none of the photographs does a single-channel breakdown show this lighter, secondary arc. However, it is a possibility that the arcs were not luminous enough to be detected.

The second possibility is that electrode-to-electrode capacitance needs to be large enough to force a low dv/dt across the gap. For example, if a single arc forms between a gap, if the capacitance is small, the voltage across the gap may close rapidly. However, if the capacitance is large, additional arcs may form at another location in the gap. The EIHCMID electrode experiments tested this criterion. There did not appear to be any difference between the higher capacitance ball electrodes and the normal electrodes. However, it is possible that a larger capacitance (such as in the toroidal electrodes) is required.

A third explanation for multichanneling is that the arcs in a gap require an inductive connection. Past studies have explored this issue [7]. However, this characteristic was not tested in the MUTTS experiments.

4.6.2 Finite Effect on Inductance

With the size constraints of the MUTTS switch, an ideal switch inductance is calculated. Using a coaxial geometry with the dimensions shown in Table 24 and inductance calculations using equation (5) from section 3.1.2, the ideal switch inductance is found to be 197 nH. This assumes that the switch is entirely composed of toroidal electrodes (similar to the switch in Figure 29). Using these switch dimensions, all improvements to the MUTTS switch only approach this ideal condition.

Table 24: Ideal full-cascade switch inductance given present MUTTS space constraints.

Switch Length	44.5 cm
Current Return Diameter	101 cm
Inner Conductor Diameter	11.4 cm
Ideal Switch Inductance	197 nH

Figure 62 shows the calculated cascade section inductance using equation (5). The figure shows that, after a point, increasing the number of arcs in the cascade section has a diminishing return with respect to inductance. Improvements in multichanneling of the cascade section have a limited benefit after a certain point.

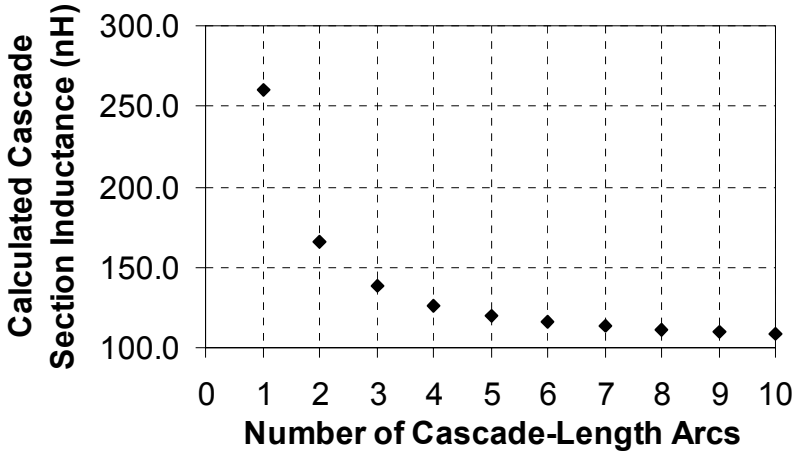

Figure 62: Calculated cascade section inductance for a given number of cascade section-length arcs.

In the MUTTS version of the Rimfire switch, there are two major deviations from the ideal geometry. The first is the trigger section. Current flows in a smaller diameter "inner conductor" for the coaxial geometry in the trigger

section than in the cascade section. The second deviation from the ideal inductance involves the end plates of the switch. Because of skin depth, current cannot penetrate through the metal, but flows along the surface. In addition, the current feeds to the switch are on the outside perimeter. Figure 63 shows the ideal current path in blue, and the present current path in red. In addition, there may be stray inductances that lead to an increased switch inductance.

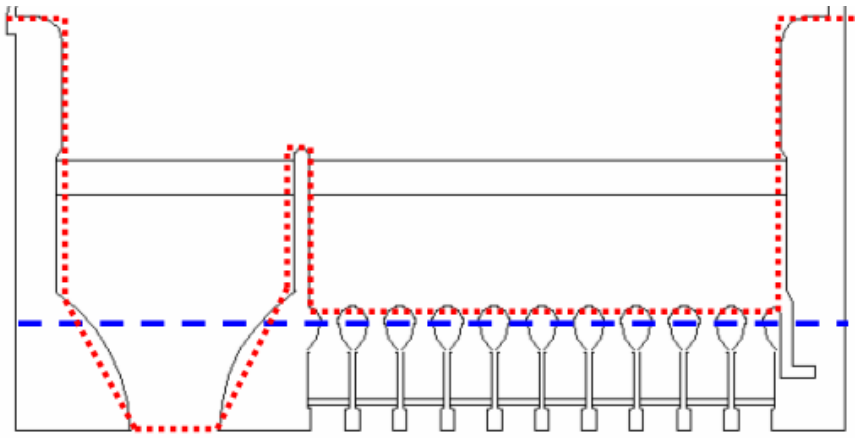

Figure 63: Current paths in the MUTTS Rimfire switch. Ideal path: blue. Present path: red.

Figure 64 shows the results of the 40 kV Marx charge experimental tests grouped according to test setup. As stated above, the ideal inductance for the MUTTS switch was calculated to be ~200 nH. The lowest switch inductance measured was ~390 nH. This added inductance is attributed to the non-ideal geometry of the MUTTS switch described above. Also, there is a relatively large range of data spread for a single shot setup. This is due predominantly to two factors. First, the shot setup does not take into account the quality of multichanneling in the cascade section. If a six ball shot had one cascade section-

length arc, it would still be characterized as a six ball shot. Second, the curve fit was done over a large range of the experimental waveform. If the comparison was focused only on the first 250 ns of the pulse, less variation is expected. In addition, increases in the number of shots will reduce the confidence interval.

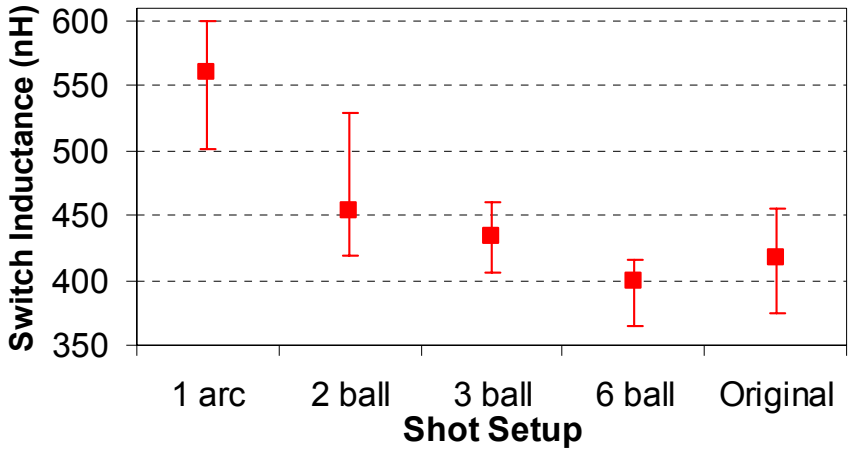

Figure 64: Measured inductance for each shot setup. Data points are means of seven shots. For the original electrodes, only four shots are used. Error bars are the range of data.

To evaluate the effect of the cascade section on the overall switch inductance, the measured switch inductance was compared to the calculated inductance for the cascade section. The only variable in the tests was the geometry of the cascade section, so any switch inductance outside the cascade section was constant from shot to shot. The switch inductance values shown in Figure 64 are compared to the cascade inductance values given by equation (5) shown in Figure 62. Measured and calculated inductances were normalized to the measured switch inductance for the six ball shots. Figure 65 shows that the

calculated inductance is within the range of the measured inductance and the values scale linearly.

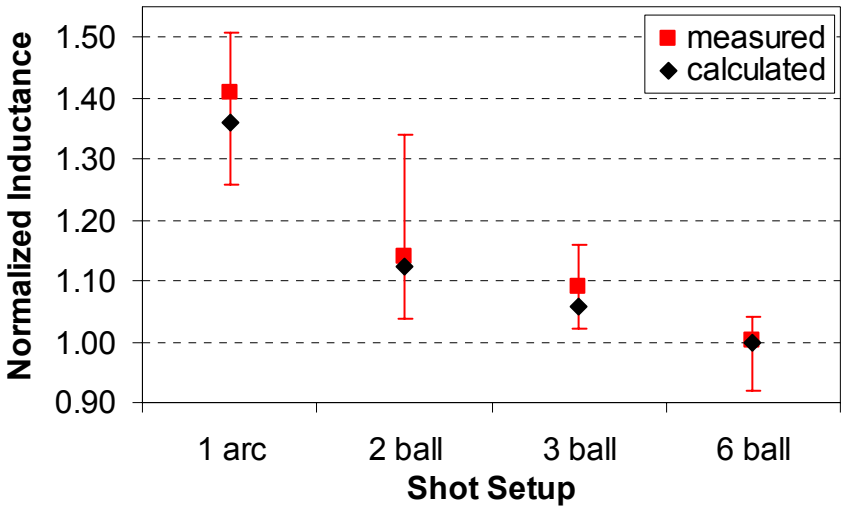

Figure 65: Comparison of measured to calculated switch inductance. Error bars are the range of data and data points are means with N=7.

This strong agreement between measured and calculated inductances also has implications on evaluating the effect of azimuthal current in the cascade electrodes. All the one arc shots must have zero azimuthal current in the electrodes because the ball electrodes were isolated electrically. The two, three, and six ball shots potentially have large azimuthal currents in the toroidal electrodes. If azimuthal currents have relatively large contributions overall to switch inductance, it would be only evident in the two, three and six ball shots. This would mean the two, three, and six ball switch inductances would be closer to the one arc inductance and that calculated inductances would be a large underestimation. This is not shown in Figure 65. Therefore, these tests suggest

that the azimuthal inductance in the cascade section does not have a large effect on overall switch inductance.

4.6.3 Scaling of the Rimfire Switch to Larger Diameters

One possibility for a reduced inductance switch is to have a large diameter cascade section [8]. In a coaxial geometry, a larger inner conductor leads to lower inductance. However, even if the cascade inductances were reduced to zero, the lowest value inductance switch would be 300 nH because of the trigger section, end plates, and stray inductances. One possible solution to the high inductance of the end plates is to feed current at the same diameter as the cascade section. In addition, if several holes are drilled through the metal end plates around the perimeter of the trigger section, current could flow through the end plate and the skin effect issue is minimized. The holes could be plugged with a dielectric to allow pressurization of the switch.

A solution to the high inductance of the trigger section is to construct an all cascade section switch as described in section 3.3.4. This would allow the entire switch to multichannel consistently and allow changes in switch diameter to not be limited by the trigger section. Keeping the length of the switch and the outer diameter constant, Table 25 shows three possible MUTTS Rimfire switches.

Table 25: Effects of variation of cascade electrode diameter on inductance

	Ideal Inductance
Full Cascade Original MUTTS	179 nH
20 cm diameter	134 nH
40 cm diameter	78.1 nH

CHAPTER 4 REFERENCES

[1] D.L.Johnson, "Initial Proto II Pulsed Power Tests," *in Proceedings of the 1st IEEE International Pulsed Power Conference*, Lubbock, TX, 1976.

[2] K.R.LeChien, J.M.Gahl, M.A.Kemp, A.L.Benwell, J.M.Elizondo, and K.W.Struve, "Initial Results from the University of Missouri Terawatt Test Stand," *in Proceedings of the 26th IEEE Power Modulator Symposium*, San Francisco, CA, 2004.

[3] K.R.LeChien and J.M.Gahl, "Investigation of a Multichanneling, Multigap Marx Bank Switch," Review of Scientific Instruments, vol. 75, no. 1, pp. 174-178, Jan.2004.

[4] S.N.Volkov, A.A.Kim, B.M.Kovalchuk, V.V.Kremnev, and V.A.Sinebryukhov, "MV Multi Channel Closing Switch for Water Storages," *in Proceedings of the 12th IEEE International Pulsed Power Conference*, Monterey, CA, 1999.

[5] R.V.Hogg and J.Ledolter, Engineering Statistics, Macmillan Publishing Company, 1987.

[6] T.H.Martin, J.F.Seamen, and D.O.Jobe, "Energy Losses in Switches," *in Proceedings of the 9th IEEE Pulsed Power Conference*, Albuquerque, NM, 1993.

[7] S.Futuya, Y.Watanabe, T.Yoshikawa, S.Takano, and J.Irisawa, "Characteristics of Multichannel Arc Gap," Japanese Journal of Applied Physics, vol. 40, no. 2B, pp. 987-991, 2001.

[8] J.M.Elizondo, K.W.Struve, and H.Ives, "Large Diameter, Low Inductance Gas Switch as a Water Switch Alternative," ZR Technical Note, Num. 9, 2002.

CHAPTER 5

CONCLUSIONS

5.1 Summary and Conclusions

In this thesis, two separate studies were presented: a circuit model of the Rimfire switch and experimental studies of the cascade section. Because most of the focus for each part was on different subjects, a large range of switch functions was studied. Through this two-pronged approach, an overall picture of the operation of the switch was studied.

There have been many designs and versions of the Rimfire switch. Future Rimfire switches will have increased demands and will be of different geometries than presently used switches. Because of these issues, it becomes difficult to suggest specific design parameters that are applicable to all designs. However, given specific requirements for switch operation, design parameters can be suggested. In addition, trends have been presented in this thesis and therefore conclusions are made:

- The Rimfire switch with toroidal electrodes performs better submerged in oil rather than water.

Sections 3.2.1 and 3.3.1 investigated the effects of the Rimfire switch submerged in oil compared to water. When the switch was submerged in water, the runtime was twice as large. This was evident for all trigger percentages of self-break. These results confirm past works in this area [1]. It is not clear if different electrode geometries such as the MID electrodes would perform similarly.

- The value of the added inductance affects the runtime of the hybrid switch.

It was shown in section 3.3.3 that with an increased value of inductance added in series with the trigger section, an increase in runtime resulted. However, smaller magnitude inductances resulted in the parallel cascade electrodes not breaking down and the switch to not function normally. In this case, the inductance of the switch was dominated by the added trigger inductance. In addition, it was found that increased inductance has little effect on reducing currents in the hemispherical trigger section. Past studies do not focus on the actual value of the added inductance [2-4].

- The hybrid switch will have increased jitter compared to the present trigger scheme.

Section 3.3.3 shows that runtime, specifically in the trigger section, is increased in the hybrid switch compared to the normal switch. Switches designed with the hybrid trigger section will probably be limited in their improvement of jitter. Possible decreases in overall switch inductance will have a tradeoff with increases in jitter. Past studies have shown that the hybrid switch has high jitter, but it has not yet been attributed to the added trigger inductance [4].

- Increasing the number of ball electrodes in the MID electrodes, when alternated with toroidal electrodes, increases the total number of cascade arcs.

It was shown that increasing the amount of field enhancement points (ball electrodes) increased the total number of arcs in the cascade section. While this may be intuitive, there was a distinct possibility that increases in ball electrodes would not result in additional arcs forming as was the case when toroidal electrodes were not alternated with the MID electrodes. These results are confirmed by similar work by Volkov *et al.* [2].

- The cascade section multichanneling efficiency is dependent on the breakdown voltage of the switch.

Shown in Figure 53 of section 4.5.1, the multichanneling efficiency (cascade arcs per the number of possible arcs) had a statistically significant dependence on switch breakdown voltage. As the breakdown voltage of the switch increased, there was a tendency to have a larger number of arcs in the

cascade section. However, there was a large spread in data (R^2=.25) and therefore it is not the main contributing factor to multichanneling. Past studies report similar results [5].

- Load current risetime is dependent on the percentage of maximum intermediate store voltage breakdown and, in untriggered switches, cannot be used as an indicator of switch inductance.

Figure 54 in section 4.5.2 shows the strong dependence of load current risetime on the switch breakdown voltage. This is confirmed through circuit simulation. Unless comparing shots with the same breakdown voltage and Marx charge voltages, direct correlation of switch inductance cannot be made with these parameters. A curve fitting technique was developed to circumvent this issue.

- Shots using MID electrodes with more ball electrodes, when alternated with toroidal electrodes, have a lower switch inductance.

It was demonstrated that shots using more ball electrodes in the MID electrodes had a lower switch inductance. In addition, the difference in inductance from switch setup to switch setup is well outside the shot-to-shot standard deviation. This is illustrated in Figure 65 of section 4.6.2. Measured values of inductance using this technique are within the range of error of calculated values.

- Switch inductance is dependent on the total number of cascade section arcs.

Figure 60 in section 4.5.3 shows that switch inductance had a statistically significant dependence on number of cascade section arcs. In addition, Figure 61 shows that the number of single arc discharges in the cascade section has an even larger influence on the switch inductance.

- In the MUTTS Rimfire switch, the cascade section has a large effect on overall switch inductance.

Shots taken without varying any parameters except the cascade section had up to a 46% change in switch inductance. This shows that the cascade section does have a significant role in the overall inductance of the switch. The present MUTTS switch is therefore an appropriate version for evaluating effectiveness of changes to the cascade section.

- Increasing the number of arcs in the cascade section has a diminishing return with regard to lowering cascade section inductance.

After a point, increasing the number of cascade arcs does not have a significant effect on improving cascade section inductance. The discrete arcs only approach the ideal case of a cylinder. This was demonstrated theoretically in

Figure 62 and experimentally in Figure 64. Further improvement of cascade section inductance must involve geometry changes to the electrodes.

- Azimuthal currents in the cascade electrodes appear to have little effect on overall switch inductance.

Shots were taken where no azimuthal currents were possible (the 1 arc case) and where azimuthal currents were allowed (all other shots). If the inductance values are compared, as in Figure 65, the shots with azimuthal currents do not significantly overestimate the calculated values. If the assumption is made that the calculated values overestimate the switch inductance, then the one arc case moves further from the trend, rather than closer to it.

5.2 Future Work

One limitation of the UMC circuit model is that it uses derived inductances. Gathering inductances from field models will improve the accuracy. Also, incorporation of transmission lines instead of discrete capacitors and inductors as circuit elements may prove to have results that better match the electromagnetic code results by Rosenthal [1].

Efforts in future switch design should focus on producing switches that function in a true coaxial geometry. Present designs force currents to flow around large endplates. If current is fed to the switch at the same diameter and then

extracted from the switch at the same diameter, the switch inductance should decrease.

The present trigger section will become a limiting factor when designing lower inductance Rimfire switches. While the hybrid trigger section may provide the inductance desired, circuit simulations suggest it may have unacceptable jitter. Investigations into an all cascade design may prove beneficial. Triggering of the switch will be a major issue to be verified.

Large diameter cascade electrode Rimfire switches need to be developed and tested. Calculations show that they will have a reduced inductance, but the actual switch may or may not be an improvement. In addition, it is unknown what jitter may result from this design.

CHAPTER 5 REFERENCES

[1] S.E.Rosenthal, J.M.Elizondo, J.E.Maenchen, K.W.Struve, D.H.McDaniel, J.P.Corley, D.L.Johnson, and B.V.Oliver, "Modeling 6-MV Gas Switches For the ZR Accelerator," *in Proceedings of the 14th IEEE Pulsed Power Conference*, Dallas, TX, 2003.

[2] S.N.Volkov, A.A.Kim, B.M.Kovalchuk, V.V.Kremnev, and V.A.Sinebryukhov, "MV Multi Channel Closing Switch for Water Storages," *in Proceedings of the 12th IEEE International Pulsed Power Conference*, Monterey, CA, 1999.

[3] J.P.Corley, M.A.Dixon, A.A.Kim, B.M.Kovalchuk, V.A.Sinebryukhov, S.N.Volkov, K.C.Hodge, S.A.Drennan, J.M.Navarro, D.L.Johnson, G.Avrillaud, and F.Lassalle, "Tests of 6-MV Triggered Switches on APPRM at SNL," *in Proceedings of the 13th IEEE International Pulsed Power Conference*, Las Vegas, NV, 2001.

[4] J.P.Corley, K.C.Hodge, S.A.Drennan, D.W.Guthrie, J.M.Navarro, D.L.Johnson, J.M.Lehr, S.E.Rosenthal, and J.M.Elizondo, "Development/Tests of 6-MV Triggered Gas Switches at SNL," *in Proceedings of the 14th IEEE International Pulsed Power Conference*, Dallas, TX, 2003.

[5] K.R.LeChien and J.M.Gahl, "Investigation of a Multichanneling, Multigap Marx Bank Switch," Review of Scientific Instruments, vol. 75, no. 1, pp. 174-178, Jan.2004.

APPENDIX

APPENDIX A

Capacitance Values for all Conductors- Water Dielectric

Below is a table of the capacitance values generated by Maxwell for the ZR baseline switch submerged in water. The capacitance values are in pF. Cas *1-24* represents each of the cascade electrodes, *ground* is the ground return, *disk* is the disk electrode, and *end 1* and *end 2* are the two end electrodes of the switch. These are the capacitance values for Figure 17.

	end 1	cas 1	cas 2	cas 3	cas 4	cas 5	cas 6	cas 7	cas 8
cas 1	24.549								
cas 2	2.915	21.164							
cas 3	2.301	0.355	21.256						
cas 4	1.999	0.111	0.396	21.278					
cas 5	1.797	0.052	0.137	0.412	21.274				
cas 6	1.641	0.031	0.069	0.149	0.422	21.279			
cas 7	1.505	0.020	0.043	0.079	0.156	0.428	21.291		
cas 8	1.386	0.014	0.029	0.050	0.084	0.160	0.431	21.286	
cas 9	1.277	0.011	0.021	0.035	0.054	0.088	0.164	0.433	21.292
cas 10	1.175	0.008	0.016	0.026	0.038	0.057	0.090	0.166	0.435
cas 11	1.081	0.006	0.012	0.020	0.029	0.041	0.060	0.092	0.167
cas 12	0.991	0.005	0.010	0.015	0.022	0.031	0.043	0.061	0.094
cas 13	0.908	0.004	0.008	0.012	0.017	0.024	0.032	0.044	0.063
cas 14	0.828	0.003	0.006	0.010	0.014	0.019	0.025	0.034	0.045
cas 15	0.754	0.003	0.005	0.008	0.011	0.015	0.020	0.026	0.035
cas 16	0.682	0.002	0.004	0.007	0.009	0.012	0.016	0.021	0.027
cas 17	0.615	0.002	0.004	0.005	0.008	0.010	0.013	0.017	0.021
cas 18	0.551	0.002	0.003	0.005	0.006	0.008	0.011	0.014	0.017
cas 19	0.489	0.001	0.002	0.004	0.005	0.007	0.009	0.011	0.014
cas 20	0.428	0.001	0.002	0.003	0.004	0.006	0.007	0.009	0.011
cas 21	0.367	0.001	0.002	0.003	0.004	0.005	0.006	0.007	0.009
cas 22	0.301	0.001	0.001	0.002	0.003	0.004	0.005	0.006	0.007
cas 23	0.224	0.000	0.001	0.001	0.002	0.003	0.003	0.004	0.005
cas 24	0.122	0.000	0.001	0.001	0.001	0.001	0.002	0.002	0.003
disk	1.967	0.004	0.008	0.011	0.016	0.021	0.026	0.032	0.040
end 2	16.907	0.020	0.038	0.057	0.078	0.101	0.126	0.153	0.182
ground	155.510	0.022	0.042	0.062	0.084	0.106	0.130	0.154	0.178

	cas 9	cas 10	cas 11	cas 12	cas 13	cas 14	cas 15	cas 16	cas 17
cas 10	21.296								
cas 11	0.435	21.297							
cas 12	0.168	0.437	21.296						
cas 13	0.095	0.170	0.438	21.293					
cas 14	0.064	0.096	0.171	0.440	21.301				
cas 15	0.046	0.064	0.097	0.172	0.440	21.303			
cas 16	0.035	0.047	0.065	0.097	0.173	0.442	21.299		
cas 17	0.028	0.036	0.047	0.065	0.097	0.173	0.441	21.293	
cas 18	0.022	0.028	0.036	0.047	0.065	0.097	0.172	0.441	21.296
cas 19	0.018	0.022	0.028	0.036	0.047	0.065	0.097	0.171	0.440
cas 20	0.014	0.018	0.022	0.028	0.035	0.047	0.064	0.096	0.169
cas 21	0.011	0.014	0.017	0.022	0.027	0.035	0.045	0.062	0.093
cas 22	0.009	0.011	0.013	0.016	0.020	0.025	0.033	0.043	0.059
cas 23	0.006	0.008	0.009	0.011	0.014	0.017	0.022	0.028	0.037
cas 24	0.003	0.004	0.005	0.006	0.007	0.009	0.011	0.014	0.018
disk	0.048	0.058	0.070	0.084	0.101	0.122	0.148	0.182	0.225
end 2	0.215	0.249	0.287	0.327	0.369	0.414	0.462	0.512	0.564
ground	0.201	0.224	0.245	0.263	0.279	0.292	0.301	0.306	0.306

	cas 18	cas 19	cas 20	cas 21	cas 22	cas 23	cas 24	disk	end 2
cas 19	21.311								
cas 20	0.437	21.310							
cas 21	0.166	0.434	21.299						
cas 22	0.089	0.161	0.428	21.298					
cas 23	0.052	0.080	0.148	0.408	21.253				
cas 24	0.025	0.035	0.057	0.114	0.349	21.128			
disk	0.284	0.366	0.487	0.681	1.037	1.877	24.207		
end 2	0.617	0.668	0.714	0.748	0.745	0.662	0.410	19.257	
ground	0.302	0.293	0.277	0.255	0.223	0.174	0.097	1.789	190.960

APPENDIX B

MUTTS Switch Schematic

Below is a drawing of the MUTTS version of the Rimfire switch. All dimensions are in inches. This switch is a scaled down version of a Proto II switch. Design of this version was done by Keith LeChien at the University of Missouri- Columbia.

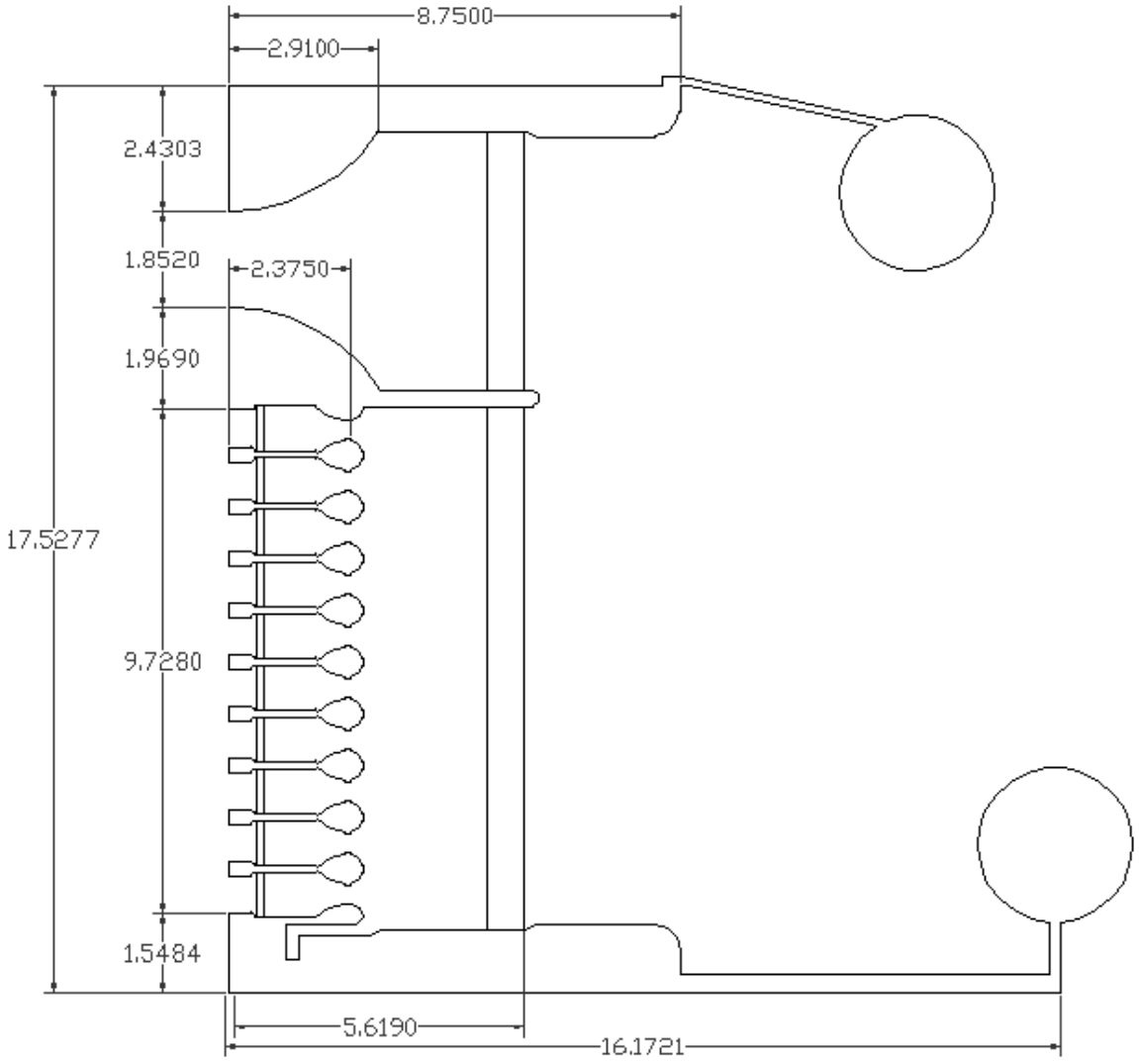

APPENDIX C

ZR Baseline Switch Schematic

This is a schematic of the ZR Baseline switch. All units are in inches. This drawing was provided by Juan Elizondo at Sandia National Laboratories.

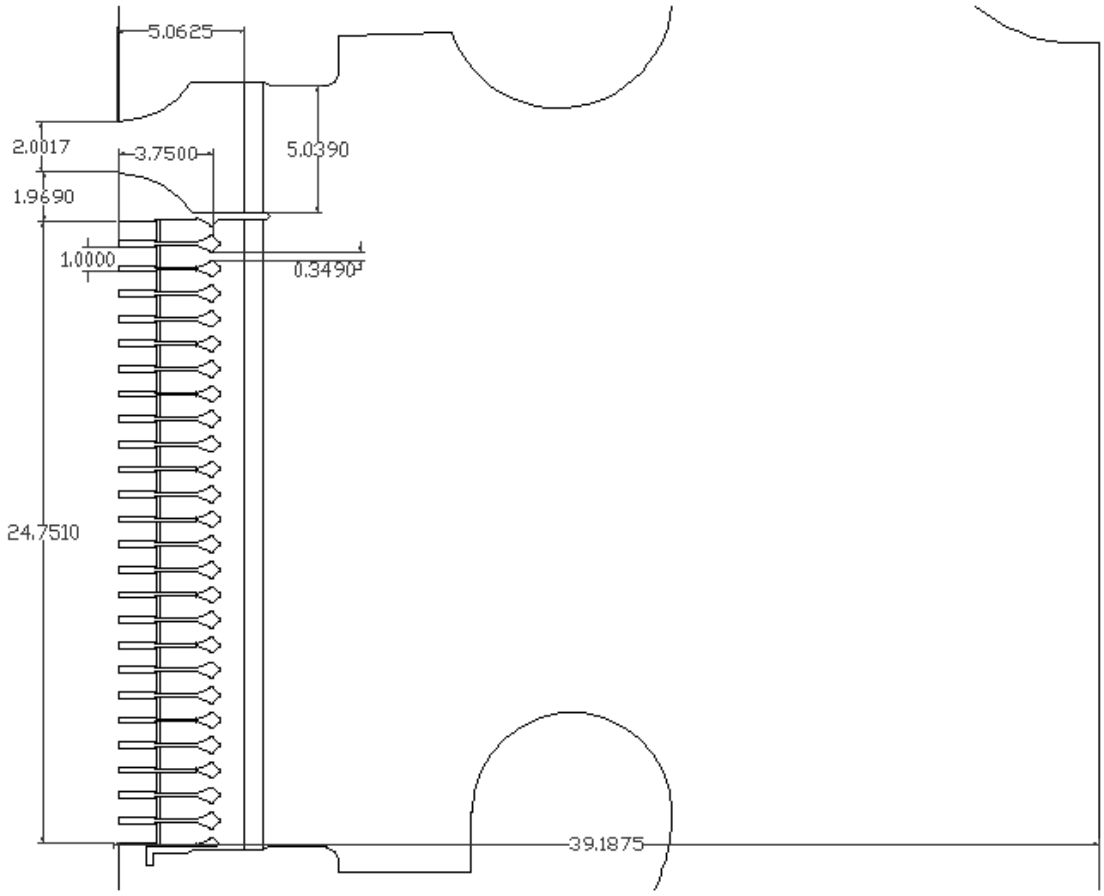

APPENDIX D

"Squares" Curve Correlation program

This is the program used for the curve fitting process in Chapter 4. The code was written for Matlab.

```
%  squares.m
clear;
breakdown_time=702*10^-9;
second_zero_crossing=1235*10^-9;
istore_offset=85*10^-9;
%
shot1='85';
[labels,time_data,trace_data]=readColData(strcat('shot',shot1,'-10.txt'),2,1,1);
trace_data=trace_data*1220*2*17.7/1000;

%y = [time_data'*1e9 ; trace_data'];
%fid = fopen(strcat('C:\Documents and Settings\Administrator\Desktop\MID electrode at
home\csvs\shot',shot1,'istore.txt'),'w');
%fprintf(fid,'%.1f\t%f \n',y);
%fclose(fid);

time_data=time_data+istore_offset;

[labels,time1,y1] = readColData(strcat('shot',shot1,'a.txt'),7,1);
y1=y1/1000;
ya_sum=0;
ya_sum(6)=0;
trace_number=1;
while trace_number<7;
   n=breakdown_time;
   p=1;
   q=1;
   l=0;
   while n<second_zero_crossing
      while time1(p)<n
         p=p+1;
      end;
      while time_data(q)<n
         q=q+1;
      end;
      ya_sum(trace_number)= ya_sum(trace_number)+(y1(p,trace_number)-trace_data(q))^2;
      n=n + 1e-9;
      l=l+1;
   end;
   ya_sum(trace_number)=ya_sum(trace_number)^.5/l;
   trace_number=trace_number+1;
end;

[labels,time1,y1] = readColData(strcat('shot',shot1,'b.txt'),7,1);
y1=y1/1000;
```

```
yb_sum=0;
yb_sum(6)=0;
trace_number=1;
while trace_number<7;
   n=breakdown_time;
   p=1;
   q=1;
   l=0;
   while n<second_zero_crossing
      while time1(p)<n
        p=p+1;
      end;
      while time_data(q)<n
         q=q+1;
      end;
      yb_sum(trace_number)= yb_sum(trace_number)+(y1(p,trace_number)-trace_data(q))^2;
      n=n + 1e-9;
      l=l+1;
   end;
   yb_sum(trace_number)=yb_sum(trace_number)^.5/l;
   trace_number=trace_number+1;
end;

[labels,time1,y1] = readColData(strcat('shot',shot1,'c.txt'),7,1);
y1=y1/1000;
yc_sum=0;
yc_sum(6)=0;
trace_number=1;
while trace_number<7;
   n=breakdown_time;
   p=1;
   q=1;
   l=0;
   while n<second_zero_crossing
      while time1(p)<n
        p=p+1;
      end;
      while time_data(q)<n
         q=q+1;
      end;
      yc_sum(trace_number)= yc_sum(trace_number)+(y1(p,trace_number)-trace_data(q))^2;
      n=n + 1e-9;
      l=l+1;
   end;
   yc_sum(trace_number)=yc_sum(trace_number)^.5/l;
   trace_number=trace_number+1;
end;
format bank
sum(3,6)=0;
sum(1,:)=ya_sum;
sum(2,:)=yb_sum;
sum(3,:)=yc_sum;

sum
```

APPENDIX E

Raw Data from "Squares" Program

Below are the quality of fit numbers that were generated for each shot. The lower the number in the table, the better the fit is. The value of inductance, in nH, is shown in the top right of each shot summary. It is the interpolated value of the initial inductance. The x-axis on the table is the initial inductance value and the y-axis is the final inductance value in nH.

2 ball

Shot101 Inductance 475

	310	**350**	**390**	**430**	**470**	**510**
1375	4.76	4.39	4.12	3.96	3.89	3.91
1600	4.58	4.21	3.94	3.77	3.71	3.74
1825	4.47	4.09	3.82	3.65	3.59	3.63

Shot102 Inductance 450.00

	310	**350**	**390**	**430**	**470**	**510**
1375	3.52	3.16	2.90	2.78	2.79	2.91
1600	3.49	3.11	2.85	2.72	2.73	2.86
1825	3.57	3.19	2.93	2.80	2.80	2.91

Shot103 Inductance 415.00

	310	**350**	**390**	**430**	**470**	**510**
1375	4.83	4.60	4.48	4.45	4.50	4.62
1600	4.67	4.46	4.36	4.34	4.41	4.54
1825	4.55	4.35	4.26	4.25	4.33	4.47

Shot104 Inductance 430.00

	310	**350**	**390**	**430**	**470**	**510**
1375	4.05	3.77	3.61	3.57	3.64	3.80
1600	3.92	3.64	3.49	3.45	3.53	3.69
1825	3.88	3.59	3.44	3.40	3.48	3.65

Shot105 Inductance 435.00

	310	350	390	430	470	510
1375	3.44	4.22	2.93	2.88	2.96	3.15
1600	3.37	3.03	2.84	2.78	2.86	3.06
1825	3.39	3.05	2.86	2.80	2.87	3.06

Shot107 Inductance 535.00

	310	350	390	430	470	510
1375	5.37	4.92	4.56	4.28	4.08	3.97
1600	5.18	4.73	4.36	4.08	3.88	3.78
1825	5.06	4.61	4.24	3.95	3.76	3.65

Shot108 Inductance 435

	310	350	390	430	470	510
1375	3.55	3.23	3.04	2.98	3.05	3.22
1600	3.56	3.23	3.04	2.97	3.04	3.20
1825	3.67	3.35	3.15	3.09	3.14	3.29

3 ball

Shot74 Inductance 460.00

	310	350	390	430	470	510
1375	4.17	3.83	3.59	3.48	3.48	3.57
1600	4.11	3.75	3.51	3.38	3.37	3.46
1825	4.15	3.79	3.53	3.40	3.37	3.45

Shot75 Inductance 445.00

	310	350	390	430	470	510
1375	4.08	3.76	6.56	3.47	3.49	3.61
1600	4.04	3.71	3.50	3.40	3.41	3.53
1825	4.09	3.76	3.53	3.43	3.43	3.53

Shot81 Inductance 450.00

	310	350	390	430	470	510
1375	6.14	5.95	5.84	5.78	5.78	5.82
1600	6.02	5.85	5.74	5.70	5.71	5.77
1825	5.93	5.77	5.67	5.63	5.65	5.71

Shot82 Inductance 420.00

	310	350	390	430	470	510
1375	3.66	3.39	3.27	3.27	3.38	3.58
1600	3.65	3.37	3.23	3.22	3.31	3.50
1825	3.74	3.46	3.31	3.28	3.36	3.54

Shot83 Inductance 435.00

	310	350	390	430	470	510
1375	4.63	4.37	4.22	4.17	4.21	4.34
1600	4.51	4.24	4.08	4.03	4.08	4.20
1825	4.46	4.18	4.02	3.96	3.99	4.11

Shot85 Inductance 405.00

	310	350	390	430	470	510
1375	4.91	4.74	4.67	4.70	4.81	4.98
1600	4.74	4.57	4.51	4.54	4.65	4.83
1825	4.63	4.46	4.39	4.43	4.53	4.70

Shot90 Inductance 425.00

	310	350	390	430	470	510
1375	4.47	4.23	4.10	4.08	4.16	4.30
1600	4.36	4.11	3.97	3.95	4.02	4.17
1825	4.33	4.35	3.93	3.90	3.96	4.11

6 Ball

Shot135 Inductance 405.00

	310	350	390	430	470	510
1375	3.63	3.43	3.38	3.44	3.60	3.85
1600	3.50	3.28	3.21	3.27	3.43	3.68
1825	3.44	3.21	3.13	3.18	3.33	3.57

Shot136 Inductance 400.00

	310	350	390	430	470	510
1375	3.36	3.12	3.03	3.07	3.24	3.49
1600	3.34	3.09	2.99	3.03	3.18	3.42
1825	3.44	3.18	3.07	3.09	3.23	3.45

Shot137 Inductance 415.00

	310	350	390	430	470	510
1375	3.32	3.04	2.90	2.89	3.00	3.22
1600	3.37	3.07	2.91	2.89	2.98	3.17
1825	3.53	3.23	3.06	3.02	3.10	3.26

Shot 139 Inductance 410.00

	310	350	390	430	470	510
1375	3.66	3.44	3.35	3.39	3.53	3.76
1600	3.55	3.32	3.22	3.25	3.39	3.61
1825	3.54	3.30	3.19	3.21	3.34	3.55

shot 141 Inductance 390.00

	310	350	390	430	470	510
1375	3.45	3.28	3.25	3.34	3.54	3.81
1600	3.40	3.21	3.16	3.24	3.42	3.68
1825	3.46	3.26	3.19	3.26	3.42	3.67

Shot142 Inductance 365.00

	310	350	390	430	470	510
1375	4.29	4.20	4.23	4.35	4.55	4.80
1600	4.18	4.08	4.10	4.22	4.42	4.68
1825	4.12	4.02	4.03	4.14	4.34	4.59

Shot143 Inductance 405.00

	310	350	390	430	470	510
1375	3.85	3.66	3.59	3.64	3.79	4.02
1600	3.70	3.49	3.41	3.46	3.60	3.83
1825	3.63	3.41	3.32	3.35	3.48	3.70

Original

Shot34 Inductance 435.00

	310	350	390	430	470	510
1375	3.97	3.69	3.54	3.50	3.57	3.73
1600	3.81	3.52	3.35	3.31	3.37	3.53
1825	3.73	3.42	3.25	3.19	3.25	3.41

Shot35 Inductance 405.00

	310	350	390	430	470	510
1375	3.67	3.47	3.40	3.45	3.61	3.84
1600	3.54	3.32	3.24	3.29	3.44	3.67
1825	3.49	3.26	3.16	3.20	3.35	3.57

Shot36 Inductance 455.00

	310	350	390	430	470	510
1375	4.26	3.95	4.23	3.64	3.65	3.75
1600	4.10	3.77	4.23	3.44	3.44	3.53
1825	4.02	3.67	3.44	3.32	3.31	3.40

Shot37 Inductance 375.00

	310	350	390	430	470	510
1375	3.73	3.61	3.62	3.74	3.95	4.22
1600	3.59	3.46	3.46	3.57	3.77	4.05
1825	3.54	3.39	3.37	3.47	3.67	3.93

1 arc

Shot61 Inductance 500.00

time 1 inductance

	310	350	390	430	470	510
1375	4.96	4.55	4.23	4.02	3.9	3.88
1600	4.79	4.37	4.05	3.82	3.71	3.69
1825	4.77	4.34	4.02	3.79	3.67	3.65

Shot62 Inductance 545.00

	310	350	390	430	470	510
1375	4.84	4.37	3.98	3.66	3.44	3.32
1600	4.83	4.35	3.96	3.64	3.42	3.30
1825	4.91	4.44	4.05	3.74	3.53	3.41

Shot162 Inductance 550

	310	350	390	430	470	510
1375	4.26	3.76	3.34	3.00	2.76	2.64
1600	4.21	3.70	3.26	2.91	2.66	2.53
1825	4.27	3.76	3.32	2.97	2.72	2.58

Shot163 Inductance 570

	310	350	390	430	470	510
1375	3.82	3.31	2.86	2.49	2.21	2.05
1600	4.00	3.50	3.06	2.69	2.41	2.23
1825	4.30	3.82	2.40	3.06	2.80	2.63

Shot164 Inductance 590

	310	350	390	430	470	510
1375	4.42	3.90	3.43	3.02	2.70	2.46
1600	4.57	4.05	3.59	3.19	2.86	2.61
1825	4.83	4.33	3.89	3.51	3.20	2.97

Shot165 Inductance 600

	310	350	390	430	470	510
1375	4.08	3.56	3.09	2.68	2.34	2.08
1600	4.31	3.81	3.35	2.95	2.62	2.38
1825	4.65	4.17	3.74	3.37	3.07	2.85

Shot166 Inductance 570

	310	350	390	430	470	510
1375	3.85	3.36	2.93	2.58	2.31	2.16
1600	4.16	3.69	3.28	2.95	2.70	2.55
1825	4.56	4.13	3.75	3.45	3.22	3.08

Shot167 Inductance 470

	310	350	390	430	470	510
1375	3.52	3.09	2.77	2.58	2.53	2.61
1600	3.54	3.09	2.76	2.56	2.50	2.57
1825	3.67	3.23	2.90	2.70	2.63	2.68